OPTIMIZATION OF A NON-CONTACT SINGLE PHASE DRIVE ULTRASONIC MICROMOTOR: VIA DESIGN AND ANALYSIS OF ENGINEERED STATOR CURVATURE AND SURFACE ACOUSTIC STREAMING ACTUATORS

A Dissertation

Presented to the Faculty of the Graduate School

of Cornell University

In Partial Fulfillment of the Requirements for the Degree of

Doctor of Philosophy

by

Sarvani Piratla

January 2014

OPTIMIZATION OF A NON-CONTACT SINGLE PHASE DRIVE ULTRASONIC MICROMOTOR: VIA DESIGN AND ANALYSIS OF ENGINEERED STATOR CURVATURE AND SURFACE ACOUSTIC STREAMING ACTUATORS CALIBRATION

SARVANI PIRATLA, Ph. D.

Cornell University 2014

We present new design methodologies of the Whispering Gallery Mode Micro Ultrasonic Motor (WGMMUM) that enable control of motor rotation direction, and enable controlled levitation of the rotor. These design degrees of freedom provide insights into future optimization of the motor for high torque density output, allowing for long-term air-operation, low voltage and power consumption, leading to CMOS-electronics compatible ultrasonic micromotors. The MUMPS/PZT motor operates with a drive voltage of 4 – 10 Vpp in the frequency range of 100 kHz - 5 MHz, creating rotation through frictional coupling and acoustic streaming in the rotor-stator gap. Using interferometer measurements, we demonstrate smooth rotation of micromotor at 100 – 500 rpm. We implemented multiple gear coupled surface micromachined ultrasonic motors to achieve direction control, providing frequency selective motor operation.

The ultrasonic motor utilizes radial and circumferential periodic variation of stator curvature that periodically modulates the gap between the rotor and the stator. We demonstrated designs of the stator with periodic patterns of gold layer as a method to induced theta periodic gaps between the stator and the rotor. The analytical analysis of the multilayer structure matched well with the measured curvature information. The

motor is designed to be tested under optical interferometer at different operating temperatures. Temperature dependence of the curvature demonstrates that temperature can be used to control the efficiency and coupling of the ultrasonic motor.

A thermal actuator driven gripper actuator is used as a braking mechanism, but experimentally seen to control not only the speed but also the direction of the rotor motion by modulating the rotor gripper gap in nanometer dimensions. Analysis and experiments show the operating mechanism as acoustic streaming forces in the air gap between the gripper and the rotor, providing an active MEMS approach to generate acoustic streaming actuators. Upon preliminary demonstrations of levitation of the motor, non-contact control of angular speed, and non-contact optical means of measurement, towards the use of ultrasonic micromotor as a rotation platform for inertial sensor calibration, we fabricated a gyroscope and showed a method of attaching a separate chip to a released motor using a focused ion beam nano-welding process.

BIOGRAPHICAL SKETCH

Sarvani was born in Guntur, Andhra Pradesh, India. She graduated with a Bachelor's degree in Mechanical Engineering from the Indian Institute of Technology Madras, India in 2007. She then completed her Master's degree in Mechanical Engineering from The Ohio State University, Columbus, USA in 2009. In the same year, she began pursuing her Ph.D. degree in Cornell University. She has been with SonicMEMS lab pursuing Ph.D. in Electrical Engineering under the guidance of Dr. Amit Lal since spring of 2010.

To my parents Venkata Ramana Piratla and Narayana Murty Piratla, teachers, friends, husband Siva Pulla, brothers Pavan Ram Piratla, Kalyan Ram Piratla, and all girls from towns and villages of Andhra Pradesh.

ACKNOWLEDGMENTS

The years I spent at Cornell have given me some of the best learning experiences of my life. I would like to acknowledge the outstanding people who made this journey possible. I am grateful to Prof. Amit Lal for the opportunity to conduct research in the field of Ultrasonic Micromotors. His progressive and dynamic approach of solving technologically challenging problems, pragmatic manner of guiding and providing unending support to students has deeply influenced my years in the Ph.D program. I would like to thank Committee members Professor Alan Zehnder, Professor Sunil Bhave, Professor Alyosha Molnar for providing feedback on my work and encouraging me. I would like to thank Dr. Sasikanth Manipatruni who encouraged me to join SonicMEMS lab. I am also truly thankful to my lab mates Serhan, Kwame, Steven, Larry, Hadi, Po-cheng, Jason, Justin, Janet, Sachin, Yue, JuneHo, Ved for helping me in my research and providing continuous support. I would like to acknowledge the support of DARPA μPNT program in funding my research. I am thankful to all Electrical engineering staff especially, Sue Bulkley, Scott Coldren, Daniel Ritcher, Patricia Gonyea. I would also like to thank Cornell Nanofabrication facility staff and Cornell Center for Material Research staff for assisting me in fabrication process. Finally I would like to thank my parents, two brothers, my husband Siva, my in-laws for their moral support and encouragement.

TABLE OF CONTENTS

BIOGRAPHICAL SKETCH iii

DEDICATION iv

ACKNOWLEDGMENTS v

LIST OF FIGURES viii

LIST OF TABLES xiii

1 INTRODUCTION 1

2 RESONANT STATOR ACTUATION OF GEAR COUPLED ULTRASONIC MOTORS 8

2.1 Introduction 8

2.2 Motor structure and fabrication 9

2.3 Piezo-actuation of MEMS 11

2.3.1 Response of an anchored disk on silicon substrate due to PZT induced vibrations 15

2.3.2 Motor rotation due to acoustic coupling mechanism 20

2.4 Ultrasonic motor characteristics 22

2.4.1 Rotation rate 23

2.4.2 Burst mode operation 25

2.4.3 Effect of frequency splitting rotor motion 25

2.5 Gear coupled motors 29

2.5.1 Mode control 30

2.6 Conclusions 33

3 EFFECT OF STATOR-ROTOR GAP MODULATION ON MOTOR PERFORMANCE 34

3.1 Outline 34

3.2 Design features for optical metrology and rotor gripping 34

3.3 Stator curvature and buckling 36
3.3.1 Curvature and rotation rate variation with temperature 46
3.4 Levitation of ultrasonic motors 49
3.5 Conclusions 52
4 NON-CONTACT ROTOR CONTROL USING THERMAL ACTUATORS 53
4.1 Introduction 53
4.2 Non-contact rotor control through thermal actuator driven gripper 54
4.2.1 Analysis of thermal actuators 56
4.2.2 Rotation rate and direction control 60
4.2.3 Thermal actuator aided actuation of motors 68
4.3 Optical interrogation 68
4.4 Conclusions 70
5 INERTIAL SENSOR CALIBRATION ON ROTOR 72
5.1 Outline 72
5.2 Gyroscope design and fabrication 77
5.3 Beam bonding on motor using focused ion beam nanomachining 84
APPENDIX 88
A. Ultrasonic Motor – Dimensions 88
B. PZT – Motor Assembly 91
C. Thermomechanical FEM model of thermal gripper 92
D. Rotor control through Gripper – Mathematica derivation 94
REFERENCES 95

LIST OF FIGURES

Figure 1.1 Different kinds of motors in use [9] 2

Figure 1.2 (a) Bar type USM used in canon camera for auto-focusing application [12], (b) NASA/JPL Mars micro-lander has dexterous micro-manipulator that uses disk type traveling wave USM [13], (c) Two USMs used in SAMSUNG cellular phone to independently control focusing and optical zooming control [14], (d) Two rotary USMs used in XY positioning stage [15], (e)World's lightest micro-flying robot built by EPSON that has two contra rotating propellers powered by four USMs [16], (f) Traveling wave USM is used in a vibration alarm of a watch [15]. 4

Figure 1.3 PZT/Si laminate with hub and stator. 5

Figure 2.1 PolyMUMPS surface micromachining process showing (a) device before release and (b) after release. It consists of three structural layers Poly0, Poly1, Poly2 and two oxide layers OX1 and OX2. 9

Figure 2.2 Schematic of the ultrasonic micromotor (a) before release, (b) after release 10

Figure 2.3 Schematic and optical image of the ultrasonic motor bonded to the PZTplate. 12

Figure 2.4 Measured impedance of PZT plate with and without Si die 12

Figure 2.5 Velocity amplitude of the substrate, rotor, and stator as a function of frequency measured by Laser Doppler Vibrometer shows the resonant modes of stator at 3 to 4 MHz range, independent of the substrate and rotor resonant modes. 14

Figure 2.6 Frequency spectrum at different excitation frequencies to quantify nonlinear components creating rotation of the motor (a) 2.31 MHz, (b) 2.33 MHz, (c) 2.42 MHz which belongs to quasi-periodic regime. 16

Figure 2.7 (a) Frequency sweep of ultrasonic micromotor with Doppler vibrometer shows one of the peaks at 3.17 MHz at which frequency splitting of 1.53 MHz, 1.64 MHz is observed. 2D scan of the motor showing the mode shapes at (b), (e) 3.17 MHz, (c), (f) 1.53 MHz and (d), (g) 1.64 MHz. 17

Figure 2.8 Schematic shows that from post-buckling vibration analysis of the buckled stator, and the resulting acoustic streaming induced motion. 21

Figure 2.9 Schematic of the ultrasonic micromotor set up with VCSEL and photo detector to measure the rotation rate. 23

Figure 2.10 Rotation rates of various micromotors with voltage. 24

Figure 2.11 Burst mode actuation of the slot stator ultrasonic motor design 25

Figure 2.12 Spectrum analyzer measurements of the motor shown in inset at (a) 4.38 MHz, (b) 4.39 MHz. Motor rotated CCW at 4.38 MHz and CW at 4.39 MHz. During the rotation of the motor, the amplitudes of the subharmonic modes at half the frequency changed from 4.38 MHz to 4.39 MHz. 26

Figure 2.13 Two similar motors (one in this plot and one motor in the Figure 2.12 (b)) from different dies rotate in the same direction (CW) at 4.39 MHz. 28

Figure 2.14 (a) Schematic of the three ultrasonic motor structure, (b) SEM of the structure fabricated in MUMPS process flow with inset showing adjacent motors connected by gear teeth, (c) optical micrograph of the three motors. 29

Figure 2.15 Finite element simulation of mode shape at (a) 390 kHz for the left stator-rotor rotated CCW, (b) 225 kHz for the right stator-rotor rotated CCW, (c) 267 kHz for the right stator-rotor rotated CCW, (d) 215 kHz for the right stator-rotor rotated CW..... 30

Figure 2.16 Top and middle show optical interferometer data on for left and right motor stator. Note the difference response due to different stator size. 31

Figure 2.17 Different combinations of rotation achieved at different frequencies. The data points correspond to the actuation schemes shown in Table 1.2 32

Figure 3.1 (a) Schematic of ultrasonically driven micromotor with integrated grating accelerometer. A thermal actuator is used to move a gripper close to the spinning levitated motor, (b) Cross-sectional view of the motor before release, (c) Cross-sectional view of the motor after release, (d) SEM of the motor on a substrate, inset showing the diffraction grating that can be used as an integrated accelerometer and to measure rotational speed of the motor..... 35

Figure 3.2 Motor stators with different patterns of gold leading different curvatures (a) no gold, (b) completely covered with gold, (c) covered in 4 sectors, (d) covered in 6 sectors. The bottom four images are 3D profiles of corresponding top (with horizontal to vertical dimensions not to scale) recorded using ZYGO optical profilometer, (e) SEM image of stator completely covered with gold, (f) SEM image of stator (c)..... 37

Figure 3.3 (a) A buckled focusing mirror [51][53] (b) optical image of motor shows similar buckled pattern of stator. 38

Figure 3.4 Three characteristic evolutions of buckling patterns of a circular microstructure during etching with HF show that buckling pattern does depend on the plate size. At different times of HF release, buckling of stator pattern is recorded [54]. 38

Figure 3.5 Multi-layered stator comprising of polysilicon, chrome and gold layer. The thicknesses of these three layers are comparable. Gold layer is evaporated at 110oC and when the stator is operated at room temperature, due to the difference in coefficient of thermal expansion of the three layers, there will be in-plane plate force and thermal bending moment on the stator. 39

Figure 3.6 Buckling simulation of stator covered completely with gold agrees to experimentally measure of out of plane deflection. 45

Figure 3.7 Out of plane deflection variation with HF etch time 45

Figure 3.8 The stator has 4 peaks right after release in (a) and after excitation of the stator, due to change in residual stress from bending and with time, the buckling mode shape changed to three peaks 46

Figure 3.9 The hot plate with ultrasonic motor on it is placed on ZYGO optical profilometer stage to measure the topography of the motor from which levitation of the rotor, variation of the stator with temperature can be calculated. The motor is actuated using sinusoidal voltage provided by the function generator..... 47

Figure 3.10 2D top view of the motor at (a) room temperature, (b) 65oC, 3D view of the motor at (c) room temperature showing the curvature bending of the stator, (d) at 65oC shows flat stator. 48

Figure 3.11 Out of plane deflection of the motor shows (a) hill, (b) valley..... 48

Figure 3.12 (a) Stator height decreases with temperature in a quadratic manner, (b) Rotation rate variation with temperature shows that there is an optimum curvature for highest rotation rate. 49

Figure 3.13 Levitation of the rotor is calculated from the difference between the out of plane deformation profile of the motor with and without actuation..... 50

Figure 3.14 Levitation height during rotation (measured with ZYGO) with drive voltage at (a) 3.25 MHz, (b) 2.41 MHz. 51

Figure 3.15 Levitation height measured during rotation of motor with drive voltage at 2.46 MHz 51

Figure 4.1 SEM of the thermal actuator that moves the gripper towards rotor..... 54

Figure 4.2 Rotor-Gripper Gap variation with voltage 55

Figure 4.3 Infrared images of the motor captured at (a) 2V, (b) 6.5 V applied to thermal actuator shows heating of the substrate and the stator along with the thermal actuator driven gripper with increase in voltage. Color code units (a) and (b) are in degree Centigrade. 56

Figure 4.4 (a) cross-section diagram of the actuator for thermal analysis, (b) shows dimension labels of various beams. 57

Figure 4.5 (a) Gripper moves due to substrate motion and creates a gradient in the sonic shear viscous field (uθ) giving rise to acoustic streaming force FAS, (b) Due to small rotor-gripper gap compared to the length of gripper, the rotor and the gripper can be represented in a two dimensional Cartesian coordinate system with vibration of the gripper at PZT drive frequency as the initial non-zero condition..... 63

Figure 4.6 Rotation rate increases as the gripper gap decreases with increasing actuator voltage. As the gripper starts touching the rotor, the rotation rate decreases. 66

Figure 4.7 Rotation rate as a function of thermal actuator voltage shows that shear viscous force can change direction of rotation (CCW- to CW+). Threshold changes with drive voltage, with increased role of shear drive..... 67

Figure 4.8 (a) Fixed and movable gratings , (b) and (c) shows diffraction grating pattern rotates with rotor motion, (d) showing ultrasonic motor, VCSEL, CMOS imager for optical readout of an accelerometer in a package of 10 x 2 x 3 cm. Figure 4: (a) Schematic set up shows a levitated rotor with integrated inertial sensor held by two grippers, and the diffraction pattern from the gratings of the inertial sensor and others is read by a CMOS imager when a VCSEL light is emitted on part of the motor. (b) Schematic of fixed gratings on the substrate G2, movable gratings on the rotor G1, and accelerometer gratings AG. 69

Figure 5.1 Schematic showing the key components measured with MEMS inertial sensors 72

Figure 5.2 Three-axis accelerometer 73

Figure 5.3 Orientation of accelerometers in six different directions (three opposite directions not shown here) to do accelerometer calibration according to six position static test [68]. 74

Figure 5.4 Carouseling method of reducing bias by SANDIA national labs. 76

Figure 5.5 Several applications of gyroscope that are in current use – (a), (b) Gyroscope Stabilized platform, (c) Inertial Measurement Unit, (d) Head mount display, (e) Ball joint, (f) Midcourse navigation, (g) Rotation sensing, (h) Motion compensation, (i) FLIR, (j) Vehicle stability control, (k) Motion sensing game controller..... 78

Figure 5.6 Design of the gyroscope shows masses mA and mB, driven in opposite directions and the Coriolis force in z direction due to rotation of gyroscope in y axis [71]. 79

Figure 5.7 Gyroscope design shown in Figure 5.6 can be sensed through transmittive diffraction or reflective diffraction. 80

Figure 5.8 Process flow for the fabrication of gyroscope using a 2 mask process – 1) SOI wafer with 25 µm of device layer, 2 µm of buried oxide, 375 µm of backside oxide, 2) 100 nm of MoSi2 is sputtered on device layer, 3) 2 µm of GSI oxide deposited on backside, 4) Negative photoresist nLOF 2020 is spun on front side and is patterned, 5) Front side oxide etched using DRIE process after etching of 100 nm of MoSi2 using Oxford 100, 6) Removal of front side photoresist, 7) Positive photoresist SPR 3.0 coated on backside and patterned, 8) Backside oxide etched using Oxford 100, 9) Using oxide as the mask, backside silicon is etched using DRIE process, 10) The device is released in BOE. 82

Figure 5.9 SEM images of fabricated gyroscope, inset showing actuation and sensing comb fingers. 83

Figure 5.10 Gyroscope device bonded to surf board for testing 83

Figure 5.11 Side-view of the inertial sensor bonded to the rotor 84

Figure 5.12 Surface profile height of the motor showing the maximum stator height is at 4.5 µm and the pedestal has to be higher than the stator height. 85

Figure 5.13 (a) Left: Focused Ion Beam tool, inset showing the tungsten probes, Right: tungsten probe tip bonded to the beam with Platinum deposition, (b) Process flow of cutting beam from external structure using ion milling and bonding it onto rotor using Platinum deposition step..... 86

Figure 5.14 External structures bonded onto the micromotor rotor through Focused Ion Beam method, (a) beam of size 75 µm x 15 µm x 3 µm, (b) probe tip separation after bonding beam of size 15 µm x 20 µm x 3 µm, (c), (d) shows view of the motor with two and four beams. 87

Figure A.1 Ultrasonic Micromotor and thermal actuator gripper dimensions 88

Figure A.2 Assembly process of micromotor to PZTusing Brass Zig and vacuum pump. 91

LIST OF TABLES

Table 2.1gives operating and performance parameters of ultrasonic micromotor 22

Table 2.2 explains the concept how central motor can be rotated at either directions by exciting left and right motors at different frequencies. 31

Table 2.3 gives possible combinations of direction of rotation of left, right rotor resulting in central rotor motion. 32

Table 3.1 Elastic Modulus E, Poisson's ratio (ν), thermal expansion coefficient (α) of Poly-Si, Au, Cr. 40

Table 4.1 Parameters used in the analysis 58

Chapter 1

INTRODUCTION

Surface micromachining is a ubiquitous fabrication technique in MEMS, and is used to realize free-to-move, microscale structures, which can be actuated by electrostatic, magnetic, thermal, ultrasonic, etc. forces [1][2]. All of these actuation methods have been used to realize on-chip micromotors, which have been a goal of many researchers since early years of MEMS development [3][4][5][6]. Different kinds of motors that are in use today, at all scales are shown in Figure 1.1. Among these, the predominantly used motors are electric motors, especially AC and DC motors which are again categorized into several varieties based on structure, operation principle and application etc. Numerous applications from daily life use electromagnetic motors as their operating principle is well understood and their designs are optimized for several applications. In a conventional electromagnetic motor, a current carrying coil acts like an electromagnet and this coil in the presence of poles of a magnet or a magnetic field created by other coils, gives rise to rotary torque resulting in rotation. These motors typically need high current and can have excessive ohmic heating of the coil. In applications needing miniaturized rotors or small angular rotations, it is hard to realize the electromagnetic effect through the coils that are often bulky in size, even with IC fabrication techniques. Even if the scale of these motors is reduced, the electromagnetic driving force promotes an undesirable high speed and low torque regime [7].

Unlike the electromagnetic motors, electrostatic motors can have very low power consumption and are most widely researched in the MEMS community as small gaps can be achieved for high electric fields. The patterning and processing of dielectric

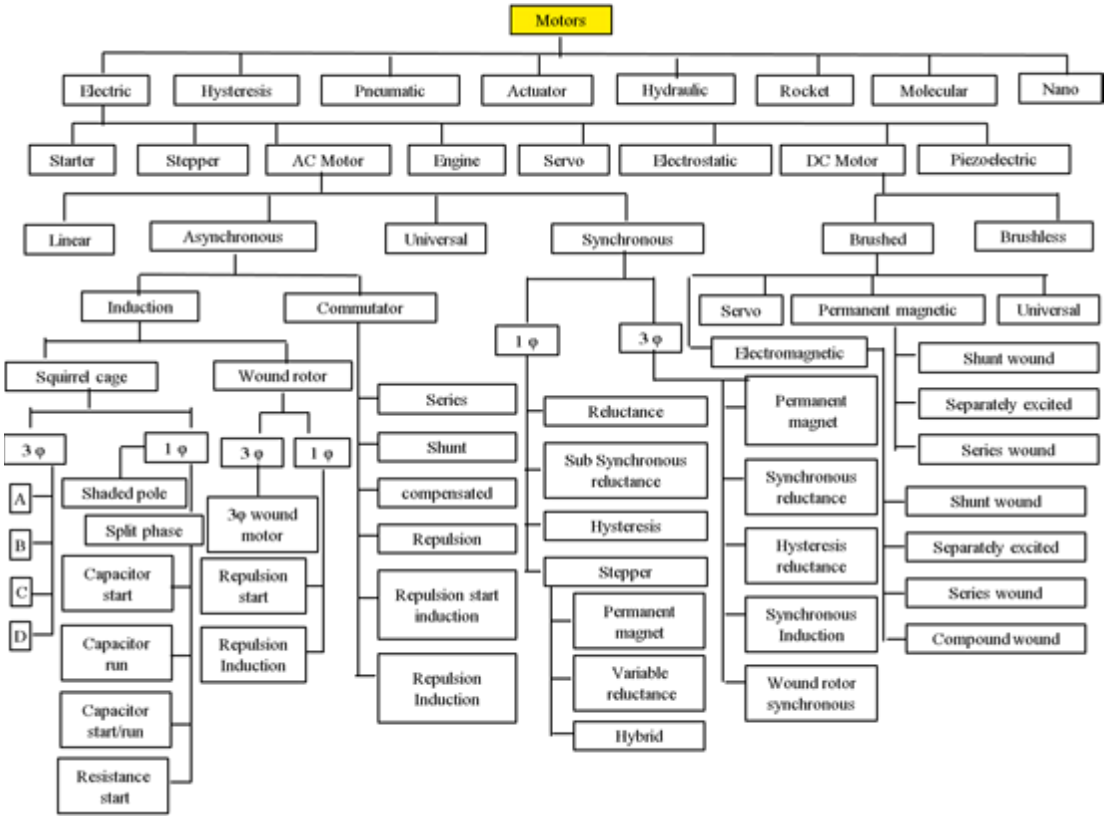

Figure 1.1 Different kinds of motors in use [9]

materials is easier compared to magnetic materials. Electrostatic forces increases as dimensions reduce, making electrostatic micromotors favorable over magnetic micromotors [8]. The MEMS electrostatic motors still need high drive voltage, in-spite of narrow electrode gaps, typically tens to hundreds of volts, and also operate at very high speeds and low torque. Gears are often needed in order to convert to lower speed range. The high voltages needed make drive electronics often incompatible with CMOS-miniaturization. The need for gears to increase torque can make the overall surface area high which is sometimes incompatible with small implementation requirements.

A class of motors called piezoelectric ultrasonic motors, use reverse piezoelectric effect, and converts vibratory motion into linear or rotary motion. Typically PZT (Lead Zirconate Titanate oxide) ceramic piezoelectrics are used to realize ultrasonic motors. The dielectric constant of the PZT is three orders of magnitude higher than air, and thus using PZT can store high amounts of electrical energy, unlike electrostatic actuators where air is used with a dielectric constant of one.

Ultrasonic motors (USM) have high torque, low speed characteristics, and are compatible with silicon integration technologies. They potentially have small size, low acoustical noise, and can operate at low voltages when the PZT is driven at resonance. These motors can maintain holding torque without the need of power due to frictional coupling between the rotor and stator. Miniaturized motors can be used in micro-optical systems [10][11], micro-sensor calibration, and position modulation. The surface micromachined motors can be integrated with optics microsystems such as lab-on-a-chip applications. Figure 1.2 shows some current applications of ultrasonic motors**.**

Commercial ultrasonic motors use direct contact between the rotor and stator and use multi-phase drives to achieve traveling elliptical motion on the stator. Direct solid-solid contact motors at the microscale suffer from charging and abrasion that can lead to ultimate failure limiting motor lifetime. In contrast to an ultrasonic motor with contact, non-contact ultrasonic motors use nonlinear effects such as acoustic radiation force and acoustic streaming for rotor actuation. These forces are proportional to the gradient of the ultrasonic energy fields. This approach is particularly advantageous at the microscale where high gradients of sonic fields are easily achievable around sharp boundary conditions, and both radiation and streaming forces are proportional to sonic

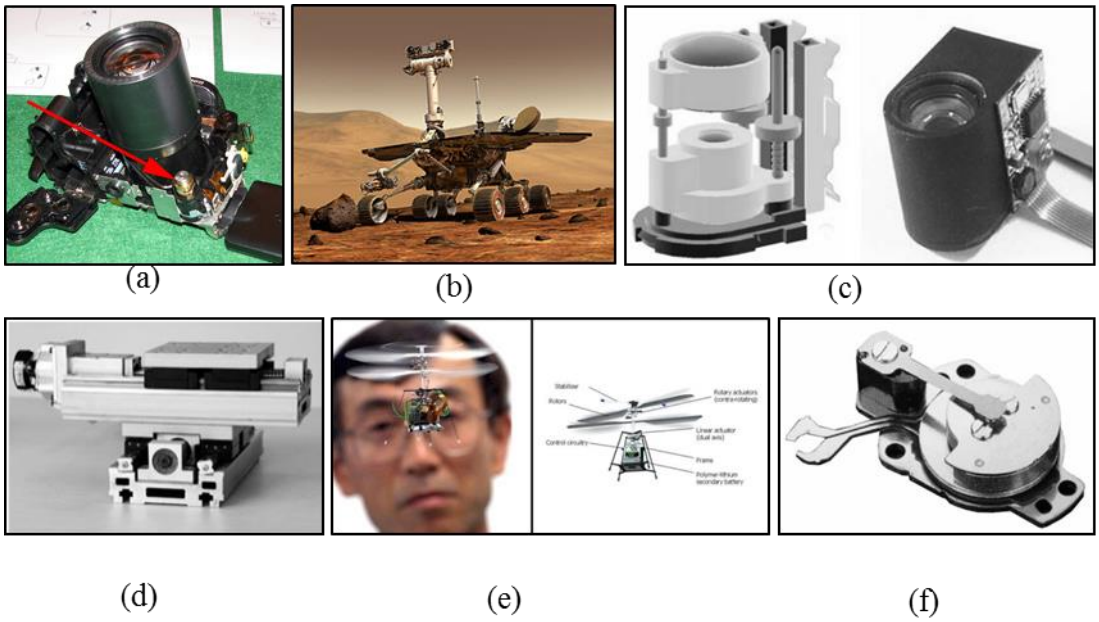

Figure 1.2 (a) Bar type USM used in canon camera for auto-focusing application [12], (b) NASA/JPL Mars micro-lander has dexterous micro-manipulator that uses disk type traveling wave USM [13], (c) Two USMs used in SAMSUNG cellular phone to independently control focusing and optical zooming control [14], (d) Two rotary USMs used in XY positioning stage [15], (e)World's lightest micro-flying robot built by EPSON that has two contra rotating propellers powered by four USMs [16], (f) Traveling wave USM is used in a vibration alarm of a watch [15].

field gradients. Non-contact motors also have the advantage of being naturally cushioned by an air bearing. Non-contact ultrasonic motor designs are studied in detail by various researchers [17][18][19][20][21][22][23][24][25][26][27]. The size of the previous motors is macroscopic in the range of 1-3 cm edge dimensions, and the smallest gap between the stator and rotor found in literature is 50 μm. In our work,

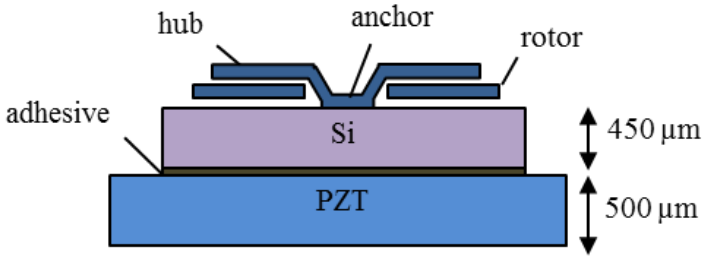

Figure 1.3 PZT/Si laminate with hub and stator.

utilizing lithographic resolution of 1 µm in microfabrication, we have realized surface micromachined ultrasonic micromotors of 1mm diameter, with an average 2 µm gap between the rotor and the stator.

The conventional ultrasonic motors use two ultrasonic standing waves that are 90 degrees out of phase both spatially and temporally, in order to create a traveling wave on the stator. In our motor, we use a single phase drive to realize the ultrasonic motor.

Single phase ultrasonic actuation offers many advantages such as low voltage, low power consumption, and minimum external wiring to run the motor [5][28]. Mesoscale ultrasonic motors have shown trends of shrinking over the last decades: 1 to 3 cm diameter USM by [7][8][17][29][30], 1 µm to 1 cm diameter USM by [4][31][32].

Our group's efforts have led to a surface micromachined implementation of an ultrasonic motor that operates with sub 3 Vpp single phase drive actuation using a bulk-PZT actuated chip [5], also breaking the record for the smallest ultrasonic motor till then. In the MEMS ultrasonic motor, vibrations are transferred from the bulk-PZT and substrate combination to the stator through inertial coupling. These vibrations on the stator are of high amplitude and nonlinear in nature. Any asymmetry or imperfection in the stator in the presence of these high amplitude vibrations can give

rise to the parametric instability followed by multimode excitation resulting in traveling wave that couples with rotor, giving rise to rotation. The dominant factor that causes this asymmetry is found to be the anchor motion induced in-plane stresses [33].

The sub harmonic modes due to nonlinear high amplitude stator vibrations that give rise to traveling wave component were detected by experiments and confirmed through simulations. Upon successful demonstration of motor rotation, angular control of as small as 0.1 degree was achieved from burst mode actuation of PZT plate. The rotation, vibration and actuation properties of the motors with different dimensions of the stator were studied and found that the larger stator corresponds to lower rotational threshold voltage, but smaller stator gives higher rotational speed [34].

These previous works on single phase drive micromotors [5] [33][34][35][36][37][38][39] highlighted the design challenges with controlling the motor operation despite ease of assembly. These challenges are significant as the actuation mechanism is nonlinear and is a function of boundary conditions, presenting specific states of operation that are harder to control. Hence, an understanding and control of these motors is important to fully utilize their potential in microsystems.

In this thesis, we present several structural aspects that enable better motor control. In Chapter 2, we present the results of testing the previous ultrasonic motor design by driving it at different frequencies to get different directions. We also present actuation and direction control of multiple gear-coupled surface micromachined ultrasonic motors. The multiple motor driver of a central rotor enables direction control once the directions of the two motors at different frequencies have been characterized. In Chapter 3, we investigate the effect of modulating the stator-rotor gap by built in stress

on the stator. We demonstrate controlled levitation and measure temperature dependence of curvature and rotation rate. In Chapter 4, we use a thermal actuator to grip the rotor and demonstrate the utility of acoustic streaming force between the gripper and rotor as yet another mechanism to drive the ultrasonic motor and control the angular speed of the motor. In Chapter 5, we demonstrate the possibility of inertial sensor calibration by showing how a separate chip can be attached to a released ultrasonic motor.

Chapter 2

RESONANT STATOR ACTUATION OF GEAR COUPLED ULTRASONIC MOTORS

2.1 Introduction

In this chapter, we introduce the design and working principle of our ultrasonic micromotor. Upon successful demonstration of rotation of single ultrasonic micromotor, we present results on actuation and direction control of multiple gear-coupled surface micromachined ultrasonic motors. The rotation rate of an ultrasonic micromotor depends on the drive voltage and frequency among several other factors. The direction control of the motor has been addressed before by segmentation of PZT electrodes and by exciting different electrodes at different phases [38]. However, the mechanism of this process was not clearly understood and unpredictable due to variations in the PZT-die/silicon-die bond. It is found that the direction of rotation of motor is repeatable at each drive frequency at which rotation is observed. Due to nonlinearities involved in vibration of flexible structures, the exact relation between direction of rotation and the drive frequency could not be derived and variations in the initial position of the rotor is a variable that is hard to control. Having the prior knowledge of direction of rotor motion at different frequencies, we present a new and superior method of controlling the direction of micromotor with fewer interconnects. This capability is important to realize sub-milli-degree control of rotating stages that could be used to calibrate accelerometers and gyroscopes, mounted or co-fabricated on the rotating stages and for alignment of components on and off the rotation platform. Section 2.2 gives details of the structure of the ultrasonic micromotor, and the method of fabrication. Section 2.3 presents the actuation of the motor using bulk PZT and its

working principle. In Section 2.4, rotation rates of several motors as a function of voltage is presented. In Section 2.5, the design of three gear coupled ultrasonic motors is presented followed by mode control to achieve direction and rotation rate control.

2.2 Motor structure and fabrication

The ultrasonic motors in this thesis were fabricated using a commercial surface micromachining process, PolyMUMPS [40]. In this process, polysilicon is used as a structural material and silicon dioxide as a sacrificial layer. Sequential depositions of structural and sacrificial layers with contact and via holes in between enable fabrication of complex microstructures [41]. Figure 2.1 depicts all the layers of the PolyMUMPS process before and after release, showing a realization of an electrostatic motor.

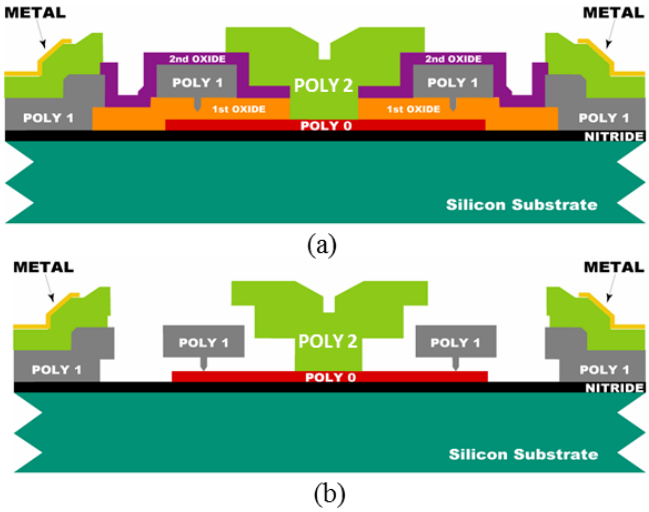

Figure 2.1 PolyMUMPS surface micromachining process showing (a) device before release and (b) after release. It consists of three structural layers Poly0, Poly1, Poly2 and two oxide layers OX1 and OX2.

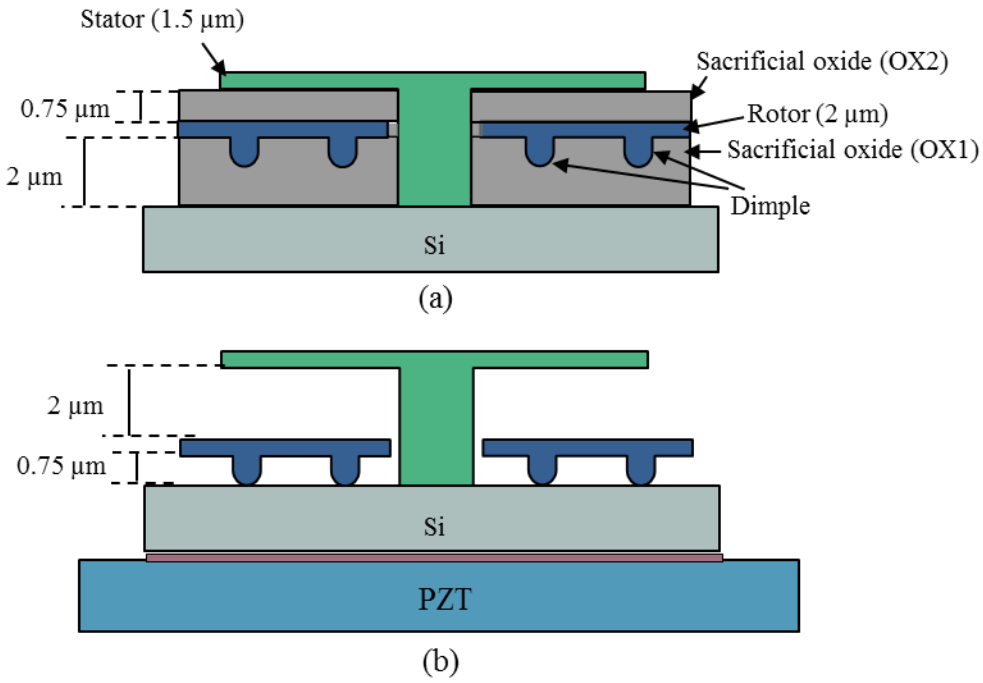

Figure 2.2 Schematic of the ultrasonic micromotor (a) before release, (b) after release

Figure 2.2 shows the schematic cross-section of the ultrasonic micromotor before and after release. The micromotor consists of three levels of polysilicon structural layers. The first structural layer at the bottom of the motor is a polysilicon layer (P0), which is deposited on top of the SiN coated, 675 µm thick substrate. An annular shaped rotor made out of 2 µm thick polysilicon layer (P1), forms the next structural layer and is separated from the P0 level by a 2µm thick sacrificial oxide (OX1). The next layer of 1.5µm thick polysilicon (P2) is used for the hub-shaped stator fabrication, and is spaced 0.75 µm above the P1 layer through another layer of sacrificial oxide (OX2). The final layer deposited and patterned is a 0.5µm thick gold layer on top of P2. The main purpose of the gold layer is to realize low resistance electrical interconnects between contact pads and the motor active areas as the sheet resistance

of even doped polysilicon is too high. MUMPS also allows fabrication of dimples that are small bumps under the P1 structures as shown in the Figure 2.2 (a), (b) and explained in detail in the process manual [40]. The height of these dimples determine the stationary spacing between rotor and the substrate after the release, since the rotor is free to move under the effect of gravity while being constrained by the central anchor of the stator. Dimples reduce the surface contact area of the rotor with the substrate which reduces the surface adhesion forces such as the van der Waals forces. The substrate-rotor spacing before and after release is illustrated by Figure 2.2 (a) and (b), respectively.

The rotor has typical outer diameters of 900-1000 μm and an inner diameter of 150 μm. The sacrificial oxide is etched through the HF chemical etch, followed by a critical point drying step which minimizes stiction between surfaces. Due to the high surface area to volume ratio of the surface micromachined rotor and stator, in order for the stator or the rotor not to get stuck to its immediate neighboring layers, atomic layer deposition of Al_2O_3 was done after the motors are released.

2.3 Piezo-actuation of MEMS

Surface micromachines can be actuated by bonding a silicon die to a piezoelectric PZT plate. This has been shown in several applications like silicon based ultrasonic surgical tools [42] and micromachined pumps [43]. This method of actuation eliminates interconnects directly to the surface micromachines and instead transfer the vibrations onto them through the substrate. The dies with the released motors are bonded to 5mm long, 3.6 mm wide, 500 μm thick rectangular PZT piezoelectric plates using cyanoacrylate adhesive (CA40). The adhesive layer thickness is designed to be

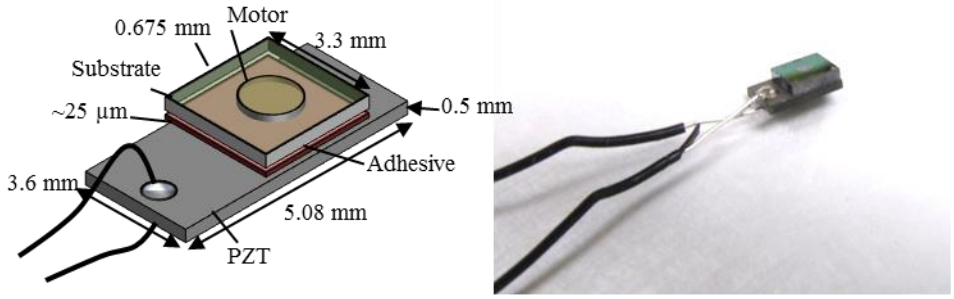

Figure 2.3 Schematic and optical image of the ultrasonic motor bonded to the PZTplate.

as thin as possible while maintaining strong bonding between silicon die and PZT plate reducing the coupling loss [See Appendix B for detailed process of bonding]. The size of the PZT plate is larger compared to the size of silicon die to provide easy handling and provide surface space for soldering wires for PZT actuation. In the future, with PCB integration and wire bonding, the size of the PZT can be

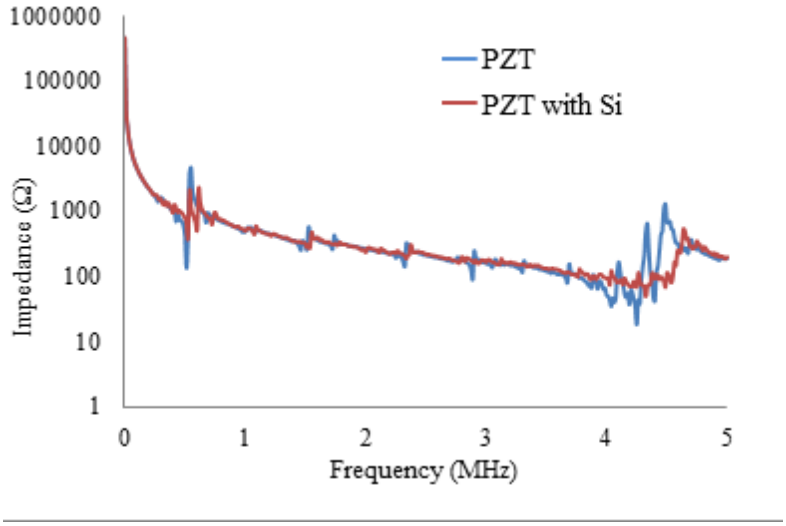

Figure 2.4 Measured impedance of PZT plate with and without Si die

significantly reduced to further increase the driving efficiency and ultrasonic motor density.

There are two stages of energy conversion process in a piezoelectric ultrasonic motor. In the first stage, when electrical energy is applied to piezoelectric PZT plate, it is converted into vibratory motion, i.e., longitudinal, transverse or flexural, depending on the frequency of excitation. The second stage of energy conversion happens when the vibratory motion of stator translates into rotary motion of rotor either through frictional coupling or acoustic streaming mechanisms. Both the stages of energy conversion can exhibit nonlinear dynamics due to nonlinear properties of the adhesive layer and the nonlinearities of flexible structures that can exceed the linear limit approximation in strain and displacements. In the conventional ultrasonic motor, a traveling wave is created on the stator by simultaneously applying two waves that are of equal amplitude and 90^{o} out of phase in both space and time on PZT, resulting in a traveling wave. As the traveling wave propagate, each surface particle of the stator draws an elliptical locus due to the coupling of longitudinal and transverse waves. So, any point on the surface of the stator has an elliptical motion. In order to realize the traveling wave, two waveform generators are needed to excite standing waves on the stator. This needs a complicated setup involving many interconnects. In our work, we present the motor whose stator is excited through single phase drive. Driving motor using single phase drive has already been tried in [8]. The reason for the ability to drive using single phase drive is attributed to wave reflections off the edges of the membrane/stator setting up parasitic traveling waves. Later, [5] also reported single phase drive actuation and our work is based on the same type of actuation. The bulk PZT-piezoelectric plate bonded to the motor is excited using a function generator at voltage up to 10 Vpp as a function of frequency. The stress waves generated are by the

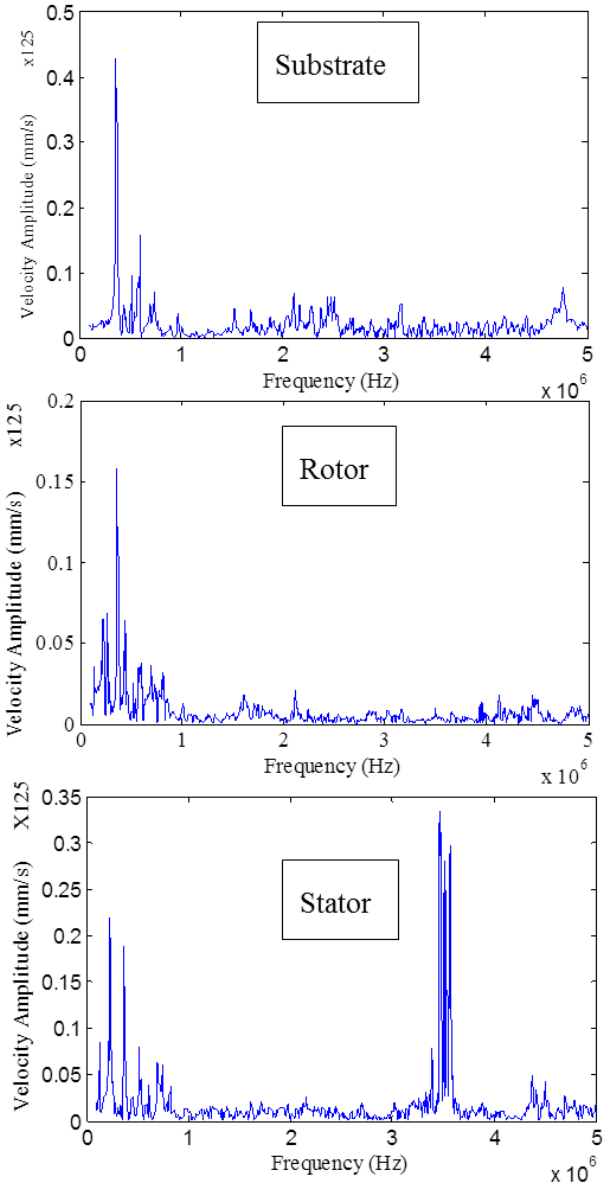

Figure 2.5 Velocity amplitude of the substrate, rotor, and stator as a function of frequency measured by Laser Doppler Vibrometer shows the resonant modes of stator at 3 to 4 MHz range, independent of the substrate and rotor resonant modes.

PZT and couple into the PZT-silicon composite structure. At the resonance frequencies of the structure, large motion can be achieved. This motion can couple into the surface micromachines by impact coupling, spalling, stress coupling through anchor, and inertial coupling. From the analysis, inertial coupling was shown to be the dominant mechanism of energy transfer [33]. Figure 2.4 shows the impedance measurements of a PZT plate and PZT/Si composite plate. As can be seen in the Figure 2.4, the PZT vibration modes are damped by the silicon plate. In the 4-5 MHz range, the first thickness mode of PZT can be seen which is again damped by the silicon glue layer. Figure 2.5 shows the velocity amplitude of the substrate, the stator, and the rotor as a function of frequency measured using Polytec Doppler vibrometer. The peaks in 1 kHz to 1 MHz range correspond to the resonance of the whole structure and can be seen in all three plots. The stator plot has high velocity amplitude in 3 to 4 MHz range which corresponds to its thickness mode resonance.

2.3.1 Response of an anchored disk on silicon substrate due to PZT induced vibrations

The vibrations of stator are recorded using Polytec^{TM} laser Doppler vibrometer. The output of the vibrometer is read through spectrum analyzer in 100 kHz to 5 MHz range as shown in Figure 2.6. The (i,j) mode resonant frequency of a free-clamped annular plate (stator in our case) can be expressed as [44]

$$f_{ij} = \frac{\lambda_{ij}^2}{2a^2\pi}\sqrt{\frac{Eh^3}{12\gamma(1-\nu^2)}} \tag{2.1}$$

where a is the stator radius, b is the anchor radius, h is the stator thickness, E is the

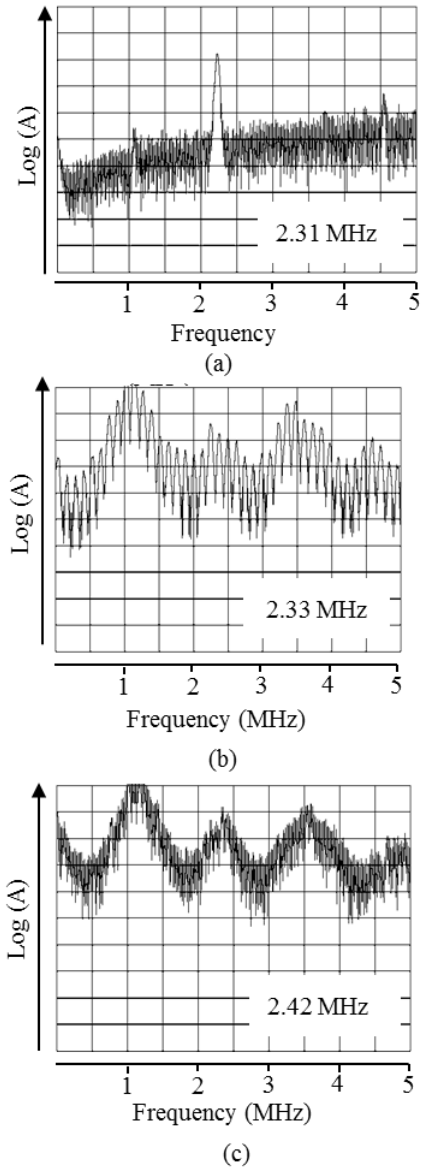

Figure 2.6 Frequency spectrum at different excitation frequencies to quantify nonlinear components creating rotation of the motor (a) 2.31 MHz, (b) 2.33 MHz, (c) 2.42 MHz which belongs to quasi-periodic regime.

Young's modulus, ν is the Poisson's ratio, γ is the mass per unit area, and λ_{ij} is the dimensionless frequency parameter, which is determined by the mode number (m,n)

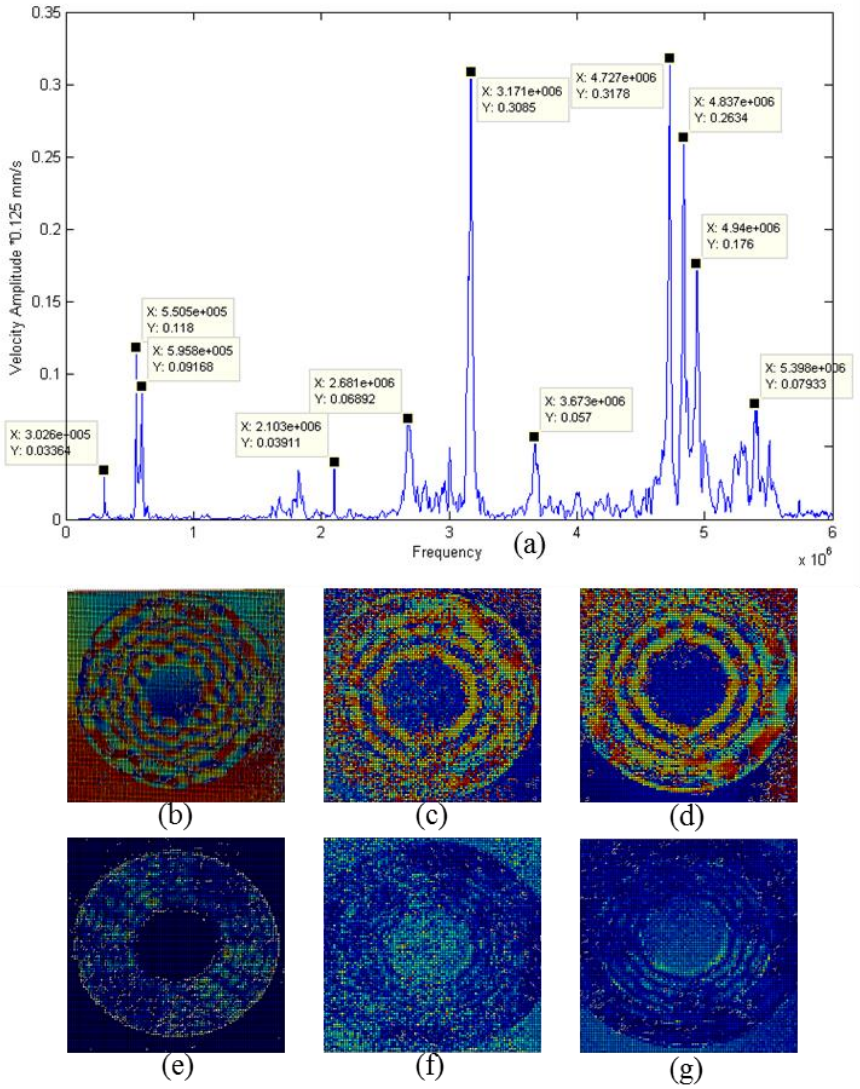

Figure 2.7 (a) Frequency sweep of ultrasonic micromotor with Doppler vibrometer shows one of the peaks at 3.17 MHz at which frequency splitting of 1.53 MHz, 1.64 MHz is observed. 2D scan of the motor showing the mode shapes at (b), (e) 3.17 MHz, (c), (f) 1.53 MHz and (d), (g) 1.64 MHz.

and the ratio between the radius of the stator, a and anchor, b. When the drive frequency is far from the resonant frequency of the stator, the spectrum analyzer shows a single frequency peak corresponding to that of the excited frequency as shown in Figure 2.6 (a). An increase in the force amplitude or a decrease in the damping leads to further bifurcations, giving sub-harmonics of order 4, 8 and so on. As the excitation frequency nears the resonant frequency which is a sign of decrease of damping, frequency splitting into number of discrete frequencies is observed as shown

in Figure 2.6 (b). From the plate vibration theory, each transverse displacement solution corresponds to two orthogonal modes, the sine component and cosine component that are degenerate in nature for a perfect plate. But, an actual plate will have some kind of imperfection either due to its fabrication errors, etch holes, lateral in-plane stresses or other factors. Due to the asymmetry of the plate, corresponding to each symmetric mode of a perfect disk, there are two modes having slightly differing frequencies in the imperfect disk. These two modes are in 1:1 internal resonance. Similarly a mode can be in internal resonance with another mode at half its frequency, called 1:2 resonance and so on. As the excitation frequency is near one of these modes that share internal resonance, the discrete peaks come together to form two to three main peaks and this is called quasi-periodic regime as shown in Figure 2.6 (c). These peaks have high amplitude due to the high quality factor of the polysilicon stator even if it is operating in air. In the quasi-periodic regime, the major peaks exhibit simple nonlinear relationship with the excited frequency. The transition from excited mode to quasi-periodic regime is a sign of distribution of injected energy among all modes what share internal resonance relationship with excited mode. The first excited mode loses stability in favor of a coupled regime [45]. When the excited frequency is close

to the highest frequency involved in the internal resonance, the traveling wave component of the highest mode can appear in the steady state response [46]. The phenomenon of frequency splitting in subharmonic modes is experimentally shown by [34]. In [34], when the PZT was excited at 3.78 MHz, two subharmonic modes, (1, 13) traveling mode at 1.78 MHz and (0, 20) standing mode at 2 MHz were observed from laser interferometer measurements which were verified by finite element simulation. When the stator was excited at 3.78 MHz that corresponds to (5, 1) mode, there occurred two orthogonal modes with slightly different frequencies. These modes sharing 1:1 internal resonance can be excited and phase-locked, resulting in a traveling wave on the stator [47][48]. The reason for the sub-harmonic vibration is said to be due to period doubling bifurcations of the system caused by the etch hole and other imperfections on the stator. In our work, in order to gain understanding about direction control, the frequency sweep of the micromotor using optical interferometer indicated the resonance peaks (Figure 2.7 (a)), at a fixed drive voltage of 300 mV_{pp}. At 3.17 MHz, there is a resonance peak and frequency splitting is observed with spectrum analyzer showing 1.53 MHz, 1.64 MHz and 3.17 MHz, the first two adding up to 3.17 MHz. Figure 2.7 (b) – (g) shows mode shapes (phase and amplitude) at these frequencies. At all the frequencies, at which the rotation is observed, frequency splitting is seen with at least 3 frequencies including the drive frequency. Among these frequencies, if z is the drive frequency, there are at least two frequencies x and y, such that x + y = z. Also, driving the motor with 2 frequencies 2x (3.06 MHz), 2y (3.28MHz) simultaneously, also showed rotation, with rotation rate slower than when the motor is driven at z (3.17 MHz) alone. In the future, one can quantify the nonlinear components as a function of design of gold coverage and drive amplitude to assess the stable operating point for the motor.

2.3.2 Motor rotation due to acoustic coupling mechanism

Once the traveling wave is formed on the stator, there are two principal ways in which rotor motion can be realized. One is the traditional way of driving ultrasonic motors through frictional coupling mechanism and the other is acoustic coupling mechanism.

In frictional coupling mechanism, the rotor is in direct contact with the stator. When the traveling wave is propagating on the stator, and the surface particle of the stator is at the top of the ellipse, it touches the rotor, and the rotor is pulled along through frictional coupling [8]. The rotor is driven in the direction that is opposite to the direction of the traveling wave. The ultrasonic micromotors that work based on friction coupling mechanism can have limited life time as there is a wear due to direct contact of stator and rotor at all times of operation. In our work, we demonstrate traveling wave lead rotary time-averaged force from acoustic streaming coupling momentum to the rotor.

Acoustic streaming is a steady current in a fluid caused due to oscillating tangential relative velocity between a fluid and a solid wall. The oscillations either originating from fluid or in solid leads to frictional dissipation within the Stokes oscillating boundary layer [49]. The acoustic streaming in the ultrasonic motor is due to the traveling wave on the stator and travels in the same direction of the wave. The force due to the acoustic streaming results from the gradient of acoustic streaming velocity in the Stokes oscillating boundary layer on the rotor [21].

From the post-buckling analysis of bilayered annular plates, the displacement and the velocity of the stator is known which serves as top boundary condition of the rotor-stator gap. The initial vertical velocity of the rotor at the excitation frequency is

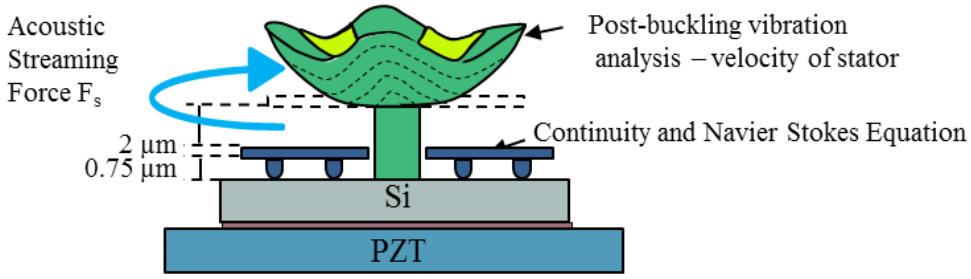

Figure 2.8 Schematic shows that from post-buckling vibration analysis of the buckled stator, and the resulting acoustic streaming induced motion.

minimal and can be neglected. This is the bottom boundary condition of the rotor-stator gap. The acoustic streaming velocity is obtained by solving continuity and Navier-Stokes equations in the air gap using these boundary conditions. From the acoustic streaming velocity $u_1 = (u_r, u_\theta, u_z)$, the acoustic shear stress is obtained [49]

$$\tau_\theta = 0.25\, B_t \rho \delta \mathrm{Re}\left[u_z \frac{\partial u_\theta^*}{\partial z} + u_\theta \frac{\partial u_\theta^*}{r\,\partial \theta} + u_\theta^* \left(i \frac{\partial u_r}{\partial r} - \nabla \cdot u_1\right)\right] \tag{2.2}$$

where B_t is the ratio of eddy kinematic viscosity and kinematic viscosity of air. Integrating $\tau_\theta$over the rotor surface, the acoustic streaming torque is

$$T_\theta = \int_{r_1}^{r_2} 2\pi r t\, \tau_\theta dr, \tag{2.3}$$

where t is the thickness of the rotor. The acoustic streaming torque acting in the tangential direction of the rotor couples the traveling wave on the stator to the rotor and pushes the rotor in the same direction as the traveling wave.

While the acoustic streaming torque assists in the rotation of the rotor, the drag torque, squeeze film damping torque and friction torque oppose the rotation. The balance between these torques results in constant rotational velocity of the rotor.

2.4 Ultrasonic motor characteristics

Power Calculation

The drive voltage of 10 Vpp corresponds to RMS voltage of 3.53 V. At drive frequency of 525 kHz, the impedance as measured from Figure 2.4 is 384 Ω. The corresponding power consumption at this voltage and drive frequency is 32 mW (V_{RMS}^2/R). If we consider drive voltage of 4 Vpp, the power consumption at resonance is 5 mW. At different drive frequencies, the impedance varies and the power consumption measured at several combinations of voltage and frequencies at which motor showed rotation is in 5 to 60 mW range. Table 2.1 shows operating and performance parameters of the ultrasonic micromotor.

Table 2.1 Operating and performance parameters of the ultrasonic micromotor.

Motor – Operating and performance parameters	
Drive Voltage	4 – 10 Vpp
Power	5 – 60 mW
Stage volume	0.182 cc
Wobble	1.2 mradians
Smallest angular movement detected	50 milli-degrees

2.4.1 Rotation rate

Our motor designs incorporated gold pads and diffraction gratings at the edge of the rotor to measure the rotational speed. The experimental set up for this measurement, shown in Figure 2.9, uses a He – Ne laser that is directed towards the edge of the rotor, which upon reflection is measured by a photo detector (Thorlabs DET36A).

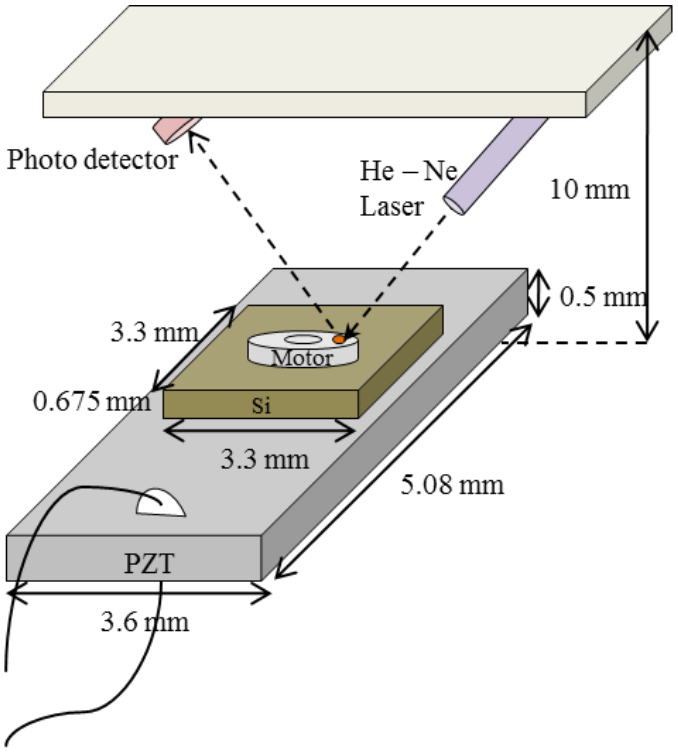

Figure 2.9 Schematic of the ultrasonic micromotor set up with VCSEL and photo detector to measure the rotation rate.

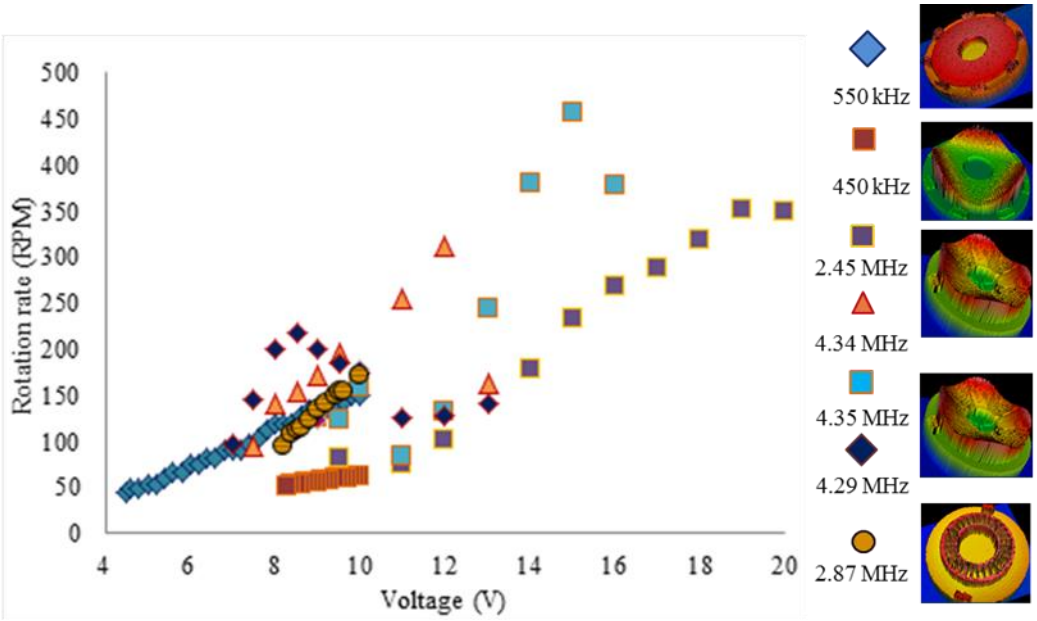

Figure 2.10 Rotation rates of various micromotors with voltage.

During the rotation of the motor, the reflectivity difference between gold and polysilicon is used to derive the rotation rate. Based on the number of peaks in a given time interval and the number of gold pads on the edge of the rotor, rotation rate of the motor is calculated. For example, four diffraction gratings on the edge of the rotor shown in Figure 2.9 causes 4 Hz photodiode signal for a rotation rate of 60 RPM.

Figure 2.10 shows the rotation rates of various designs of motors at several frequencies. Shown in the right of the figure are 3D images (vertical to lateral dimensions - not to scale) of various designs of motors. From this plot, we note that rate of rotation rate with voltage increases with frequency. At higher frequencies (>4 MHz), the rotation rate follows nonlinear trend with voltage due to excitation of several other modes that do not contribute to the rotation of the motor.

2.4.2 Burst mode operation

In the burst mode actuation, PZT is driven inputting the number of drive cycles. From this measurement, a rotation angle of 2 degree per thousand cycles with

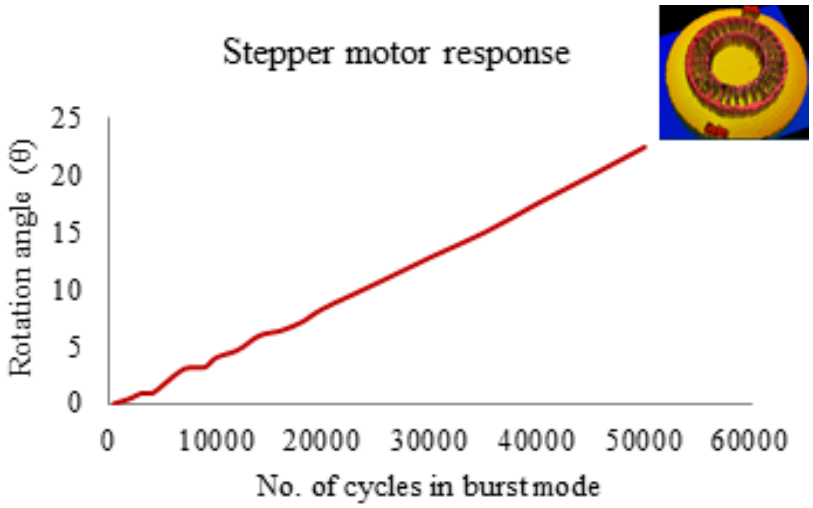

Figure 2.11 Burst mode actuation of the slot stator ultrasonic motor design

an accuracy of 0.05 degree is achieved, and the accuracy could be further increased with more accurate angle measurement equipment. Figure 2.11 shows step response in rotation angle of the motor.

2.4.3 Effect of frequency splitting rotor motion

The rotation of the motor is observed when the drive frequency induced vibrations of the stator leads to new vibrations of the stator that share internal resonance relationship with the drive frequency.

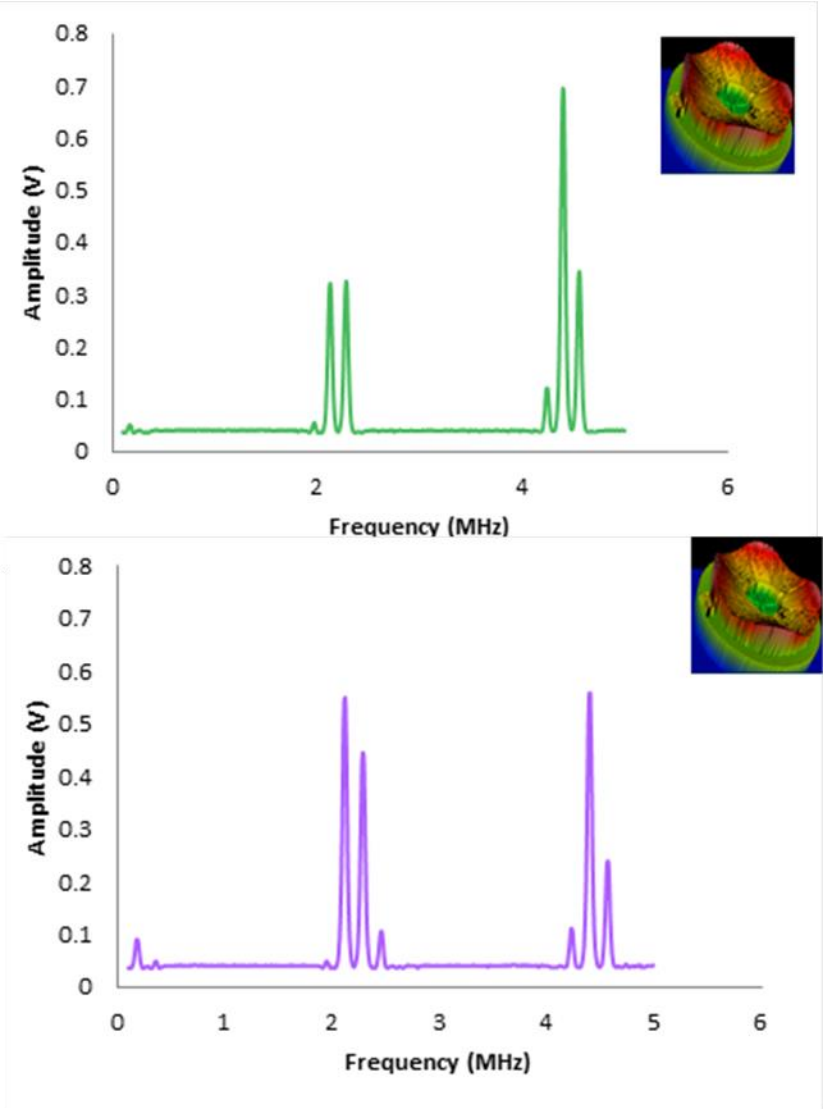

Figure 2.12 Spectrum analyzer measurements of the motor shown in inset at (a) 4.38 MHz, (b) 4.39 MHz. Motor rotated CCW at 4.38 MHz and CW at 4.39 MHz. During the rotation of the motor, the amplitudes of the subharmonic modes at half the frequency changed from 4.38 MHz to 4.39 MHz.

High frequencies (>2 MHz): At high drive frequencies, the rotation of the motor was not observed in the absence of frequency splitting as shown in Figure 2.6(a). When the

vibration of the stator is significantly high, splitting into three or more frequencies is noticed. Among these, there are at least two frequencies that add up to the drive frequency. If the envelope of split frequencies is discrete in nature as in Figure 2.6 (b), rotation is still not observed. Only when the neighboring frequencies in the envelope form a continuous band with fewer identifiable peaks and valleys as in Figure 2.6(c), rotation of the motor is observed. Compared to the neighboring drive frequencies, change in the number of split frequencies or significant change in the amplitude at any of the frequencies can initiate rotation. The direction of the rotor changed due to change in the envelope shape of the band or lowering of amplitudes of all frequencies in a band. The shape of the envelope changes when the amplitude of one of the frequencies changes significantly (Figure 2.12) or at least one of the split frequencies appear/disappear. The band shape becomes sharper for very high speed rotations.

At very few frequencies, the rotor is seen to fluctuate due to favoring of both clockwise and counterclockwise modes. The vibration of the rotor at these frequencies is so high that it effects the reliable functioning of the motor. Knowledge of these frequencies is very essential to avoid operating at the same for stable and reliable functioning of the motor.

*Low Frequencies (< 2MHz)***:** At these frequencies, the impedance is lower and the rotation is observed even in the absence of splitting of frequencies. The change in the direction of rotor is observed when there is a significant change in the amplitude at the drive frequency compared to the neighboring frequencies. If a vibrating mode at a frequency prefers a particular direction, rotation is initiated only when the amplitude at

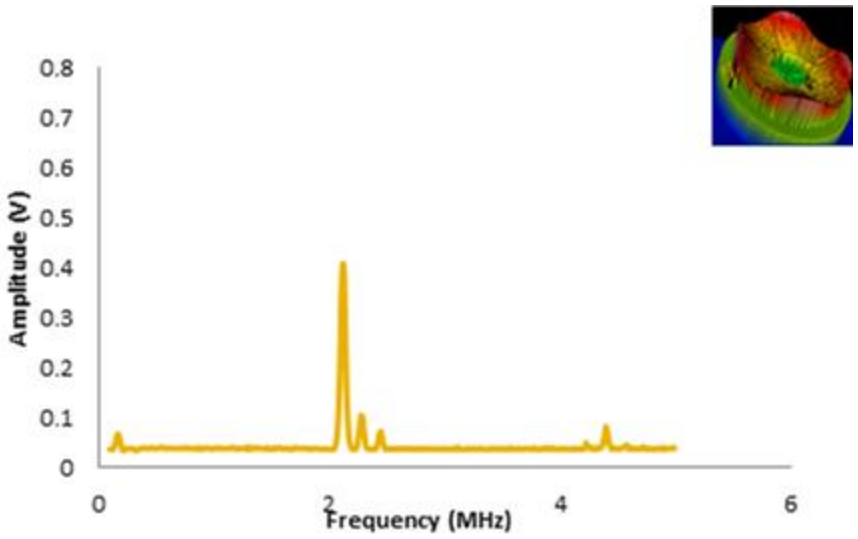

Figure 2.13 Two similar motors (one in this plot and one motor in the Figure 2.12 (b)) from different dies rotate in the same direction (CW) at 4.39 MHz.

that drive frequency is higher than a threshold value and it should be even higher to realize continuous rotation of motor.

Initial experiments indicate repeatability in the direction of rotation of two different dies at a particular frequency (Figure 2.13)

The rotation rate of an ultrasonic micromotor does depend on the drive voltage and frequency among several other factors. Testing of several ultrasonic micromotors does not give useful information on how the direction of the micromotor rotation is governed by other factors, but the direction of rotor motion at each frequency seems to be same with good repeatability. The direction control of the motor has been addressed before by segmentation of PZT electrodes and by exciting different electrodes at different phases [38]. However, the mechanism of this process was not clearly understood. Having the prior knowledge of direction of rotor motion at

different frequencies, in the next section, we present a new and superior method of controlling the direction of micromotor with fewer interconnects.

2.5 Gear coupled motors

In this section, we present actuation and direction control of multiple gear-coupled

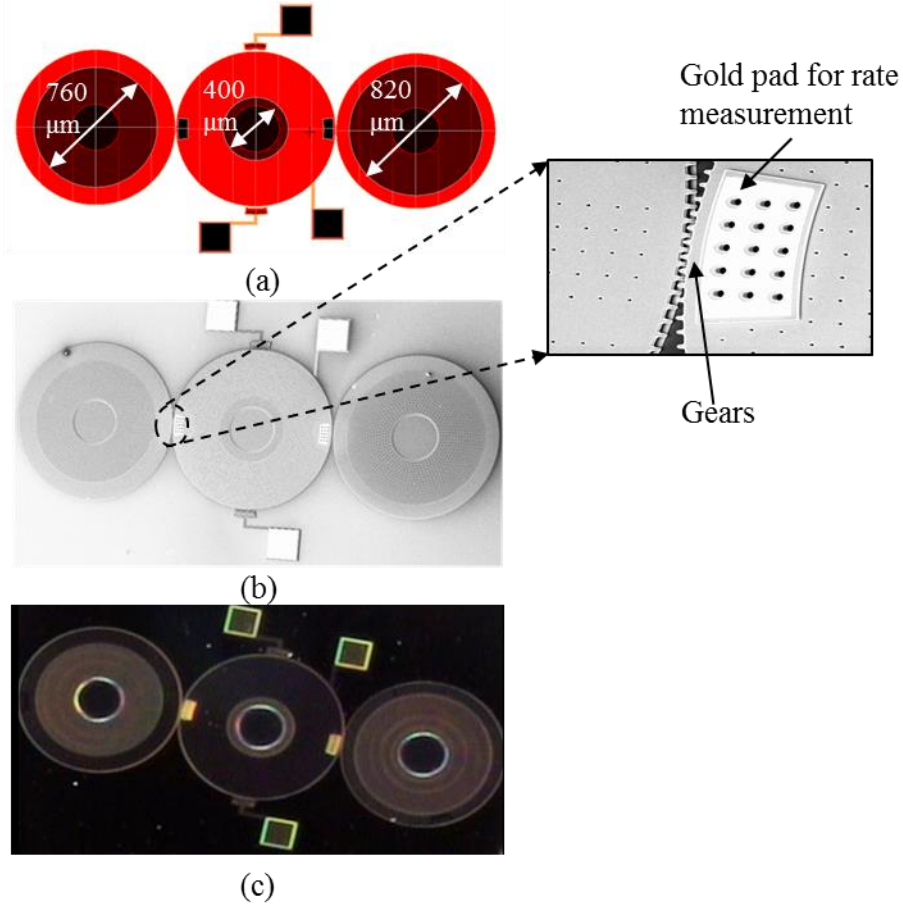

Figure 2.14 (a) Schematic of the three ultrasonic motor structure, (b) SEM of the structure fabricated in MUMPS process flow with inset showing adjacent motors connected by gear teeth, (c) optical micrograph of the three motors.

surface micromachined ultrasonic motors. Using three whispering gallery mode micro ultrasonic motors (WGMMUMs) with different flexural resonances, the center motor motion is controlled to rotate clockwise (CW) and counter-clockwise (CCW) direction at controlled rotation speeds.

2.5.1 Mode control

The three rotors shown in Figure 2.14 have thickness of 2 μm and diameter of 974 μm. The left and right stators are designed to resonate at different frequencies allowing independent operation to drive the central motor. The central motor stator is much smaller in diameter and so its resonance frequencies are too high to excite its rotor on its own, at frequencies chosen to drive the coupled motor structure. The mode shapes at which left motor and right motor showed rotation are in Figure 2.15. The left and right motors have stators that can actuate their rotors, in the 100 kHz to 5 MHz frequency range. The frequency response of the left and right motor stators from Laser interferometer is shown in Figure 2.16. The dimensional difference between the two

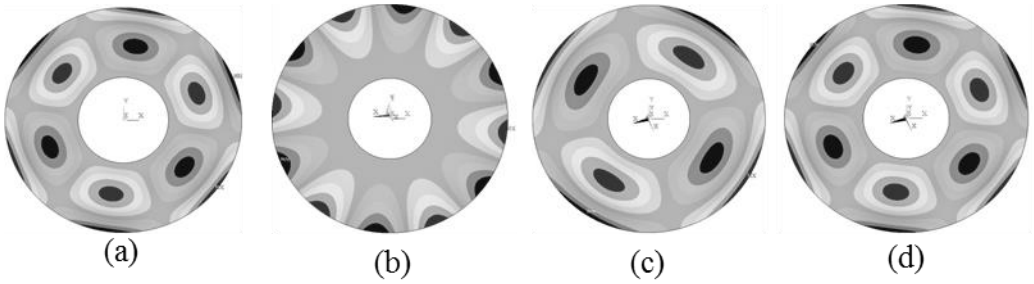

Figure 2.15 Finite element simulation of mode shape at (a) 390 kHz for the left stator-rotor rotated CCW, (b) 225 kHz for the right stator-rotor rotated CCW, (c) 267 kHz for the right stator-rotor rotated CCW, (d) 215 kHz for the right stator-rotor rotated CW.

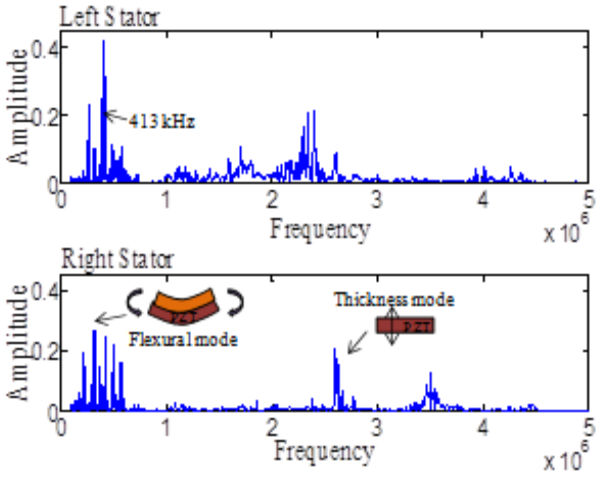

Figure 2.16 Top and middle show optical interferometer data on for left and right motor stator. Note the difference response due to different stator size.

stators (Left diameter = 380 µm, Right diameter = 410 µm) led to change in resonance frequency of similar mode shapes as predicted by analysis.

Table 2.2 Procedure for central motor rotation at either direction by exciting left and right motors at different frequencies.

Actuation Frequency	Left Motor	Central Motor	Right Motor
f_1	No Rotation	Rotates CW	Rotates CCW
f_2	Rotates CW	Rotates CCW	No Rotation

motion. Figure 2.17 shows different cases of rotation of the side rotors that controlled the rotation of the central rotor. When either left or right rotor alone rotates, it rotates the other two motors. The central rotor also rotated by traveling wave (TW) of either

Table 2.3 Combinations of direction of rotation of left, right rotor resulting in central rotor motion.

Cases of rotation and direction of three motors			
Case	Left Motor	Central Motor	Right Motor
A	CW drive	CCW driven	CW driven
B	CCW drive	CW driven	CCW driven
C	CW driven	CCW driven	CW drive
D	CCW driven	CW driven	CCW drive

Table 2.3 shows the frequencies the side rotors were driven resulting in center rotor left or right rotors, indicating that the draft force from the side stator-rotor coupling is strong enough to rotate the central rotor. When both the side rotors rotated in the same direction but at different speeds, all three rotors rotated in the direction and at the

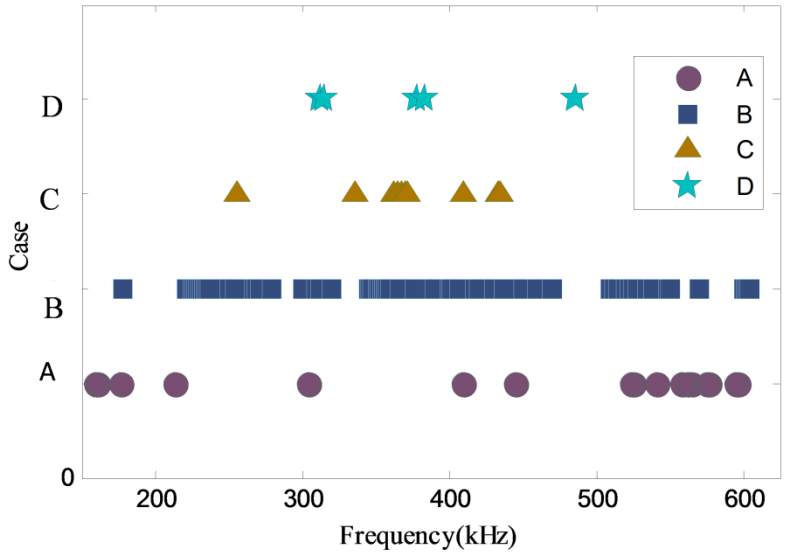

Figure 2.17 Different combinations of rotation achieved at different frequencies. The data points correspond to the actuation schemes shown in Table 1.2

speed of the greatest speed rotor. When the left and right motors were rotating in opposite directions at the same speeds, the central rotor remained stationary.

2.6 Conclusions

Several designs of motors are tested for their rotation rate variation, angular control, reliability, wobble, direction control to ultimately enable the motor as a rotating platform for other micro-devices to be placed on the motor. The rotation in the motor is caused due to acoustic streaming force in the rotor-stator gap that couples the traveling wave on the stator and pushes the rotor in the direction of traveling wave. The rotation rates for different motor designs at several frequencies are presented.

We demonstrated the speed and direction control using the three-gear coupled WGMMUM motor design. Based on the drive frequency, the side motors can rotate CW or CCW and in – turn rotate the central motor in the opposite direction through gear coupling. A micromotor which cannot rotate by itself could be made to rotate through gear coupling of the side rotors at different speeds and at desired direction of rotation. The side rotors have stators on top of them covering most of the rotor area. The applications where external devices are to be mounted on a rotating platform can use the central rotor which has larger surface area compared to the side rotors. While gear coupling of motors was successfully demonstrated, there are some limitations as well. After release of motors, the rotors have some upward curvature due to release of prior residual stresses. These residual stresses and hence the curvature vary from motor to motor. Due to the curvature of the rotor, proper engagement of gears is not always ensured that can lead to slip or non-uniform rotation of the motor. Curvature control can be realized by selective patterning of layers which is a subject of Chapter 3.

Chapter 3

EFFECT OF STATOR-ROTOR GAP MODULATION ON MOTOR PERFORMANCE

3.1 Outline

In this chapter, we investigate the effect of modulating the stator-rotor gap on rotor by varying the built-in stresses on the stator. New designs of stator with variation of built-in stress by selective patterning of gold on stator are introduced in section 3.2. Non-contact actuation and sensing will ensure control of the rotation platform with as little physical contact as possible, increasing reliability, life time and eliminating interconnects and other artifacts that are common in solid-solid contact motors. Section 3.2 presents additional features implemented on ultrasonic micromotors to demonstrate non-contact optical means of measurement and non-contact motor control. During the release of motors, the built-in stress results in stator curvature due to buckling phenomenon. The detailed characterization of stator curvature and buckling phenomenon is presented in section 3.3. In section 3.4, several characteristics of the ultrasonic micromotors including rotation rate variation with voltage, curvature variation with temperature are presented. We present successful demonstration of controlled levitation of the ultrasonic micromotor during its rotation in section 3.5.

3.2 Design features for optical metrology and rotor gripping

In order to demonstrate non-contact optical means of measurement and non-contact motor control, additional features are included in the ultrasonic micromotor

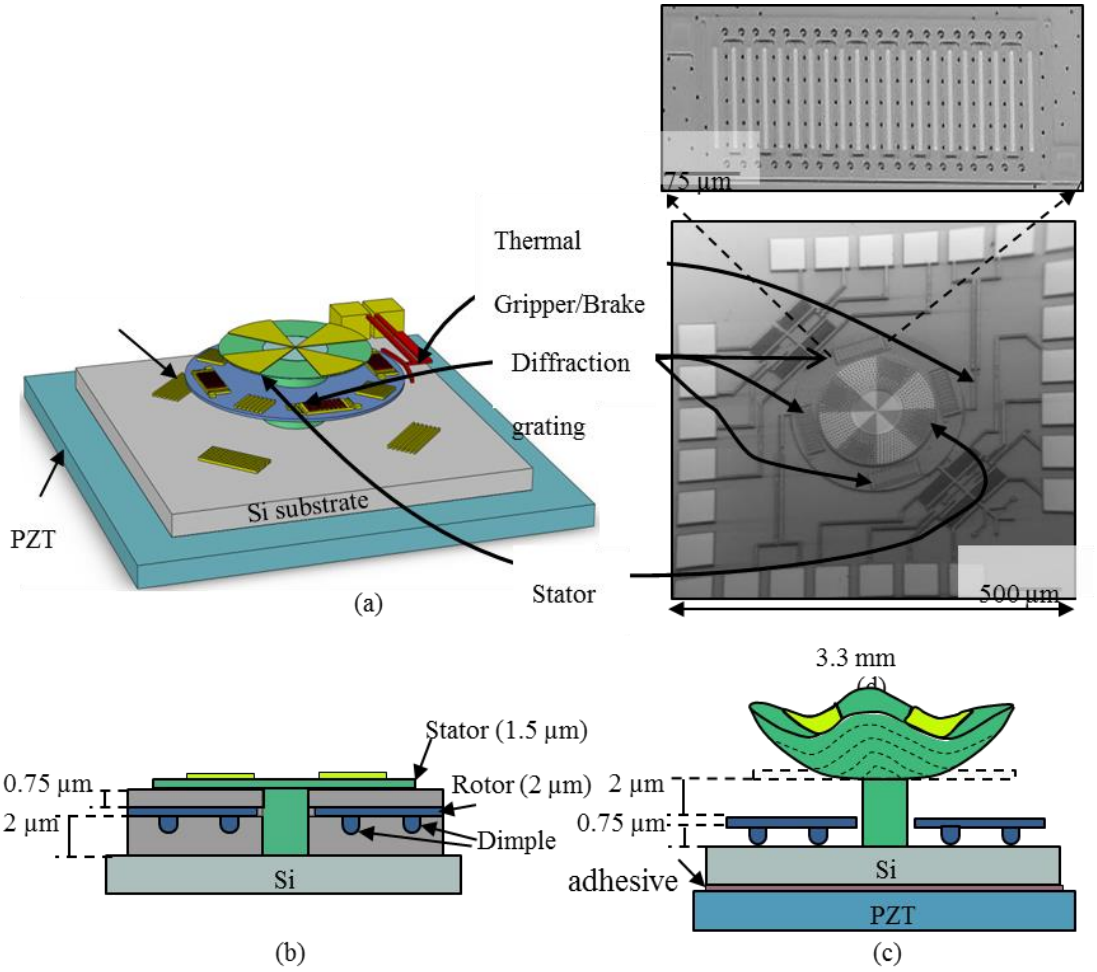

Figure 3.1 (a) Schematic of ultrasonically driven micromotor with integrated grating accelerometer. A thermal actuator is used to move a gripper close to the spinning levitated motor, (b) Cross-sectional view of the motor before release, (c) Cross-sectional view of the motor after release, (d) SEM of the motor on a substrate, inset showing the diffraction grating that can be used as an integrated accelerometer and to measure rotational speed of the motor.

design. Gold patterns are formed on the stator to develop curvature through the combination of tensile stress in gold layer and compressive stress in polysilicon layer

leading to local curvature and ripples as a result of bimorph action with underlying silicon layer as can be seen in Figure 3.1 (c). The curvature is a function of temperature, as both thermal expansion and stress cause change in elastic coefficients and the curvature of the gold and polysilicon composite. Gold thin film patterns are also formed on the rotor, stator and the substrate to form diffraction gratings that create optical diffraction patterns when laser beam is reflected off them. These diffraction gratings allow optical measurement of the relative angular position of the rotor with the pattern being imaged using a CMOS camera. There are two types of gratings on the rotor, one solidly anchored and the other on a compliant structure. When there is an external acceleration, the relative motion between these two gratings can be optically measured through their diffraction patterns. Hence they serve as integrated accelerometers on the rotor.

In Figure 3.1, we also have thermal actuators that can move grippers towards the spinning rotor to control the gap between the actuators and the rotor, and hold it in place during sensor operation, or control its rotation rate.

3.3 Stator curvature and buckling

After the release of motors, by etching the sacrificial silicon-dioxide layers in HF, the rotor and the stator out-of-plane deformation is measured by the ZYGO optical profilometer (New View 7300) as given in Figure 3.2. The stator (polysilicon layer)

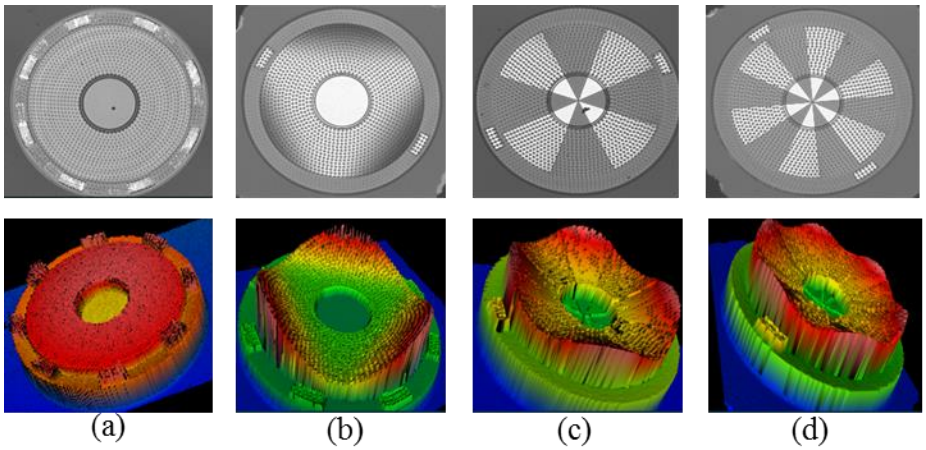

Figure 3.2 Motor stators with different patterns of gold leading different curvatures (a) no gold, (b) completely covered with gold, (c) covered in 4 sectors, (d) covered in 6 sectors. The bottom four images are 3D profiles of corresponding top (with horizontal to vertical dimensions not to scale) recorded using ZYGO optical profilometer, (e) SEM image of stator completely covered with gold, (f) SEM image of stator (c)

that is not covered with gold is flat after the motor release as shown in Figure 3.2(a). When the stator is completely covered with gold as shown in Figure 3.2 (b) or partially covered in sectors as in Figure 3.2(c), (d), it has scalloping pattern after the release process as can be seen in the bottom images of Figure 3.2 (b), (c), (d).

In literature, few bilayered plates were shown to have this scalloping pattern. In [51][52], rectangular bilayered plates were shown to have bifurcation of curvature upon temperature change of the plate with increasing curvature in x direction and decreasing curvature in the y direction or vice versa. Figure 3.3 (a) shows a bilayer buckled focusing mirror and the buckling pattern in it is similar to the pattern of

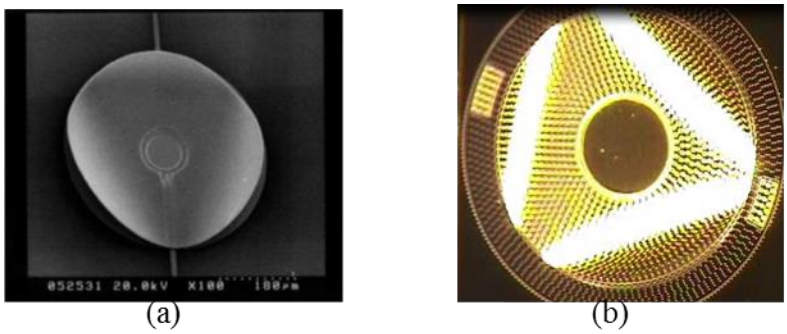

Figure 3.3 (a) A buckled focusing mirror [51][53] (b) optical image of motor shows similar buckled pattern of stator.

ultrasonic motor stator that is completely covered with gold as seen in Figure 3.3 (b). Figure 3.4 shows the polysilicon layer that is initially under compressive residual stress prior to its release. The polysilicon layer is released in HF and with increase in HF etching time, as the layer gets released from its outer radius, it slowly folded into a buckled state and formed wavy pattern with number of waves reducing with increase released area with an increased etching duration. It was also shown that if the layer to

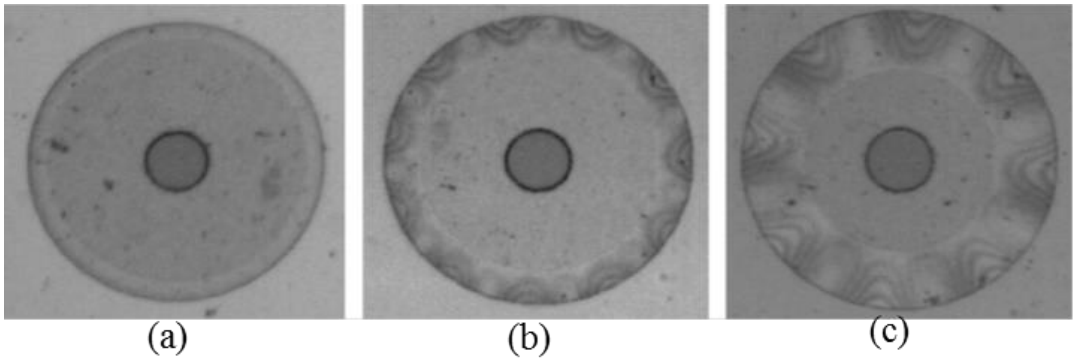

Figure 3.4 Three characteristic evolutions of buckling patterns of a circular microstructure during etching with HF show that buckling pattern does depend on the plate size. At different times of HF release, buckling of stator pattern is recorded [54].

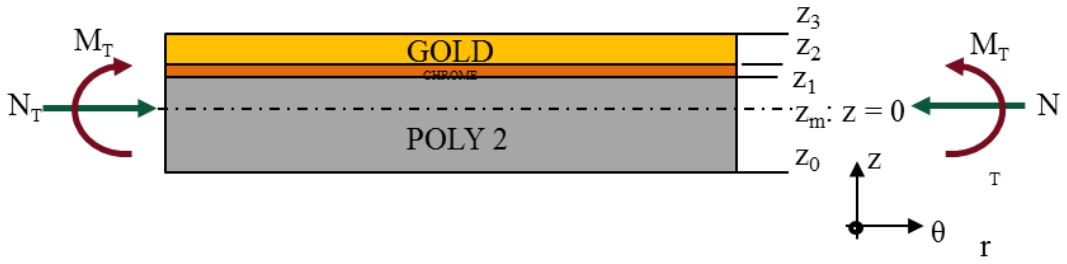

Figure 3.5 Multi-layered stator comprising of polysilicon, chrome and gold layer. The thicknesses of these three layers are comparable. Gold layer is evaporated at 110oC and when the stator is operated at room temperature, due to the difference in coefficient of thermal expansion of the three layers, there will be in-plane plate force and thermal bending moment on the stator.

be released has prior tensile stresses, then it forms an axisymmetrical bowl-like structure and only when the layer is in compressive stress, does the wavy pattern observed based on inner to outer radius ratio of the anchored layer. Although experimental results of the bilayer buckling are presented in few papers in literature, analytical proof of buckling was not shown. In our work, we present the detailed analysis of bilayer buckling. Consider the cross-section of the stator that is completely covered with gold as shown in Figure 3.5. Along with gold and polysilicon, there is a 0.2 μm chrome layer in between, to increase the adhesiveness of the gold layer to polysilicon layer. The maximum temperature during E-beam evaporation of gold is 110^{o}C and the motor is operated at room temperature. So, there is a temperature difference of about 90^{o}C from deposition. The thermal expansion coefficient of these three layers is different and due to the temperature difference of 90^{o}C, there will be thermal in-plane forces as well as thermal bending moment on the stator before release.

Table 3.1 Elastic Modulus E, Poisson's ratio (ν), thermal expansion coefficient (α) of polysilicon, gold, chrome.

Properties	E (GPa)	α (ppm/^{o}C)	ν	Thickness (μm)	
Poly Si	163	3.1	0.22	$z_1 - z_0$	1.5
Cr	278	7.9	0.22	$z_2 - z_1$	0.2
Au	78	15.4	0.42	$z_3 - z_2$	0.5

For the bilayers with the film thickness less than 5% of thickness of the substrate, the well-known Stoney equation can be used to assess the stress within the film. In our bilayer design, the thicknesses of different layers are comparable and hence the buckling pattern is modeled based on Von-Karman plate theory.

Let

- K be effective flexural rigidity of the layers
- u, v, w be the displacement of the multilayered stator in r, θ and z direction
- ε_{rr}, $\varepsilon_{\theta\theta}$, $\varepsilon_{r\theta}$ be radial, tangential and shear strains
- N_r, N_θ, $N_{r\theta}$ be the in-plane plate forces
- M_r, M_θ, $M_{r\theta}$ be bending moments
- σ_R be the residual stress
- V be the total potential energy of the system which is the combination of strain energy and work done by external load.

Assume v = 0, u = u(r), w = w(r,θ).

From the properties of polysilicon, gold and chrome from Table 3.1, effective flexural rigidity is calculated.

$$K = C - B^2/A \qquad (3.1)$$

where

$$C = \sum_{k=1}^{3} \frac{E_k(z_k^3 - z_{k-1}^3)}{3(1-\nu_k^2)} \tag{3.2}$$

$$B = \sum_{k=1}^{3} \frac{E_k(z_k^2 - z_{k-1}^2)}{2(1-\nu_k^2)} \tag{3.3}$$

$$A = \sum_{k=1}^{3} \frac{E_k(z_k - z_{k-1})}{1-\nu_k^2} \tag{3.4}$$

From classic plate theory, the corresponding strains are [55]

$$\varepsilon_{rr} = \frac{\partial u}{\partial r} - z\frac{\partial^2 w}{\partial r^2} + \frac{1}{2}\left(\frac{\partial w}{\partial r}\right)^2 = u_{,r} - zw_{,rr} + \frac{1}{2}\left(w_{,r}\right)^2 \tag{3.5}$$

$$\varepsilon_{\theta\theta} = \frac{u}{r} - \frac{z}{r}\left(w_{,r} + \frac{1}{r}w_{,\theta\theta}\right) + \frac{1}{2}\left(\frac{1}{r}w_{,\theta}\right)^2 \tag{3.6}$$

$$\varepsilon_{r\theta} = \frac{1}{2}\left(\frac{1}{r}w_{,r}w_{,\theta} - \frac{2z}{r}\left(w_{,r\theta} - \frac{1}{r}w_{,\theta}\right)\right) \tag{3.7}$$

When stator is completely covered with gold, the in-plane plate forces and bending moments [55] are

$$N_r = \sum_{k=1}^{3} \int_{z_{k-1}}^{z_k} \left(\frac{E_k}{1-\nu_k^2}(\varepsilon_{rr} + \nu_k\varepsilon_{\theta\theta}) - \frac{E_k\alpha_k}{1-\nu_k}\Delta T + \sigma_{Rk}\right)dz \tag{3.8}$$

$$N_\theta = \sum_{k=1}^{3} \int_{z_{k-1}}^{z_k} \left(\frac{E_k}{1-\nu_k^2}(\varepsilon_{\theta\theta} + \nu_k \varepsilon_{rr}) - \frac{E_k \alpha_k}{1-\nu_k} \Delta T + \sigma_{Rk} \right) dz \tag{3.9}$$

$$N_{r\theta} = \sum_{k=1}^{3} G_k \, 2\varepsilon_{r\theta}(z_k - z_{k-1}) \tag{3.10}$$

$$M_r = \sum_{k=1}^{3} \int_{z_{k-1}}^{z_k} \left(\frac{E_k}{1-\nu_k^2}(\varepsilon_{rr} + \nu_k \varepsilon_{\theta\theta}) - \frac{E_k \alpha_k}{1-\nu_k} \Delta T + \sigma_{Rk} \right) z dz \tag{3.11}$$

$$M_\theta = \sum_{k=1}^{3} \int_{z_{k-1}}^{z_k} \left(\frac{E_k}{1-\nu_k^2}(\varepsilon_{\theta\theta} + \nu_k \varepsilon_{rr}) - \frac{E_k \alpha_k}{1-\nu_k} \Delta T + \sigma_{Rk} \right) z dz \tag{3.12}$$

$$M_{r\theta} = \sum_{k=1}^{3} G_k \, \varepsilon_{r\theta}(z_k^2 - z_{k-1}^2) \tag{3.13}$$

According to the principle of minimum potential energy, the system is stable equilibrium if and only if the change of total potential energy corresponding to any sufficiently small kinematically admissible displacement is positive.

$$\Delta V = V - V_0 = \delta V + \frac{1}{2!}\delta^2 V + \frac{1}{3!}\delta^3 V + \cdots \tag{3.14}$$

For an infinitesimally small variational displacement, terms on the right hand side are linear, quadratic etc., respectively. The potential energy of the system in the equilibrium configuration is stationary results in

$$\delta V = 0 \tag{3.15}$$

Therefore the sign of second variation determines the sign of ΔV and stability of the system. The system is in stable mode for positive values of the second variation and in unstable mode for negative values of the second variation. Thus, the vanishing of

second variation is defined as the criterion of losing stability of the system or in other words, the onset of buckling, known as Trefftz criterion [56], i.e.,

$$\delta^2 V = 0 \tag{3.16}$$

The Von Karman equation for a thin linearly elastic isotropic plate in polar coordinates is derived from the Trefftz criterion [55]:

$$K\nabla^4 w = N_r w_{,rr} - 2N_{r\theta}\left(\frac{1}{r^2}w_{,\theta} - \frac{1}{r}w_{,r\theta}\right) + N_\theta\left(\frac{1}{r}w_{,r} + \frac{1}{r^2}w_{,\theta\theta}\right) - \frac{1}{\nu}\nabla^2 M_T \tag{3.17}$$

where N_r, $N_{r\theta}$, N_θ are in-plane pre-buckling forces, M_T is the thermal bending moment.

The thickness of each layer as shown in Table 3.1 is chosen in such a way that the in-plane forces are zero, in order to have low internal stresses to avoid curling of any released polysilicon structures. Although the thickness of each layer is chosen to avoid stresses, there is fairly high residual stress, 40 – 60 MPa of tensile stress in gold and 11 MPa of compressive stress in polysilicon, experimentally found [57]. In-plane forces and bending moments due to the residual stresses results in bowing up of bilayer and its bifurcation buckling. This bifurcation leads to local bending to minimize in-plane strain, causing waves in the circumferential direction, effectively resisting the applied bending moment [55][59].

In our case, $N_{r\theta}$ =0, $N_r = N_\theta = N_T = -\lambda' = -\sum_{k=1}^{2}\sigma_{Rk}(z_k - z_{k-1}) = \sigma_{poly}(z_1 - z_0) - \sigma_{Au}(z_3 - z_1)$ and

$$M_T = -\sum_{k=1}^{3}\left(\frac{E_k\alpha_k\Delta T}{1-\nu_k} + \sigma_{Rk}\right)\frac{(z_k^2 - z_{k-1}^2)}{2} \tag{3.18}$$

Substitution of above terms reduces the governing equation to

$$\nabla^4 w + \lambda \left(w_{,rr} + \frac{1}{r} w_{,r} + \frac{1}{r^2} w_{,\theta\theta} \right) = 0 \tag{3.19}$$

where $\lambda = \lambda'/K$

Assuming $w(r, \theta) = A(r) \cos(n\theta)$

$$A'''' + \frac{2}{r} A''' - \frac{(1+2n^2-\lambda r^2)}{r^2} A'' + \frac{(1+2n^2-\lambda r^3)}{r^3} A' + \left(\frac{n^4-4n^2-n^2r^2}{r^4} \right) A = 0 \tag{3.20}$$

The multi-layered annular stator is clamped inside and free outside. Let r_i and r_o be the inner and outer radius of the stator. The boundary conditions of the bilayered plate that is clamped at the inner radius and free at the outer radius are,

At $r = r_i$ (clamped):

1) $w = 0$ (3.21)

2) $\frac{\partial w}{\partial r} = 0$ (3.22)

At $r = r_o$ (free):

3) $K \left[w_{,rr} + \nu \left(\frac{1}{r^2} w_{,\theta\theta} + \frac{1}{r} w_{,r} \right) \right] + M_T = 0$ (3.23)

4) $\left(w_{,rr} + \frac{1}{r} w_{,r} + \frac{1}{r^2} w_{,\theta\theta} \right)_{,r} + (1-\nu) \left(\frac{1}{r^2} w_{,\theta\theta r} - \frac{1}{r^3} w_{,\theta\theta} \right) = 0$ (3.24)

The governing equation with the four boundary conditions is solved in MATLAB and the simulated displacement pattern for the stator completely covered with gold is shown in Figure 3.6. The out of plane deflection for this design of bilayered stator measured from experiments is 11.83 µm, and the value obtained from simulated model (Figure 3.6) is 11.474 µm thus validating our model.

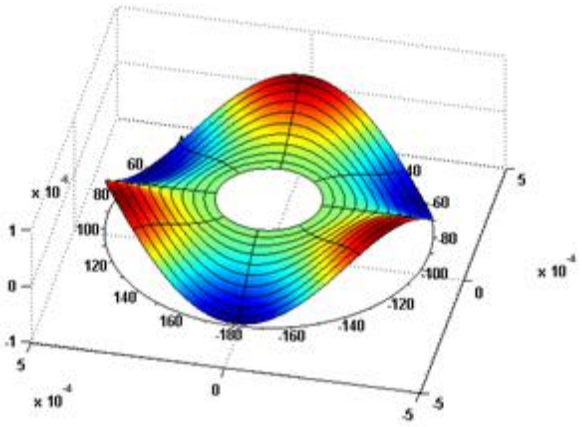

Figure 3.6 Buckling simulation of stator covered completely with gold agrees to experimentally measure of out of plane deflection.

The motors are released in HF wet chemical etch for 15 minutes. In order to verify the contribution of HF etching in the stator curvature, five motors of same design are etched with different etching times and their out of plane deflection is measured as shown in Figure 3.7. Comparing the etch time from 3 minutes to 15 minutes, there is only half a micron change in curvature. This observation suggests that the major contribution is from thermal and residual stresses.

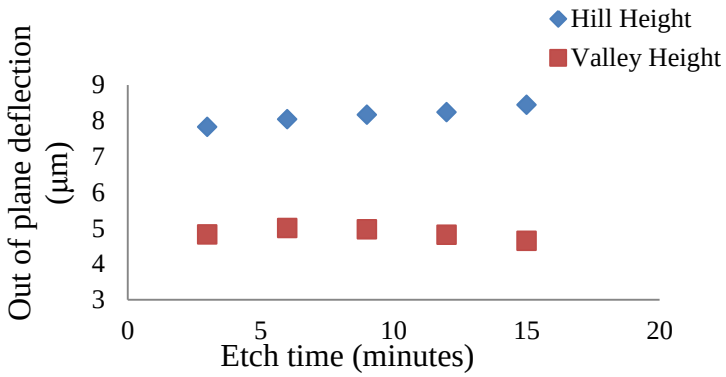

Figure 3.7 Out of plane deflection variation with HF etch time

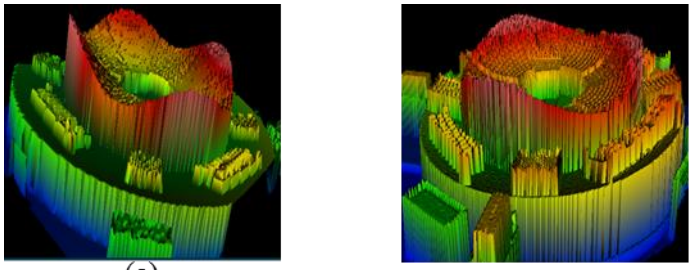

Figure 3.8 The stator has 4 peaks right after release in (a) and after excitation of the stator, due to change in residual stress from bending and with time, the buckling mode shape changed to three peaks

The number of radial patches of gold can control the number *n* of bending nulls and peaks of the stator as seen in Figure 3.2. Remarkably, the stress on the motor can change with time, probably due to slow oxidation of the polysilicon plates. Due to the bending of the stator during its actuation, the residual stress on the stator changes withtime and the buckling mode shape changes as shown in Figure 3.5 from n=4 to n=3.

3.3.1 Curvature and rotation rate variation with temperature

The stator has wavy pattern with peaks and valleys based on number of gold patches patterned on it as seen in Figure 3.2(b), (c), (d). The out of plane deflection of these peaks and valleys are shown in Figure 3.11. The rotation rate of the motor depends on the rotor-stator gap which is a function of stator curvature. In order to test the variation of rotation rate with rotor-stator gap, the temperature of motor set up is varied from room temperature to 65^{o}C using the set up shown in Figure 3.9 and the stator curvature is measured. As the sample is heated, significant microstructural changes take place in gold due to inelastic straining of gold film resulting in change of bilayer

curvature. The peak and valley height of the stator decreases with increase in temperature from 25^{o}C to 65^{o}C as seen in Figure 3.12 (a). The stator becomes flat at 65^{o}C as seen in Figure 3.10(b), (d). The decrement of curvature with temperature is also shown in [52], validating our result. Figure 3.12 (b) shows the variation of rotation rate with temperature. It can be seen that the rotation rate first increases and

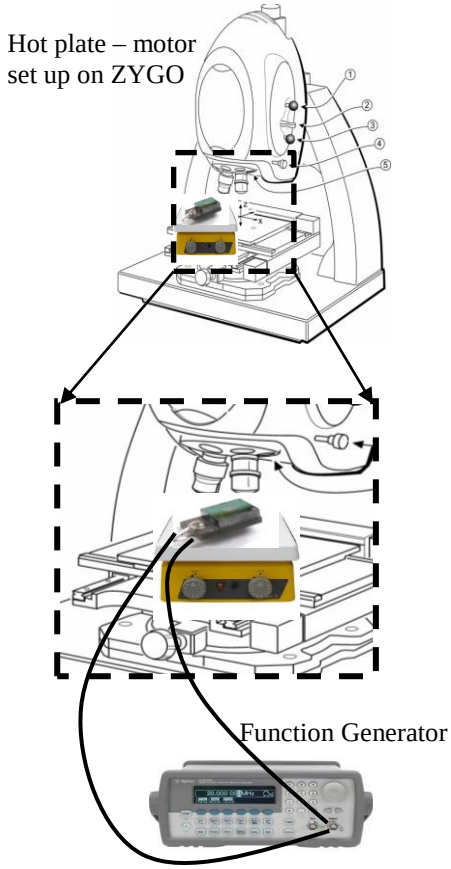

Figure 3.9 The hot plate with ultrasonic motor on it is placed on ZYGO optical profilometer stage to measure the topography of the motor from which levitation of the rotor, variation of the stator with temperature can be calculated. The motor is actuated using sinusoidal voltage provided by the function generator.

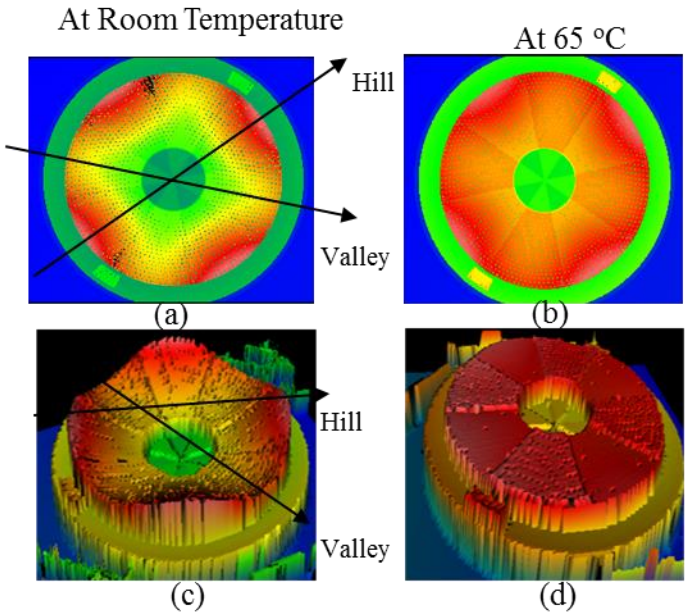

Figure 3.10 2D top view of the motor at (a) room temperature, (b) 65oC, 3D view of the motor at (c) room temperature showing the curvature bending of the stator, (d) at 65oC shows flat stator.

then reduces indicating an optimum gap that is smaller than the actual gap, which yields the highest rotation rate. Too large a gap leads to insufficient shear for drive, while too little a gap causes excessive contact force for the motor to operate.

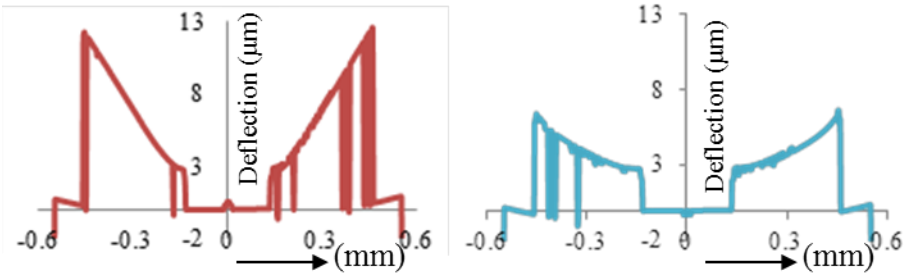

Figure 3.11 Out of plane deflection of the motor shows (a) hill, (b) valley

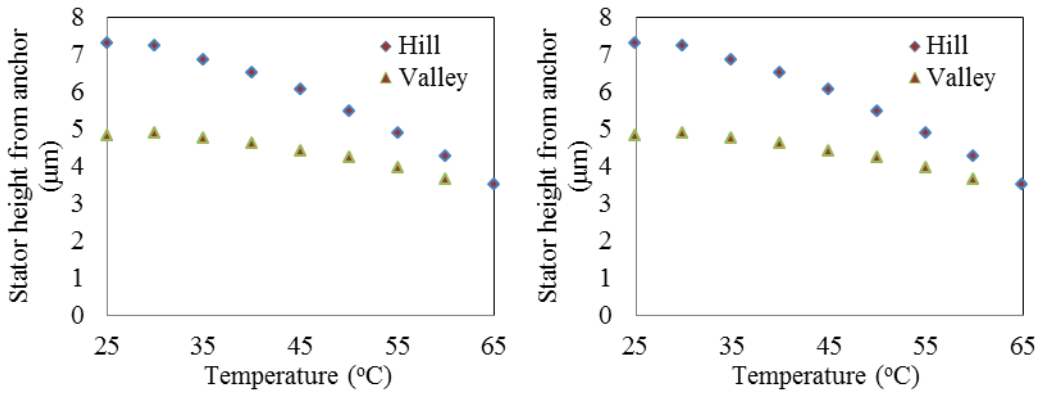

Figure 3.12 (a) Stator height decreases with temperature in a quadratic manner, (b) Rotation rate variation with temperature shows that there is an optimum curvature for highest rotation rate.

3.4 Levitation of ultrasonic motors

Levitation or suspension of rotating platforms has been tried since several decades. There are many existing proofs of principles for suspending rotating platforms in the literature. Magnetic suspension has been shown using diamagnetic rotors [60][61]. High currents are typically needed to generate sufficient magnetic field gradients for levitation. Electrostatic suspension has been achieved in implementing a spinning rotor, part of spinning gyroscope [62][63]. In these examples, relatively high voltages and vacuum are needed to achieve floatation and stable operation. An alternative to electrostatic and magnetic forces is to use fluidic forces to suspend rotating platforms. By actuating a plate at its ultrasonic resonant modes, the resulting acoustic radiation force can be used to levitate the rotor. Once levitated, the motor's smooth, frictionless motion can be used for 1D or 2D conveyor belt applications, which are extremely crucial to streamline assembly and transportation of delicate parts [27].

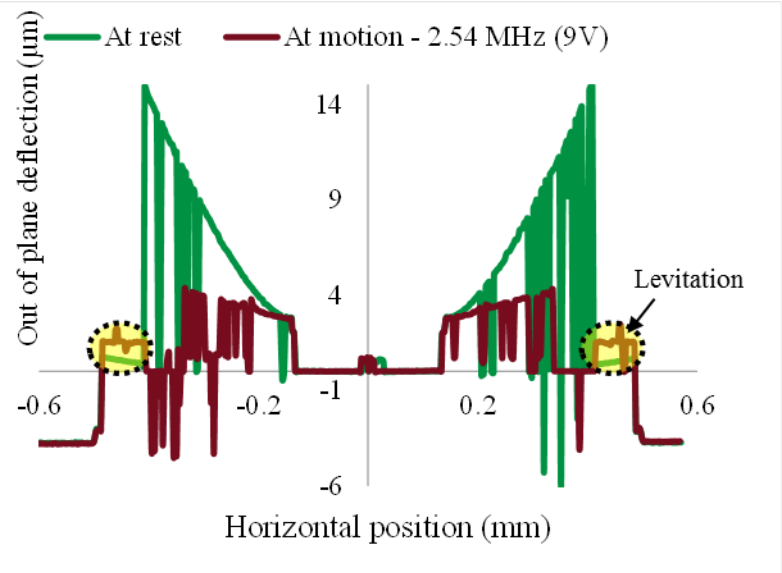

Figure 3.13 Levitation of the rotor is calculated from the difference between the out of plane deformation profile of the motor with and without actuation.

Levitation in fluid based systems can be achieved due to pressure built-up as a result of periodic forcing of the fluid. In our ultrasonic micromotor, as the vibration speed of the stator is higher than the substrate, the acoustic streaming speeds in the rotor – stator gap are higher than the air speed in the rotor – substrate gap. The diameter of rotor is significantly larger than the rotor-stator air gap and rotor-substrate air gap and the air in both the gaps can be assumed to be trapped. Since the air velocities in the rotor-stator gap are high compared to rotor-substrate gap, the pressure immediately above the rotor is lower than the pressure immediately below the rotor

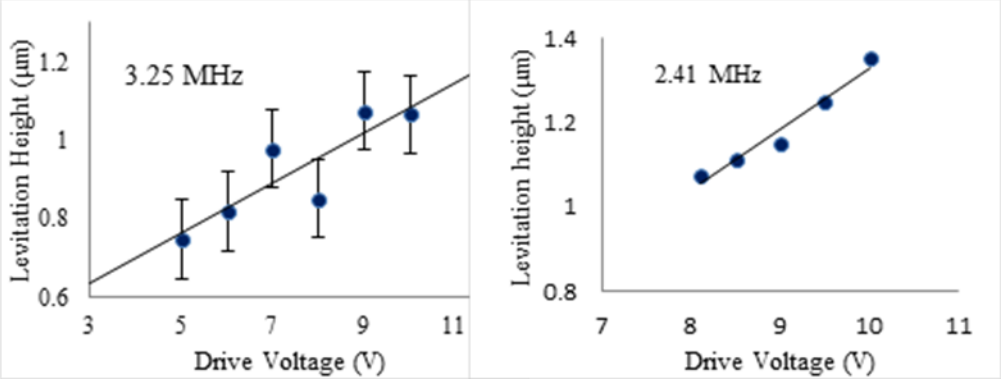

Figure 3.14 Levitation height during rotation (measured with ZYGO) with drive voltage at (a) 3.25 MHz, (b) 2.41 MHz.

thus lifting the rotor. The levitation of our ultrasonic motor-rotor is calculated from the difference between the out of plane deformation profile of the motor with and without rotation of rotor. The levitation of the rotor is observed only at high drive frequencies (>2 MHz). The levitation height is measured at different PZT drive voltages and found to linearly increase with voltage as shown in Figure 3.13Figure 3.14, Figure 3.15

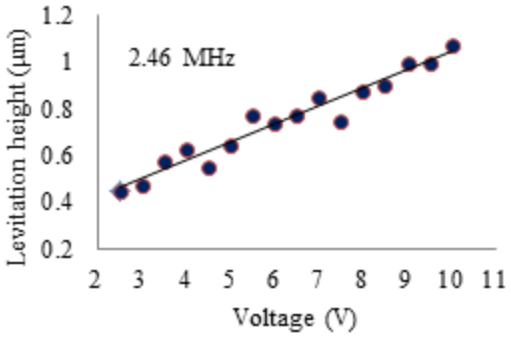

Figure 3.15 Levitation height measured during rotation of motor with drive voltage at 2.46 MHz

3.5 Conclusions

We have presented an ultrasonic micromotor that is actuated using PZT piezoelectric plate, and the effect of controlling the stator curvature on the rotor motion. The motor-stator bilayer buckles due to residual stresses and the resulting wavy pattern results in improved and reliable performance of the motor. While buckling phenomena is commonly considered as a problem in most of the structures, there are applications where circular plates are selectively buckled to use them as oscillators. The buckling phenomenon observed in our stator is one way to realize thin flat plates selectively deflected out of plane to a few micrometers. The curvature of the rotor changes with temperature and the effect of this variation on the rotation rate is also shown. The nonlinear effects causing the rotor action are measured in real time, to help identify the mechanisms of rotor stability. During rotation of the motor, we demonstrate the levitation of the rotor with minimal contact to stator on the top or the substrate on the bottom. The levitation feature of the micromotor makes it a suitable rotation platform for the micro-devices that are sensitive to motional artifacts.

Chapter 4

NON-CONTACT ROTOR CONTROL USING THERMAL ACTUATORS

4.1 Introduction

Micro scale stable rotating platforms with integrated inertial sensors hold the promise of performing in-situ gyroscope and accelerometer sensor calibration by applying known accelerations and rotation rates. However, for accurate calibration of the inertial sensor, the rotation of the platform needs to be free of unwanted off-axis motion, and transient motions that can excite unwanted proof-mask resonant modes, and sensor structural modes. For example, a rotating platform needs to rotate smoothly without actuator artifacts such as sudden jerks. Since many such jerks can originate from contacts, a non-contact method of controlling the rotation platform and a non-contact method of measurement is desired. Non-contact actuation and sensing will ensure control of the rotation platform with as little physical contact as possible, increasing reliability, life time and eliminating interconnects and other artifacts that are common in solid-solid contact motors. In our work, we have demonstrated a non-contact method of controlling the ultrasonic motor motion by integrated thermal actuator driven gripper close to the rotor. Section 4.2 provides the design of the thermal actuator driven gripper and its ability to control motor operation. We also present the results of thermal actuator driven gripper aiding the motor rotation at low PZT drive voltages. In order to realize the non-contact method of measurement, preliminary results of optical diffraction patterns from integrated gratings on the rotor and substrate are presented in section 4.3.

4.2 Non-contact rotor control through thermal actuator driven gripper

A polysilicon thermal actuator can operate in the current and voltage regimes that are compatible with integrated circuit (IC) operation at less than 5 volts, and can be fabricated by a CMOS compatible surface micromachining technology. In the work here, we integrated a thermal actuator driven gripper close to the rotor to demonstrate a non-contact approach of controlling the ultrasonic motor motion as shown in Figure 4.1. The thermal actuator design is a commonly used structure consisting of hot and cold arms that are connected together at one end. As current flows through the two arms, the arm with the smaller cross-section has a higher electrical resistance and hence reaches higher temperature for a given current, compared to the arm with a larger cross-sectional area. As a result of the temperatures, the hotter arm expands more and leads to a bending of the structure much like a thermal bimorph. A gripper is connected to the tip of thermal actuator and this gripper is placed next to the rotor with an initial gap of 5 μm between the rotor and the gripper. During the rotation of the ultrasonic motor with the PZT drive at the base, the thermal actuator is simultaneously

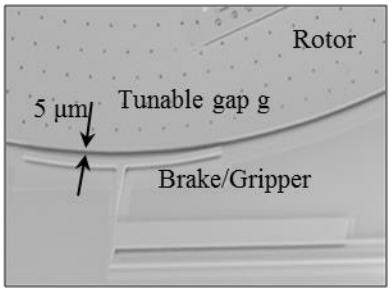

Figure 4.1 SEM of the thermal actuator that moves the gripper towards rotor.

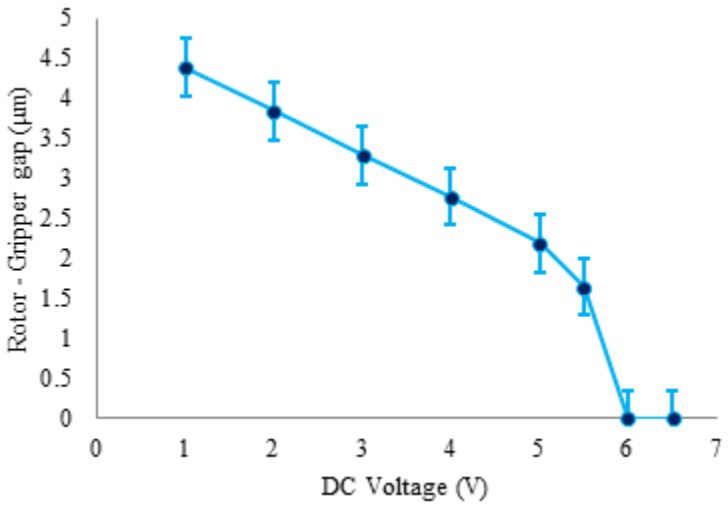

Figure 4.2 Rotor-Gripper Gap variation with voltage

actuated by applying DC voltage between its two electrodes. As the DC voltage to the thermal actuator increases, the gripper bends closer to the rotor. The rotor-gripper gap is measured using the ZYGO optical profilometer. The objectives used in the profilometer for recording of the measurements correspond to the horizontal resolution of 0.36 µm . The rotor- gripper gap gradually reduces with the increase in the DC voltage as shown in Figure 4.2. The gaps at various voltages showed in the plot are the average values measured through ZYGO optical profilometer and are slightly lower than the actual rotor-gripper gaps as the thermal actuator driven gripper is also vibrating at the PZT actuation frequency.

In the next sub-section, the theory of thermal actuation is presented with analytical expression for the deflection of thermal actuator driven gripper to compare with the experimental values shown in Figure 4.2**.** The infrared images of the temperature profile of motor Figure 4.3(a), (b)) with thermal actuator drive were

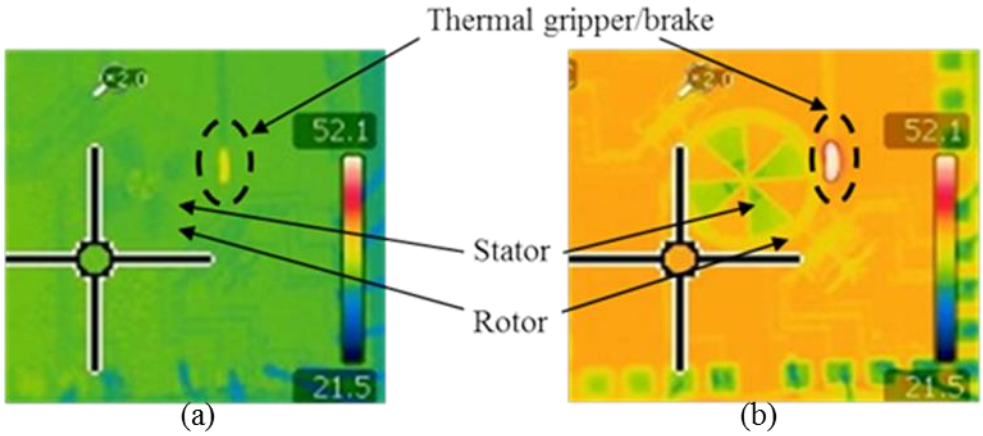

Figure 4.3 Infrared images of the motor captured at (a) 2V, (b) 6.5 V applied to thermal actuator shows heating of the substrate and the stator along with the thermal actuator driven gripper with increase in voltage. Color code units (a) and (b) are in degree Centigrade.

recorded to verify the models. The infrared images show that the substrate, stator, and rotor are also heated with the actuation of thermal actuator. The temperature of the rotor is at 7 – 10^{o}C lower than that of the substrate as it is levitating during rotation. The effect of heating can have many effects. It can increase the air viscosity for higher streaming force, or it can cause a DC buoyancy force on rotor for easier levitation, etc.

4.2.1 Analysis of thermal actuators

Consider the thermal actuator with gripper and the gripper cross-section as shown in Figure 4.4. As the thermal actuator is actuated by current flow, both the arms get heated by ohmic heating.

Let:

- i = h, c or f representing the hot arm, cold arm, and flexure respectively,

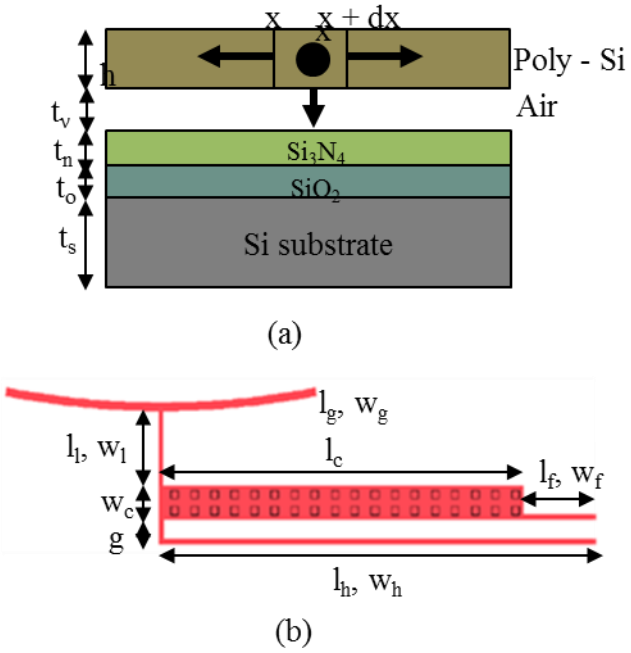

Figure 4.4 (a) cross-section diagram of the actuator for thermal analysis, (b) shows dimension labels of various beams.

- ρ_d is the density of polysilicon,
- C_p is the specific heat of polysilicon,
- K_p is the thermal conductivity of polysilicon,
- ρ_r is resistivity of polysilicon, $\rho_r = \rho_0 (1 + \xi(T - T_s))$, ρ_0 is the resistivity of polysilicon at room temperature, ξ is the temperature coefficient of resistance, T_s is the substrate temperature.
- T_i is the temperature of i^{th} arm at location x,
- V_i is the voltage across arm i,
- L_i is the length of arm i,
- S is the shape factor,

$$S = \frac{h}{w}\left(\frac{2t_v}{h} + 1\right) \tag{4.1}$$

h is thickness of polysilicon, t_v is the thickness of the air layer, w is width of the arm (cold, hot, or flexure). The shape factor for the hot arm, the cold arm and the flexure are calculated to be 2.4, 1.21 and 2.4 respectively.

Table 4.1 Parameters used in the analysis

Length	μm	Width	μm
l_h	240	w_h	2.5
l_c	200	w_c	16.5
l_f	40	w_f	2.5
l_g	170	w_g	4
l_l	38	w_l	2
g = 10 μm		h = 2 μm	
t_v = 0.75 um		t_n = 0.6 um	
t_o = 1 um		$\rho_0 = 22 \times 10^{-6}$ Ω m	
$\xi = 1.25 \times 10^{-3}\ K^{-1}$		$k_p = 50\ Wm^{-1}K^{-1}$	
Young's modulus of polysilicon, E = 158 Gpa			
Thermal expansion of polysilicon, $\alpha = 3 \times 10^{-6}\ K^{-1}$			
T_s = 298 K		$C_p = 860\ J\ kg^{-1}\ k^{-1}$	
$\rho_d = 2330\ kg\ m^{-3}$		Poisson's ratio ν = 0.22	
Thermal conductivity of air, $k_v = 0.026\ Wm^{-1}\ ^oC^{-1}$			
Thermal conductivity of Si_3N_4, $k_n = 2.25\ Wm^{-1}\ ^oC^{-1}$			
Thermal conductivity of SiO_2, $k_o = 1.4\ Wm^{-1}\ ^oC^{-1}$			

- R_T is thermal resistance, $R_T = \frac{t_\nu}{K_\nu} + \frac{t_n}{K_n} + \frac{t_o}{K_o}$. The thermal resistance is 29.82 x 10^{-6} W^{-1} m^2 K.

The rate of temperature change along the i^{th} arm is the combination of the longitudinal heat flow in the arm and the resistive heating power generated in an element minus the heat conduction out of the element according to [64][65][66]:

$$\rho_d C_p \frac{\partial T_i}{\partial t} = K_p \frac{\partial^2 T_i}{\partial x^2} + \frac{V_i^2}{\rho_r L_i^2} - \frac{S_i}{h}\left(\frac{T - T_s}{R_T}\right) \tag{4.2}$$

In order to find the time constants of hot, cold and flex arms, $\frac{\partial^2 T}{\partial x^2}$ term is neglected, and considering the first order system, the approximate time constant is $\tau_{approx_i} = \frac{h\rho_d C_p R_T}{S_i}$, i = *h, c* or *f*. Using this expression, the time constants are τ_h = 45.9 μs, τ_f = 45.9 μs, and τ_c = 114.7 μs. At steady state, the temperature distribution of hot arm, cold arm, and flexure can be solved to be [64].

$$T_h(x) = T_H + c_1 e^{m_h x} + c_2 e^{-m_h x} \tag{4.1}$$

$$T_c(x) = T_C + c_3 e^{m_c x} + c_4 e^{-m_c x} \tag{4.2}$$

$$T_f(x) = T_H + c_5 e^{m_h x} + c_6 e^{-m_h x} \tag{4.3}$$

where

$$T_i = T_s + \frac{J_i^2 \rho_0}{K_p m_i^2}, \tag{4.4}$$

$$m_i^2 = \frac{S_i}{K_p h R_T} - \frac{J_i^2 \rho_0 \xi}{K_p}, \tag{4.5}$$

i = H or C, J is the current density. Using (4.2), the maximum temperature of hot arm at V = 2V is 339 K and at V = 6.5 V is 786 K. The maximum temperature at V = 2V is close, but slightly higher compared to the temperature measured from the infrared

image in Figure 4.3(a). This is due to the reason that the heat loss due to the gripper (l_g, w_g, l_l, w_l) is not taken into consideration and the actual maximum temperature will be slightly lower as shown in the Figure 4.3(a). Since the infrared image is limited to lower temperatures, the color in the infrared image in Figure 4.3 (b) is saturated for V = 6.5V and the actual temperature is significantly higher close to theoretical calculation. The deflection of the free end of the actuator is

$$u = \frac{l_h^2}{6EI_h}(X_1 l_h - X_3) \quad (4.6)$$

where X_1 and X_3 are given in [64]. Using this expression, the deflection at 4 V is found to 3 μm which is close to the experimental value in Figure 4.2.

4.2.2 Rotation rate and direction control

Increasing the DC actuation voltage to thermal actuator, as the gripper comes closer to the rotor, and as the rotor-gripper gap reduces, the rotation rate of motor is increased as shown in Figure 4.6. The gradual increase of the rotor speed by the approaching gripper is counter-intuitive and was a surprising finding from this work. One would expect that speed should decrease due to a drag force between the gripper and the rotor. The increase in rpm indicates that there is an additional force on the rotor to force it to rotate at higher angular speeds due to the gripper proximity. A possible force is the acoustic streaming generated force between the gripper and the rotor. Any sonic motion of the rotor or the gripper would lead to motion of the air between them potentially causing acoustic streaming forces. The rotor, since it is suspended is likely to have very small ultrasonic motions, due to minimal coupling through the thin air layer. However, the gripper is anchored to the substrate, and is

driven by the inertial forces from the vibrating substrate. The thermal actuator anchored to the substrate vibrates at the PZT drive frequency, and many kinds of motion on the gripper are possible as a function of frequency. The ultrasonic wavelengths at the frequencies of 100 kHz to 10 MHz are from 90 mm to 0.9 mm given the speed of sound in silicon for pressure waves is 9000 m/s. These wavelengths are much larger than the structures on the substrate, inducing coupling through the inertial force. The modes excited on the gripper can be flexural and have lower wavelengths. In order to simplify the problem, we first assume that the motion is rectilinear – that is the gripper moves tangent to the rotor surface at ultrasonic frequencies. Any normal motion of the gripper could also be important, but would most likely to be damped out due to absorption in the air-cushion. The surviving tangential motion creates a gradient of velocity between gripper and rotor due to a shear viscous field. The shear viscous field gives rise to time averaged acoustic streaming force acting on both the gripper and the rotor.

The shear viscous field can be modeled by making assumptions on the rotor and gripper surface velocities. The rotor surface velocity is much smaller than the acoustic gripper velocities for the range of rotations speeds encountered in our experiments. Hence, the rotor velocity can be assumed to be zero, even though it is rotating for the acoustic analysis. The gradient, results in acoustic streaming force and a torque that can affect the motor rotation rate [62]. We present here the detailed theoretical analysis of increment in rotational speed of the motor and show that theoretical rotation rate matches well with experimental data shown in Figure 4.6.

Let us consider a two dimensional co-ordinate system (x, y) as shown in (Figure 4.5(a), (b)). Since the thermal actuator driven gripper is anchored to the substrate at one of its ends, the gripper vibrates at PZT drive frequency.

Let

- u, v, be x,y components of air velocity in the gap respectively
- ν is the kinematic viscosity of air
- ρ is the density of air
- F_x is acoustic streaming force per unit volume

Assume:

- Incompressible air flow in the rotor-gripper gap
- The gripper vibrates at ω and the air velocity in the gap is harmonic with frequency ω.

Governing equations:

- The general form of continuity equation is

$$\frac{\partial \rho}{\partial t} + \nabla \cdot (\rho v) = 0 \tag{4.7}$$

Since we are assuming incompressible flow with constant density, the equation reduces to $\nabla \cdot v = 0$. Hence, the continuity equation in two dimensional form is

$$\frac{\partial u}{\partial x} + \frac{\partial v}{\partial y} = 0 \tag{4.8}$$

- The general form of Navier stokes equation in x direction is

$$\rho\left(\frac{\partial u}{\partial t} + u\frac{\partial u}{\partial x} + v\frac{\partial u}{\partial y}\right) = -\frac{\partial p}{\partial x} + \mu\left(\frac{\partial^2 u}{\partial x^2} + \frac{\partial^2 u}{\partial y^2}\right) + \rho g_x \tag{4.9}$$

Neglecting the external body force (ρg_x), and assuming p is constant ($\frac{\partial p}{\partial x} = 0$). From

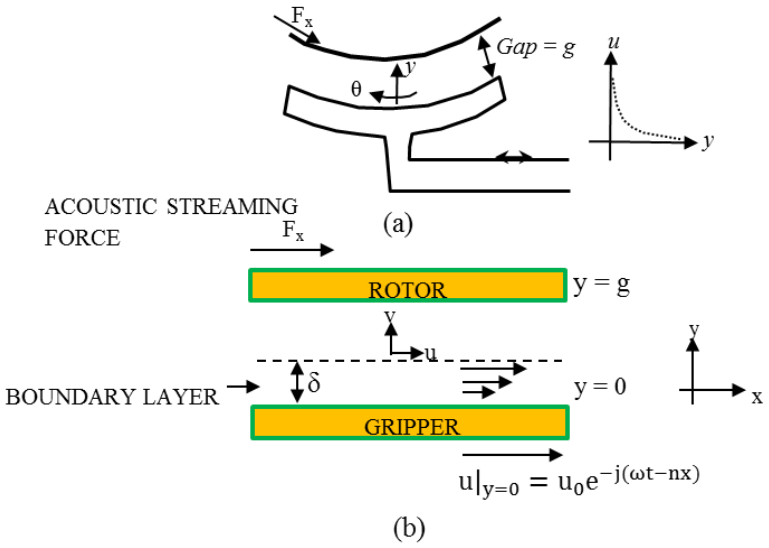

Figure 4.5 (a) Gripper moves due to substrate motion and creates a gradient in the sonic shear viscous field (uθ) giving rise to acoustic streaming force FAS, (b) Due to small rotor-gripper gap compared to the length of gripper, the rotor and the gripper can be represented in a two dimensional Cartesian coordinate system with vibration of the gripper at PZT drive frequency as the initial non-zero condition.

the order of magnitude analysis, $\frac{\partial^2 u}{\partial x^2} \ll \frac{\partial^2 u}{\partial y^2}$ since the x dimension in 2 orders of magnitude larger than y dimension. Hence $\frac{\partial^2 u}{\partial x^2}$ is neglected. $\frac{\partial u}{\partial t} \sim 10^6$, $u\frac{\partial u}{\partial x} \sim 10^{-1}$, $v\frac{\partial u}{\partial y} \sim 10^2$. Hence $u\frac{\partial u}{\partial x}, v\frac{\partial u}{\partial y}$ is neglected. Thus, the simplified Navier stokes equation in x direction reduces to

$$\frac{\partial \mathrm{u}}{\partial t} = \nu \frac{\partial^2 \mathrm{u}}{\partial y^2} \tag{4.10}$$

The general form of y- velocity v can be written as

$$u = \mathrm{Re}\left[F(y)e^{-j(\omega t - nx)}\right] \tag{4.11}$$

where F(y) is a function to be determined. Substituting this expression in the simplified Navier Stokes equation we get

$$F''(y) + \frac{j\omega}{\nu}F(y) = 0 \tag{4.12}$$

The corresponding characteristic equation is

$$k^2 + \frac{j\omega}{\nu} = 0 \tag{4.13}$$

From this, $k = \pm\frac{1-j}{\delta}$, $\delta = \sqrt{\frac{2\nu}{\omega}}$ = 1.24 x 10^{-6} at $\omega = 2\pi f$, f = 3.25 MHz (f = 3.25 MHz is one of the drive frequencies at which increment of rotation rate is recorded). Thus, the general form of F is

$$F(z) = Ae^{\frac{j-1}{\delta}y} + Be^{\frac{1-j}{\delta}y} \tag{4.14}$$

We input the boundary conditions - the zero rotor y-velocity and the gripper velocity, u0. Thus, at y = 0, F(y) = u_0, and at y=g, F(y) = 0. Substituting the boundary conditions in the general solution, the x-velocity, u is

$$u = u_0 e^{-\frac{y}{\delta}}\left[\frac{\cos\left(\frac{y}{\delta}-\omega t+nx\right)-e^{-\frac{2g}{\delta}}\cos\left(\frac{y-2g}{\delta}-\omega t+nx\right)}{-e^{-\frac{2(g-y)}{\delta}}\cos\left(\frac{2g-y}{\delta}-\omega t+nx\right)+e^{-\frac{2(2g-y)}{\delta}}\cos\left(\frac{y}{\delta}+\omega t-nx\right)}{1-2e^{-\frac{2g}{\delta}}\cos\left(\frac{2g}{\delta}\right)+e^{-\frac{4g}{\delta}}}\right] \tag{4.15}$$

We will find y-velocity v, by applying continuity condition in rotor-gripper air gap and integrate with respect to y,

$$v = -\int \frac{\partial u}{\partial x}dy + f(x) \tag{4.16}$$

Assuming f(x) = 0, acoustic streaming force per unit volume [67] is

$$F_x = \frac{\partial(\rho\overline{uu})}{\partial x} + \frac{\partial(\rho\overline{uv})}{\partial y} \tag{4.17}$$

Thus,

$$\overline{uu} = \frac{1}{2\pi}\int_0^{2\pi} u^2 dt \tag{4.18}$$

$$\overline{uv} = \frac{1}{2\pi}\int_0^{2\pi} uv\, dt \tag{4.19}$$

Since we are interested in acoustic streaming force per unit volume on the rotor, i.e., at z = g,

$$F_x = \frac{\partial(\rho\overline{uu})}{\partial x} + \frac{\partial(\rho\overline{uz})}{\partial z}|_{z=g} = \rho k_1(x, g) \tag{4.20}$$

The expression for $K_1(x,g)$ is calculated using Mathematica. Total acoustic streaming force, $F = \int_0^l \rho k_1(x, g)\, g \cdot t_r \cdot dx$, where l is the length of the gripper, g is the gap, t_r is the thickness of rotor/gripper and the corresponding total torque, T = Total force x rotor radius = FxR.

All the subsequent calculations done in Mathematica are presented in Appendix D. The effective rotation rate of the motor, ω in the presence of gripper is

$$\omega = \omega_0 + A*T, \tag{4.21}$$

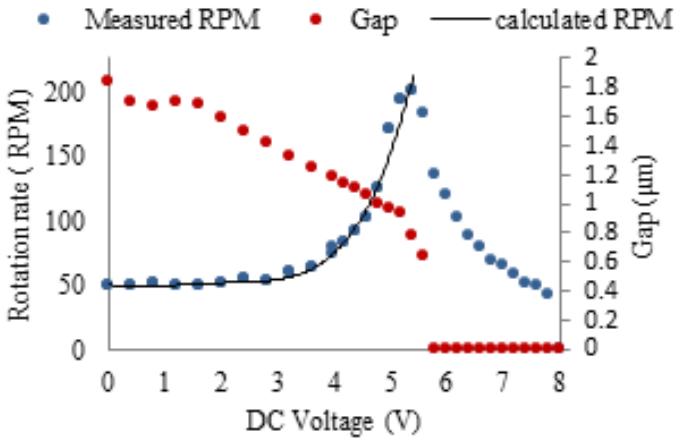

Figure 4.6 Rotation rate increases as the gripper gap decreases with increasing actuator voltage. As the gripper starts touching the rotor, the rotation rate decreases.

where ω_0 is the original rotational speed of the rotor without gripper, T is the torque and A is the fitting constant. The rotational rate derived from the above equation fits well with experimental result as can be seen in Figure 4.6. The fitting parameter to get the match is 1.21×10^{15}. The mass moment of inertia of the rotor is 4.08×10^{-16} kg-m^2. The fitting constant is proportional to mass moment of inertia. At about a DC voltage of 5.5 V, gripper-rotor gap become small enough for the gripper to periodically touch the rotor, resulting in periodic holding, rotation rate starts reducing until it completely touches the rotor and brakes the rotor motion. The reduction in rotation rate can be seen in Figure 4.6.

The acoustic streaming torque from the thermal actuator can add to or counteract the acoustic streaming torque from the stator drive. If the shear viscous force due to thermal actuator gripper is in CW (clockwise) direction, and if the rotor is rotating in CW direction due to stator force, the forces add constructively and we observed an

increase in rotation rate of the rotor as the rotor-gripper gap decreases (Figure 4.6). On the other hand, if the rotor is rotating in CCW (counter clockwise) direction, the rotation rate decreases as the rotor-gripper gap decreases eventually making the rotation rate zero and then reverses the direction of the rotation to CW (Figure 4.7). As the drive voltage for the PZT increases (Figure 4.7), the stator force and the gripper force both increase since PZT drive is the source of energy for both the actuators. Hence, as the PZT drive voltage increases, the transition from CW to CCW direction occurs at lower gaps. This could be due to better coupling of motion to the gripper, compared to the stator. The seeming variability of direction and amplitude near the transition point (Figure 4.7) could be due to the unsteady contact dynamics between

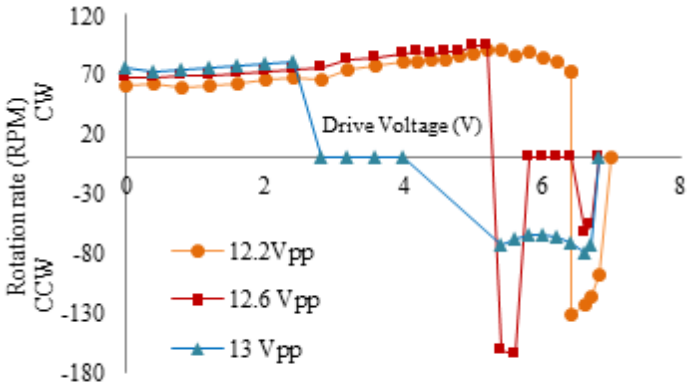

Figure 4.7 Rotation rate as a function of thermal actuator voltage shows that shear viscous force can change direction of rotation (CCW- to CW+). Threshold changes with drive voltage, with increased role of shear drive.

the rotor and the gripper. The gripper force is significantly high to drive the rotor in the opposite direction, indicating that the torques generated by the stator and the gripper are comparable.

4.2.3 Thermal actuator aided actuation of motors

In many cases, the stator excited by PZT at low voltages (5-7 Vpp) does create vibrations in the stator that do not have sufficient force to rotate the rotor. Aided by a set of thermal actuators, to apply forces in addition to those applied by the ultrasonic stator, the thermal actuators are able to enhance the ultrasonic motor reliability. We have observed that the thermal actuators cause smooth rotation of motor at 100 – 300 rpm with the PZT actuation voltages of 5.4 – 7.1 Vpp.

When the PZT is actuated in this voltage range, the thermal actuators that are located in diametrically opposite directions are actuated. The thermal actuator driven gripper gets closer to the rotor and the shear viscous field developed in the gap creates a significant force resulting in the rotor motion.

It is observed that in a rotation created with the aid of thermal actuators, there is a delay before the start of rotation. Also, as the thermal actuator is turned off, the rotor continued to rotate for some time before it stopped indicating the presence of thermal hysteresis. In the range of 5.4 – 6.1 Vpp, when the rotation starts, the motion of the rotor continues even after turning off the thermal actuator.

4.3 Optical interrogation

In order to realize applications in future with integrated motor control, rotation of the motor is measured using integrated gold diffraction gratings. The spacing of accelerometer grating (AG), movable grating G_1 and fixed grating G_2 shown in

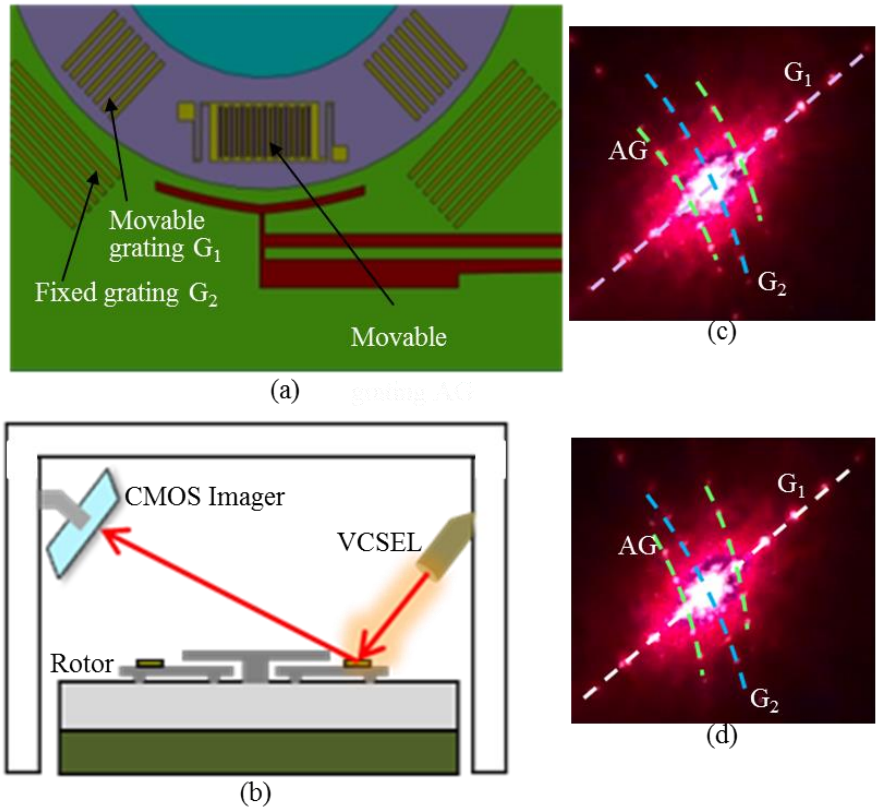

Figure 4.8 (a) Fixed and movable gratings , (b) and (c) shows diffraction grating pattern rotates with rotor motion, (d) showing ultrasonic motor, VCSEL, CMOS imager for optical readout of an accelerometer in a package of 10 x 2 x 3 cm. Figure 4: (a) Schematic set up shows a levitated rotor with integrated inertial sensor held by two grippers, and the diffraction pattern from the gratings of the inertial sensor and others is read by a CMOS imager when a VCSEL light is emitted on part of the motor. (b) Schematic of fixed gratings on the substrate G2, movable gratings on the rotor G1, and accelerometer gratings AG.

Figure 4.8 (a) is designed to record the diffraction pattern at a finite distance (2 cm to 1m) such that sufficient distance between the diffraction peaks is maintained for the

rotor theta location measurement. As shown in Figure 4.8(b), as the rotor is rotating, the light from 650 nm laser VCSEL diode (Thorlabs L650P007) is directed to cover part of the motor containing both movable grating (on rotor) and fixed grating (on substrate). The diffraction pattern from these gratings is recorded on a CMOS imager and digitally analyzed.

As described in Figure 4.8(b), there are moving and fixed gratings G_1, G_2, AG on the rotor and the substrate. These gratings are facilitated on the rotor, substrate to accurately measure the displacement of the accelerometer gratings AG. Accelerometer gratings AG move in tangential direction due to its spring motion. Here, we show the diffraction pattern recorded by CMOS imager, from G_1, G_2, and AG. While the diffraction pattern G_2 is fixed, the diffraction pattern from G_1 and AG move along the rotor (Figure 4.8(c), (d)). The fixed grating on the substrate, G_2 is the base (measurement). From the diffraction pattern reading of G_1 and G_2, the rotation rate of the rotor can be estimated. This rotation rate is found to match with the corresponding rotation rate in Figure 2.10. From the diffraction pattern reading of G_2 and AG, the displacement of the accelerometer gratings fingers can be estimated which is a subject of future work.

4.4 Conclusions

We have integrated a surface micromachined thermal actuator gripper next to an ultrasonic motor rotor. The actuator allows a sub-micron level gap to be formed between rotor and the actuator. With zero-gap between the rotor and the gripper, the gripper acts to hold the rotor in place. By adjusting the gap to sub-micron level, we can control the rotation rate and direction of the rotation of the motor. Acoustic streaming based model of torque generation due to relative motion between the

gripper and the rotor at ultrasonic frequencies is developed, which agrees with measured data. We have demonstrated the rotor motion at even lower threshold drive voltages, with the aid of a thermal actuator based gripper that can be placed at sub-micron gaps near the rotor. The temperature of the thermal actuator, motor shows the role of thermal actuator generated heat increasing the temperature of its surroundings. Both the temperature and deflection are in close agreement with the analytical expressions based on heat transfer in the thermal actuators. The role of the increased temperature near the rotor can lead to a host of physical phenomenon aiding the motor operation. These include buoyancy from heated air, increased air viscosity leading to higher acoustic streaming forces, and secondary convective air flow near the rotor, which can be investigated by varying actuator and ultrasonic drive voltages and frequencies.

Chapter 5

INERTIAL SENSOR CALIBRATION ON ROTOR

5.1 Outline

In this chapter, we introduce the concept of inertial sensor calibration on demand with attachment of the inertial sensor on the rotation platform. The calibration is to be done by optical means. To demonstrate the concept, we fabricated a gyroscope that can be sensed optically. The details of gyroscope fabrication are presented in section 5.2. We show a method of attaching a separate chip to a released ultrasonic motor in section 5.3.

MEMS inertial sensors have revolutionized the motion sensing. In today's market, MEMS sensors are used in navigation, consumer electronics, automobile industry, building & structural monitoring, medical applications, image stabilization and in

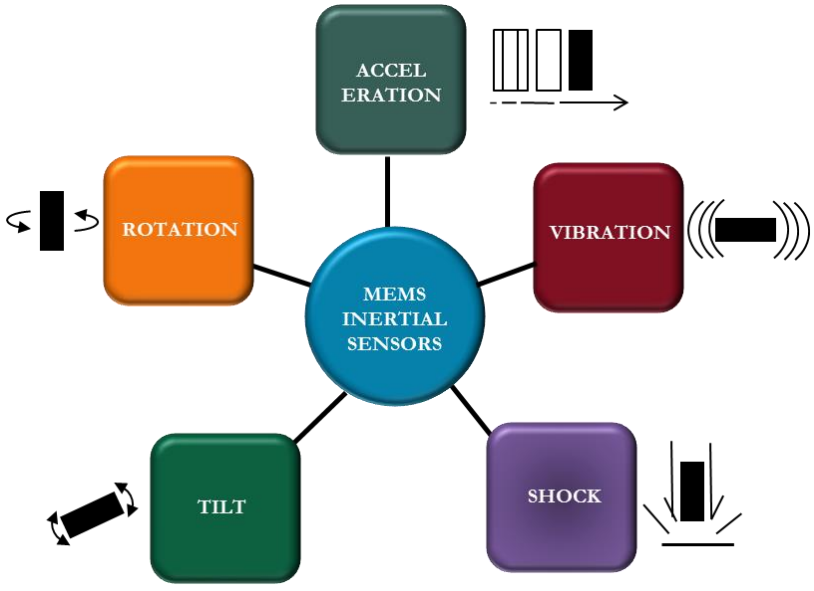

Figure 5.1 Schematic showing the key components measured with MEMS inertial sensors

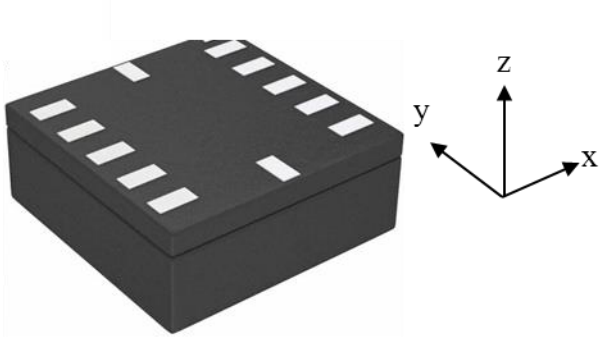

Figure 5.2 Three-axis accelerometer

many other fronts. Figure 5.1 shows the key components typically measured with MEMS inertial sensors. The main problem with the inertial sensors is non-zero bias and variability of scale factor, non-orthogonality factor. In addition, the factors vary with temperature, from device to device and time to time.

For example, consider a three axis accelerometer as shown in Figure 5.2. If the

true accelerations as in the matrix $\underline{A}_{a1}$ are applied to the accelerometer, the response voltages as in matrix $\underline{Y}_{a1}$ are measured. The accelerations applied and measured voltage responses are connected by a matrix $\underline{X}$ according to

$$\underline{Y}_{a1} = \underline{X}\,\underline{A}_{a1} \tag{5.1}$$

$$\begin{bmatrix} Y_{ax} \\ Y_{ay} \\ Y_{az} \end{bmatrix} = \begin{bmatrix} m_{axx} & m_{axy} & m_{axz} & b_{ax} \\ m_{ayx} & m_{ayy} & m_{ayz} & b_{ay} \\ m_{azx} & m_{azy} & m_{azz} & b_{az} \end{bmatrix} \begin{bmatrix} a_x \\ a_y \\ a_z \\ 1 \end{bmatrix} \tag{5.2}$$

where $\underline{Y}_{a1} = \begin{bmatrix} Y_{ax} \\ Y_{ay} \\ Y_{az} \end{bmatrix}$ are measured voltages, $\underline{A}_{a1} = \begin{bmatrix} a_x \\ a_y \\ a_z \\ 1 \end{bmatrix}$ are true accelerations applied,

$X = \begin{bmatrix} m_{axx} & m_{axy} & m_{axz} & b_{ax} \\ m_{ayx} & m_{ayy} & m_{ayz} & b_{ay} \\ m_{azx} & m_{azy} & m_{azz} & b_{az} \end{bmatrix}$. The first 3 x 3 elements of matrix X are scale factor values, and the last column has bias values. The ideal scale factor values should be invariant and bias values should be zero. It is hard to realize the ideal values in reality.

In order to calibrate this accelerometer, in general, in laboratory/manufacturing facility, a six position static test is performed with the accelerometer oriented in three directions as shown in Figure 5.3 and three other opposite directions. The orientation of the accelerometer in the six directions corresponds to application of six different known accelerations as given in matrix A in equation (**5.3**). This method is also called indexing or maytagging. A least square solution method is used for calibrating desired

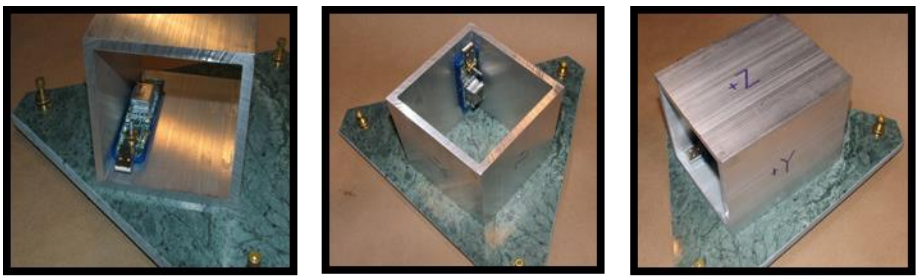

Figure 5.3 Orientation of accelerometers in six different directions (three opposite directions not shown here) to do accelerometer calibration according to six position static test [68].

$$A = \begin{pmatrix} g & -g & 0 & 0 & 0 & 0 \\ 0 & 0 & g & -g & 0 & 0 \\ 0 & 0 & 0 & 0 & g & -g \\ 1 & 1 & 1 & 1 & 1 & 1 \end{pmatrix} \tag{5.3}$$

$$A = [\underline{A}_{a1} \quad \underline{A}_{a2} \quad \underline{A}_{a3} \quad \underline{A}_{a4} \quad \underline{A}_{a5} \quad \underline{A}_{a6}] \tag{5.4}$$

$$Y = [\underline{Y}_{a1} \quad \underline{Y}_{a2} \quad \underline{Y}_{a3} \quad \underline{Y}_{a4} \quad \underline{Y}_{a5} \quad \underline{Y}_{a6}] \tag{5.5}$$

$$\underline{X} = \left(\underline{A}\,\underline{A}^T\right)^{-1} \underline{A}^T\,\underline{Y} \tag{5.6}$$

error parameters, the matrix X in equation (**5.6**) containing the bias and scale factor values.

Even after calibration on this huge calibration in the manufacturing facility, the inertial sensor bias and scale factors change after packaging and with environment, as a function of time due to aging and temperature fluctuations. There are many ways researchers are trying to reduce the bias and reduce the variability in the scale factor. Some of them are aiming to make better sensors, and an alternative way is to have the calibration platform with the sensor in the package itself to do on-demand calibration.

One of the methods to estimate the bias is carouseling. In carouseling, the sensor is placed on a platform and the platform is continuously rotated at a rate substantially faster than time scale of bias variation. For example, the orientation of the gyro input axis is rotated continuously. Due to this, the angle between earth's rotation axis and the gyro input axis changes resulting in the sinusoidal variation of the gyro output [69]. The bias and scale factor are estimated in real time by conducting a sinusoidal fit and this dynamic method greatly improves the inertial sensors. There is matter of

keeping track of direction and error in knowledge of direction introduces an error in the measurement.

A similar method was tried in SANDIA labs wherein they have an inertial sensor on a rotor consisting of mechanically contacting electrical interconnects [70] as shown in Figure 5.4. The serpentine springs connected to the stage expand as the stage rotates. This may load the motor and add additional biases. The motor is touching the substrate and the direct mechanical contact causes motion artifacts. We need a solution in which the rotor operates without contact and also a non-contact method of measurements should be taken. We want to adopt the carouseling method in which the rotor operates without contact and also implement a non-contact method of measurement. Our ultrasonic micromotor has the advantage of levitating as it rotates thus minimizing motional artifacts. The non-contact method we want to adopt for measurements is by optical diffraction means which gives enhanced accuracy. So, first we wanted to test an inertial sensor which can be sensed optically, then place this inertial sensor on the ultrasonic micromotor to adopt the dynamic method of estimating bias and scale factor. In our work, we have picked the inertial sensor

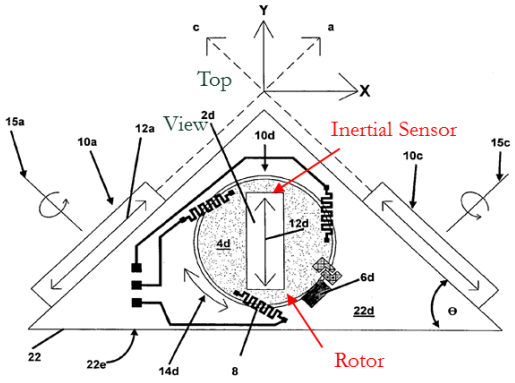

Figure 5.4 Carouseling method of reducing bias by SANDIA national labs.

gyroscope and aimed at demonstrating a way to transfer the gyroscope onto the micromotor and implement non-contact method of performing calibration measurement by optical diffraction means.

5.2 Gyroscope design and fabrication

Gyroscopes are currently used in numerous applications in the market and it was predicted that by 2015, gyroscopes market will be of $2 Billion value. Some of the applications of gyroscope in current market are shown in Figure 5.5. To test the concept of sensing gyroscope by optical diffraction means, we have picked the gyroscope design showed in Figure 5.6. This gyroscope can be actuated by electrostatic or piezoelectric means and sensed optically. It consists of two masses m_A and m_B that are driven in opposite direction in the x direction. The whole gyroscope is rotated in y direction at constant angular velocity Ω_y. The resultant of these two movements gives rise to Coriolis force on m_A and m_B in z direction opposite to each other. The center of gyroscope consists of grating fingers that alternately belong to mass m_A and m_B. The central fingers alternately move in and out of the plane. The dimensions of the gyroscope and the spacing between the central fingers are chosen so that a path difference corresponding to the net movement of the fingers in and out of the plane results in diffraction patterns. The net movement of the fingers through the difference can be detected by the diffraction patterns captured on a CMOS imager. The gyroscope has a hole to enable passage of light through the fingers from the backside of the device facilitating sensing by both transmittive diffraction and reflective diffraction as explained in Figure 5.7. The detailed fabrication process flow of the gyroscope is shown in Figure 5.8. The fabrication process was done using two masks. Starting with a SOI wafer with device layer thickness of 25 µm, mosilicide is

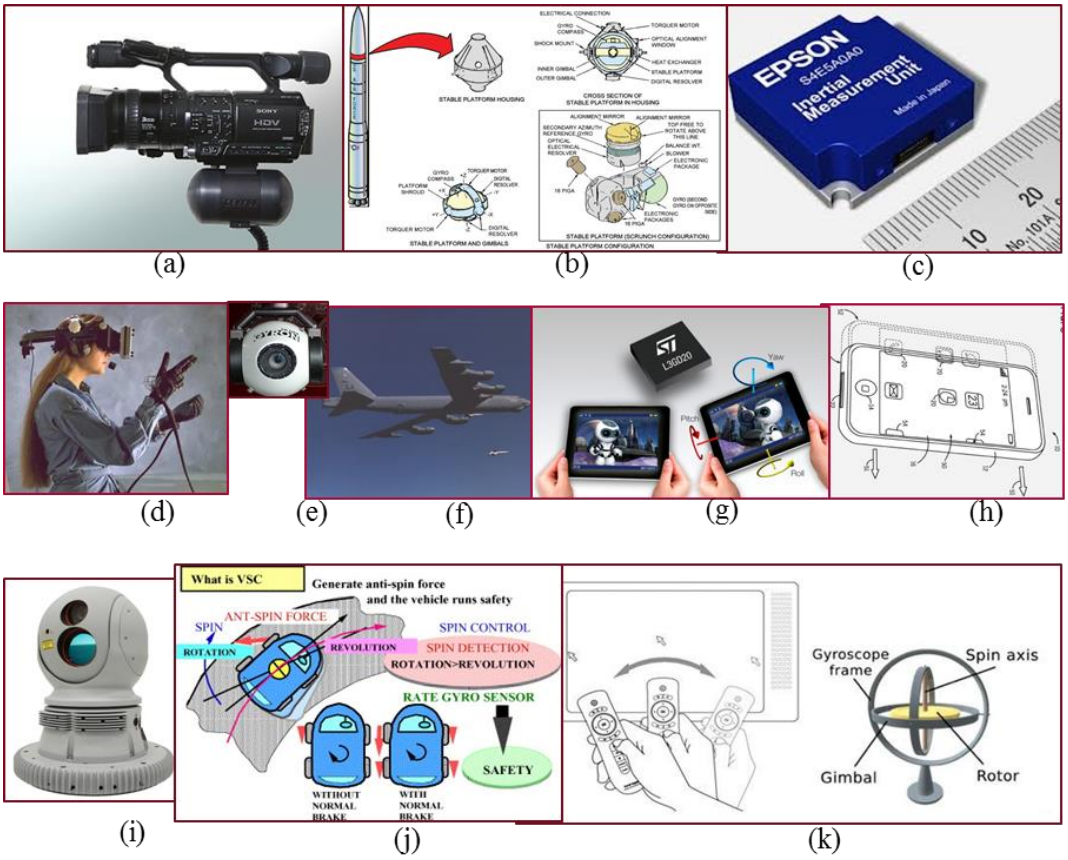

Figure 5.5 Several applications of gyroscope that are in current use – (a), (b) Gyroscope Stabilized platform, (c) Inertial Measurement Unit, (d) Head mount display, (e) Ball joint, (f) Midcourse navigation, (g) Rotation sensing, (h) Motion compensation, (i) FLIR, (j) Vehicle stability control, (k) Motion sensing game controller.

coated on the top for the metal contact and GSI oxide on backside of the wafer. Then after, front side lithography process is done, following by etching of the front side device layer using RIE method. Lithography process is repeated on the backside of the wafer and GSI oxide is etched first using RIE method which would become an etch mask for backside silicon etching. The backside silicon is etched using DRIE process

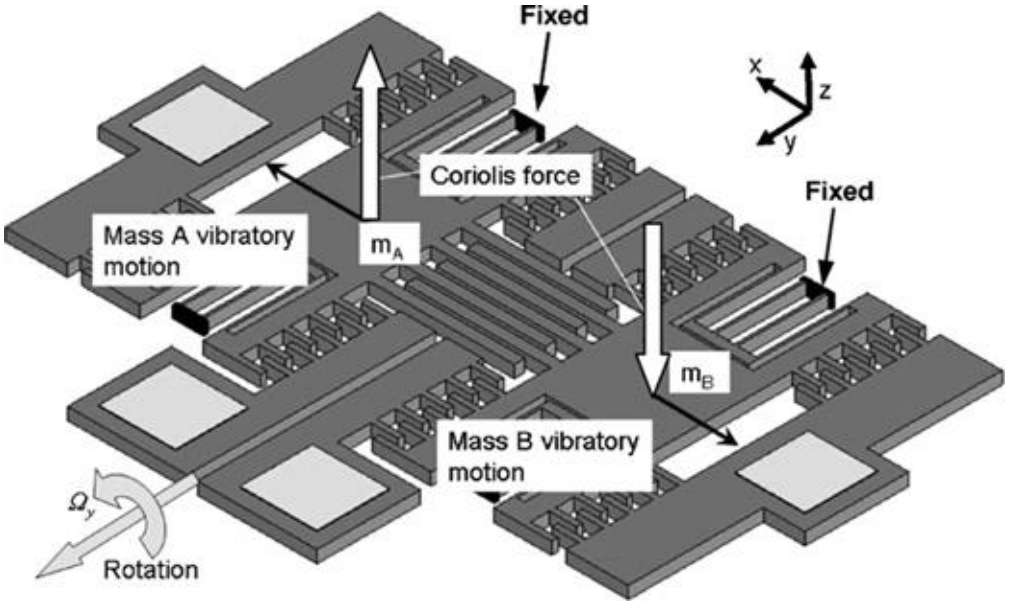

Figure 5.6 Design of the gyroscope shows masses mA and mB, driven in opposite directions and the Coriolis force in z direction due to rotation of gyroscope in y axis [71].

path and finally the wafers are released using BOE etch. The SEM of the released devices is shown in Figure 5.9. For testing the gyroscope, it is bonded to two surf board and wire bonding is done as shown in Figure 5.10. The testing of the gyroscopes is ongoing at the time of writing this thesis.

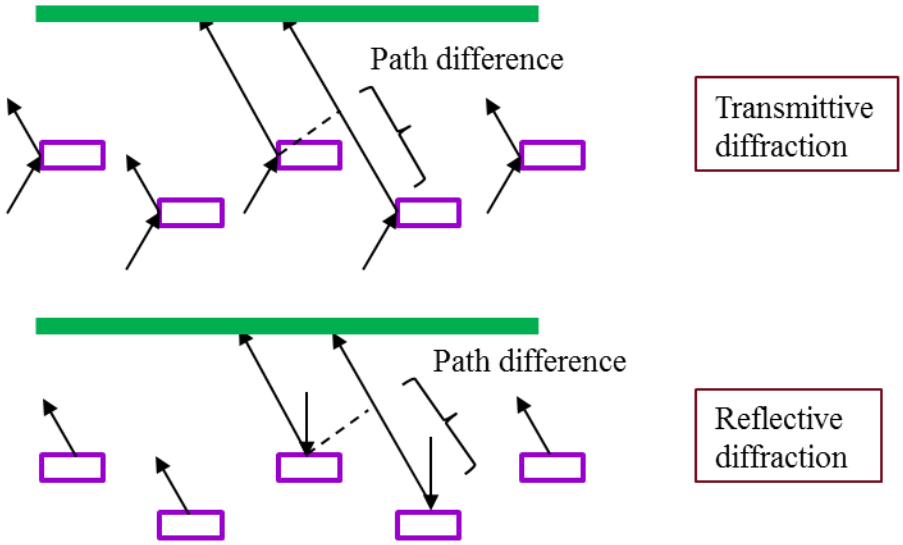

Figure 5.7 Gyroscope design shown in Figure 5.6 can be sensed through transmittive diffraction or reflective diffraction.

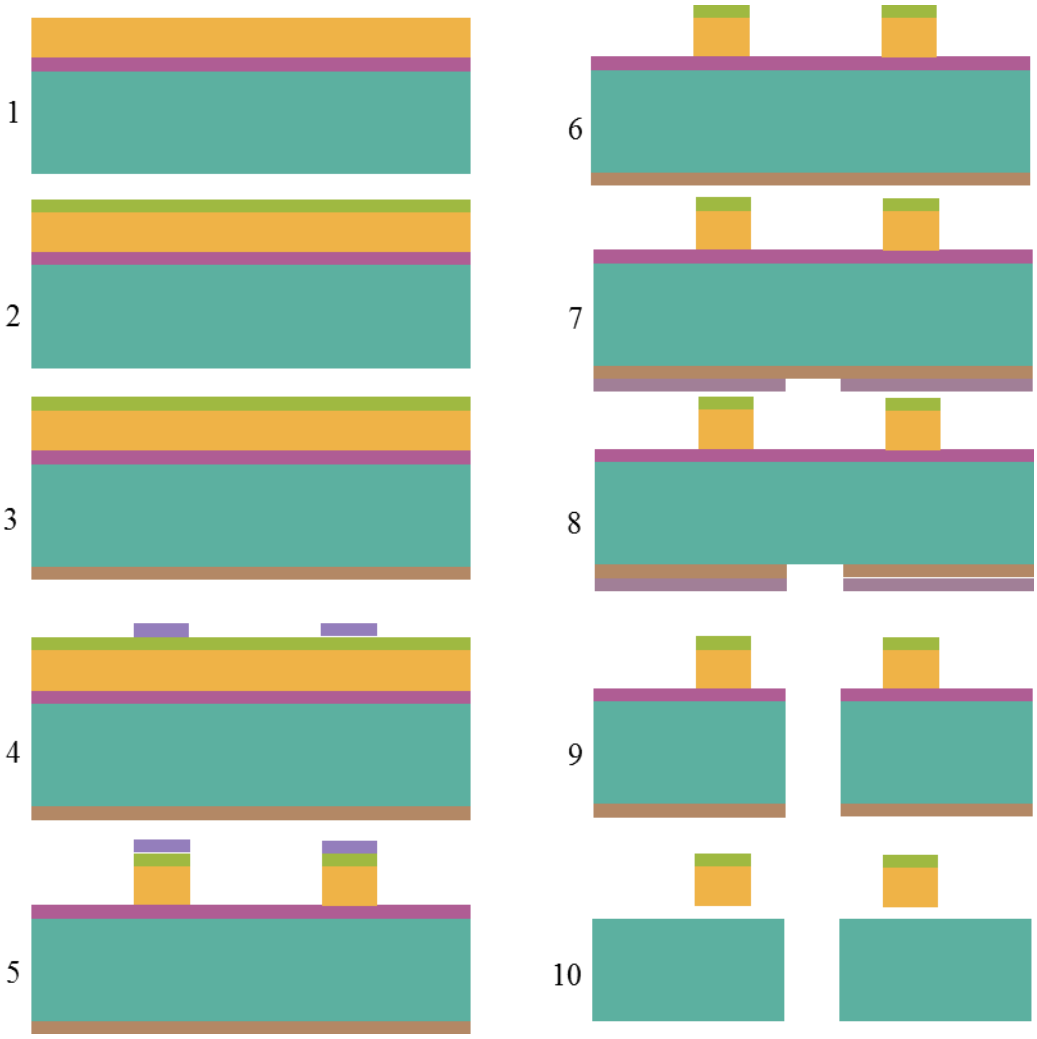
1
2
3
4
5
6
7
8
9
10

Figure 5.8 Process flow for the fabrication of gyroscope using a 2 mask process – 1) SOI wafer with 25 µm of device layer, 2 µm of buried oxide, 375 µm of backside oxide, 2) 100 nm of MoSi2 is sputtered on device layer, 3) 2 µm of GSI oxide deposited on backside, 4) Negative photoresist nLOF 2020 is spun on front side and is patterned, 5) Front side oxide etched using DRIE process after etching of 100 nm of MoSi2 using Oxford 100, 6) Removal of front side photoresist, 7) Positive photoresist SPR 3.0 coated on backside and patterned, 8) Backside oxide etched using Oxford 100, 9) Using oxide as the mask, backside silicon is etched using DRIE process, 10) The device is released in BOE.

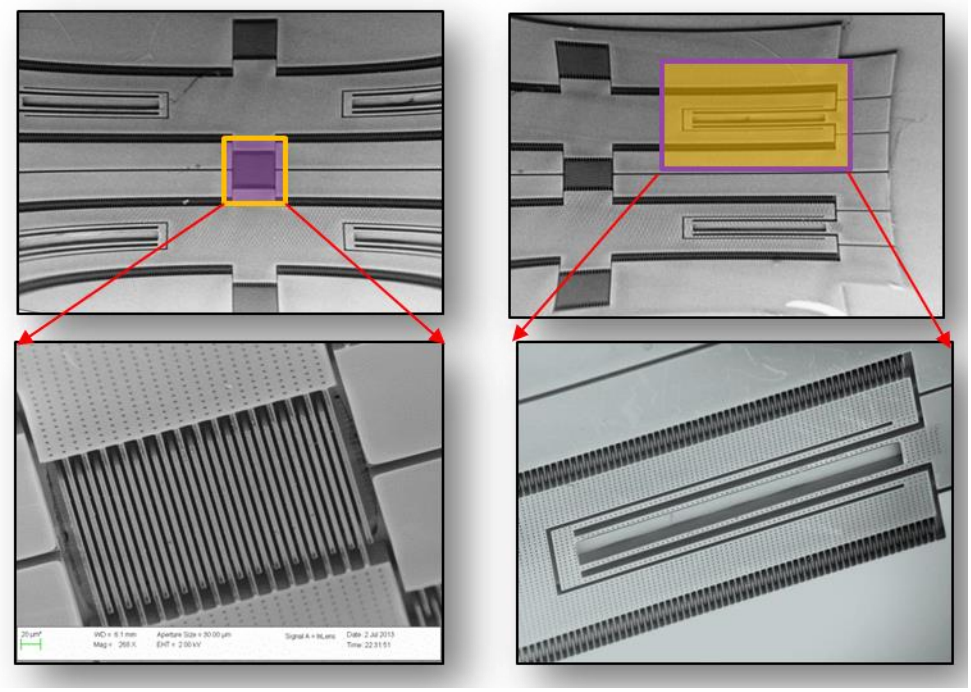

Figure 5.9 SEM images of fabricated gyroscope, inset showing actuation and sensing comb fingers.

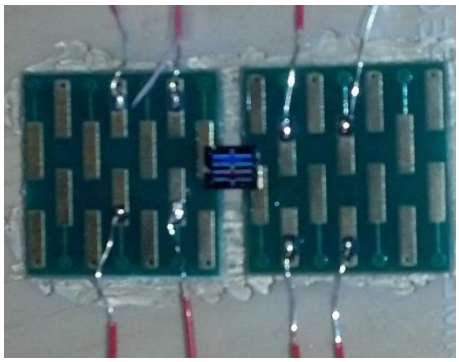

Figure 5.10 Gyroscope device bonded to surf board for testing

5.3 Beam bonding on motor using focused ion beam nanomachining

In this section, we present, for the first time, transfer bonding of external microstructures onto the ultrasonic micromotor through focused ion beam milling and deposition based nano attachment. Attaching optimized designs of inertial sensors will require bonding onto the rotor. Bonding before release process would lead to HF etching complications of the attached sensor. Bonding after HF release makes rotor structures too weak for thermo-compression bonding or flip chip bonding where high pressures are involved. As an alternative, we demonstrate focused ion beam based nano-machining to bond external structures onto the rotor.

As can be seen in Chapter 2, the stator is curved up due to the built-in stress between gold and polysilicon layer of the stator. From the surface profile of this stator in Figure 5.12 the maximum height of the stator is 4.5 µm. The gap between the stator and rotor is 2 µm. A pedestal of height greater than 6.5 µm needs to be bonded to the rotor so that an inertial sensor placed on top of the pedestal will not interfere with the stator.

Using focused ion beam, a silicon pedestal from external SOI beam structure is

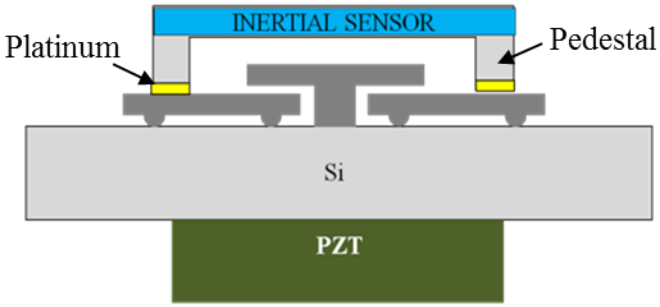

Figure 5.11 Side-view of the inertial sensor bonded to the rotor

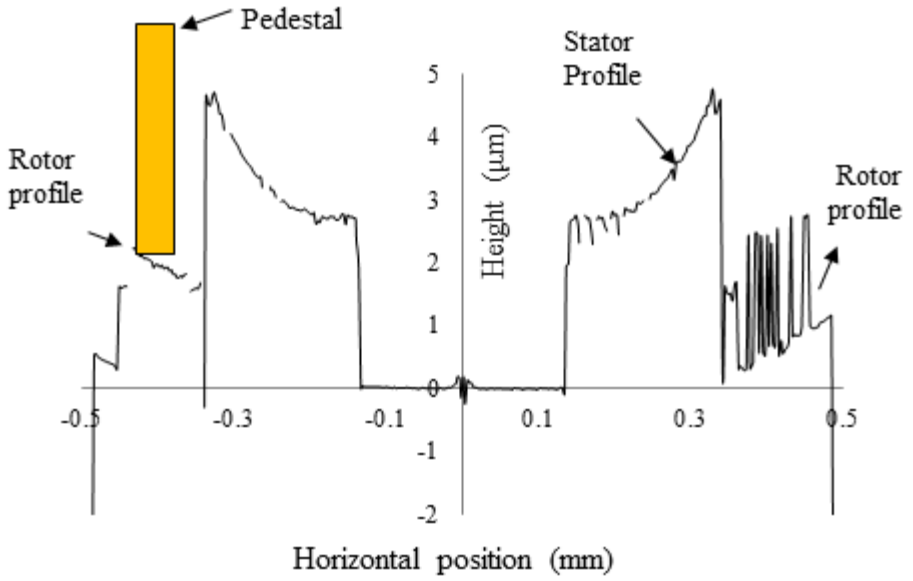

Figure 5.12 Surface profile height of the motor showing the maximum stator height is at 4.5 µm and the pedestal has to be higher than the stator height.

cut and placed onto the rotor using the process flow as shown in Figure 5.13(b). The process consists of ion milling for cutting and platinum deposition for bonding. After cutting the pedestal from external structure, it is bonded to the probe with platinum deposition and then separated from external structure and placed on top of the rotor. The edges of the pedestal are bonded to the rotor with a platinum deposition and the probe tip is separated with ion milling process. A beam current of 0.93 nA is applied during ion milling and 97 pA is applied during Platinum deposition. A Si beam of size 75 µm x 15 µm x 3 µm is bonded to the edge of the rotor Figure 5.14 (a). The motor showed rotation in this asymmetric configuration where the beam is only on one side of the rotor. Next, four beams of equal size 15 µm x 20 µm x 3 µm are placed symmetrically on the rotor as shown in Figure 5.14 (c) (d). The threshold

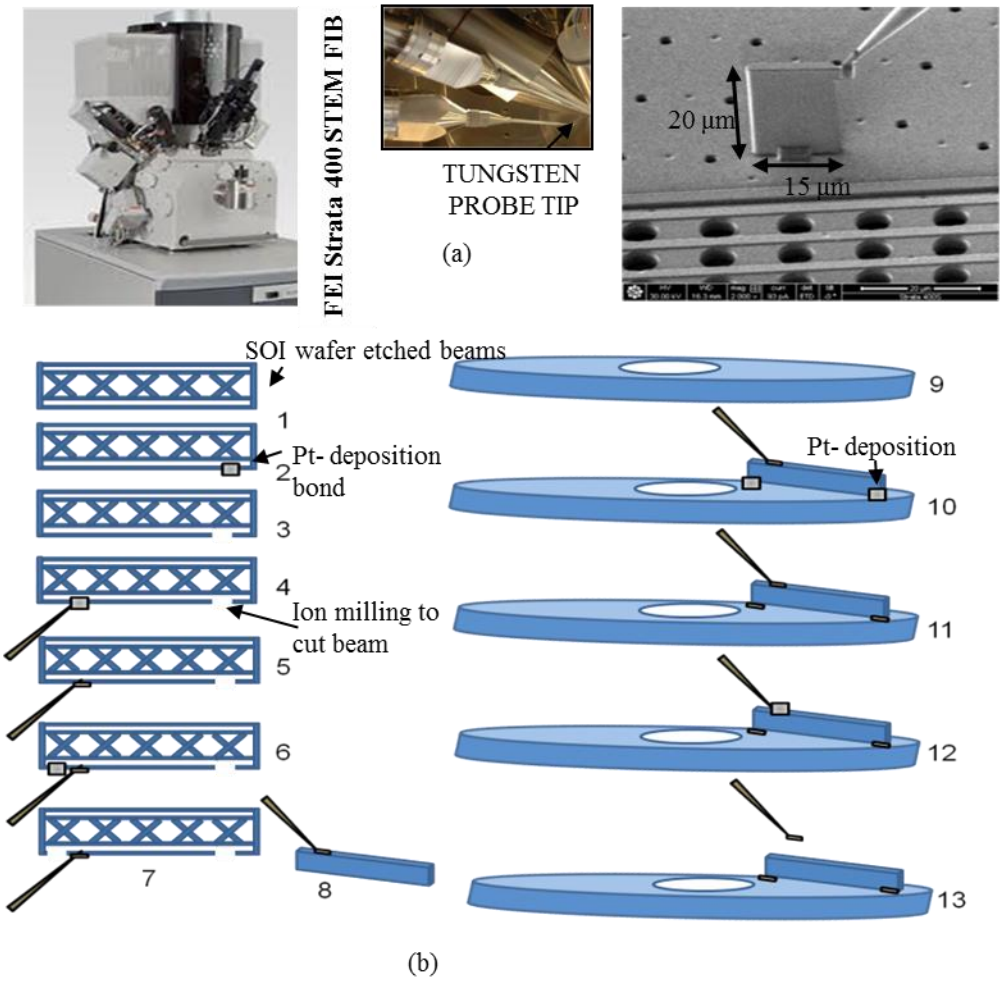

Figure 5.13 (a) Left: Focused Ion Beam tool, inset showing the tungsten probes, Right: tungsten probe tip bonded to the beam with Platinum deposition, (b) Process flow of cutting beam from external structure using ion milling and bonding it onto rotor using Platinum deposition step.

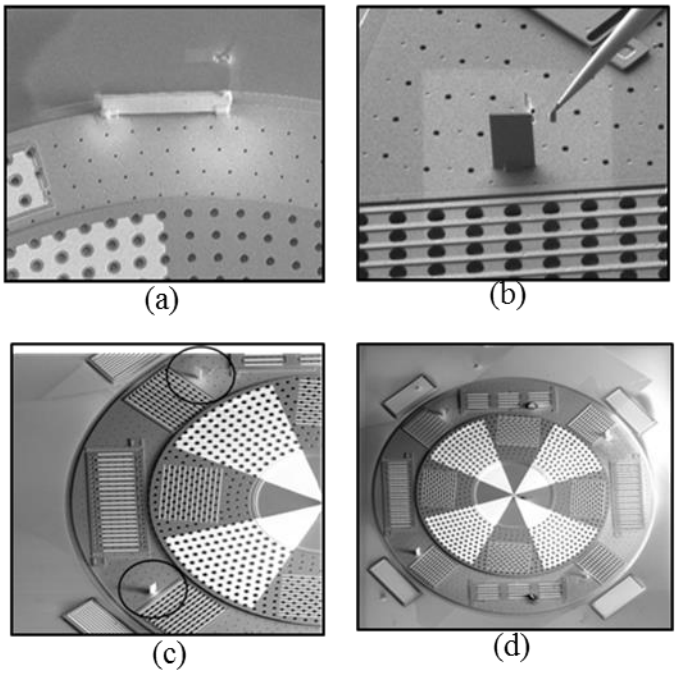

Figure 5.14 External structures bonded onto the micromotor rotor through Focused Ion Beam method, (a) beam of size 75 µm x 15 µm x 3 µm, (b) probe tip separation after bonding beam of size 15 µm x 20 µm x 3 µm, (c), (d) shows view of the motor with two and four beams.

voltage at which the rotation of the motor began has gone up from 7 Vpp (without beams) to 8 Vpp. An increase of weight on the rotor increased the force to overcome the initial friction and increased the threshold voltage. At 10Vpp actuation voltage, the rotation rate (without beams) is 125 RPM and with beams is 111 RPM. As part of future work, all optical gyroscope should be transferred onto the rotor through the pedestals.

APPENDIX

A. Ultrasonic Motor – Dimensions

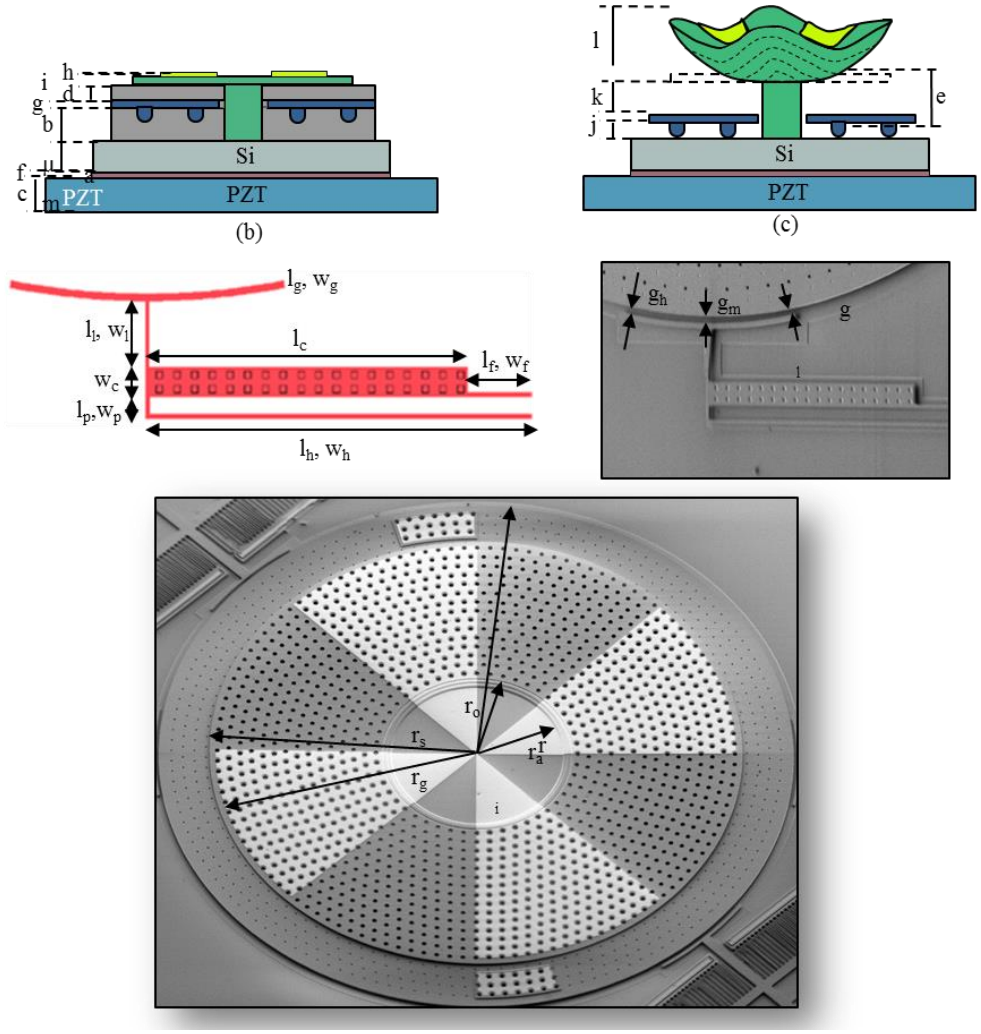

Figure A.1 Ultrasonic Micromotor and thermal actuator gripper dimensions

Dimension	Description	Value (µm)
a	Si substrate thickness	675 +/- 15
b	First sacrificial oxide layer thickness	2
c	PZT plate thickness	500
d	Second sacrificial oxide layer thickness	0.75
e	Anchor height	4.75
f	Adhesive layer thickness	25 – 40
g	Rotor /Poly 1 thickness	2
h	Gold layer thickness	0.5
i	Stator/Poly 2 thickness	1.5
j	Dimple thickness	0.75
k	Gap between stator and rotor after release	2
l	Maximum out of stator deflection recorded	14
g_l	Rotor-gripper gap at nearer end	4
g_h	Rotor-gripper gap at farther end	5.8
g_m	Rotor-gripper gap at the center	5
l_g	Approximate linear length of gripper	170
w_g	Width of gripper	4
l_l	Length of arm connecting gripper to thermal actuator	38
w_l	Width of arm connecting gripper to thermal actuator	2
l_c	Length of cold arm	200

Dimension	Description	Value (μm)
w_c	Width of hold arm	16.5
l_f	Length of flexure arm	40
w_f	Width of flexure arm	2.5
l_h	Length of hot arm	240
w_h	Width of hot arm	2.5
l_p	Length of arm connecting hot to cold arm	10
w_p	Width of arm connecting hot to cold arm	2
r_a	Radius of anchor	145
r_i	Inner radius of rotor	148
r_o	Outer radius of rotor	487
r_{ra}	Gap between rotor and anchor	3
r_{sa}	Radius of anchor (poly2)	135
r_s	Radius of stator	410
r_g	Radius of gold sector	400
r_{gs}	Gap between edge of gold and stator	10
	Ratio of stator inner radius to outer radius	0.33
	Poly-Poly2 Via anchor radius	140
	Hole 1 radius	1.5
	Hole 2 radius	3.5
	Hole metal radius	5.5
	Dimple radius	1.5

B. PZT – Motor Assembly

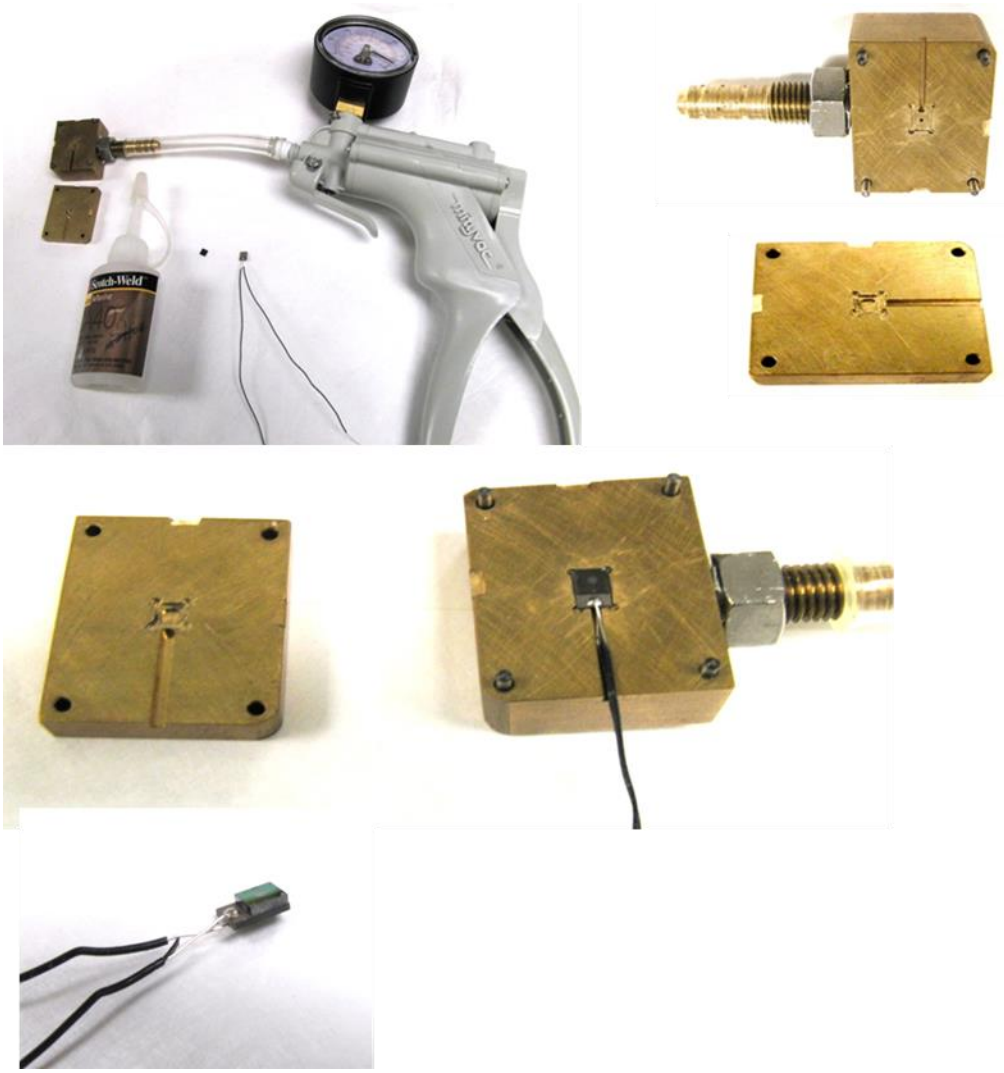

Figure A.2 Assembly process of micromotor to PZTusing Brass Zig and vacuum pump.

C. Thermomechanical FEM model of thermal gripper

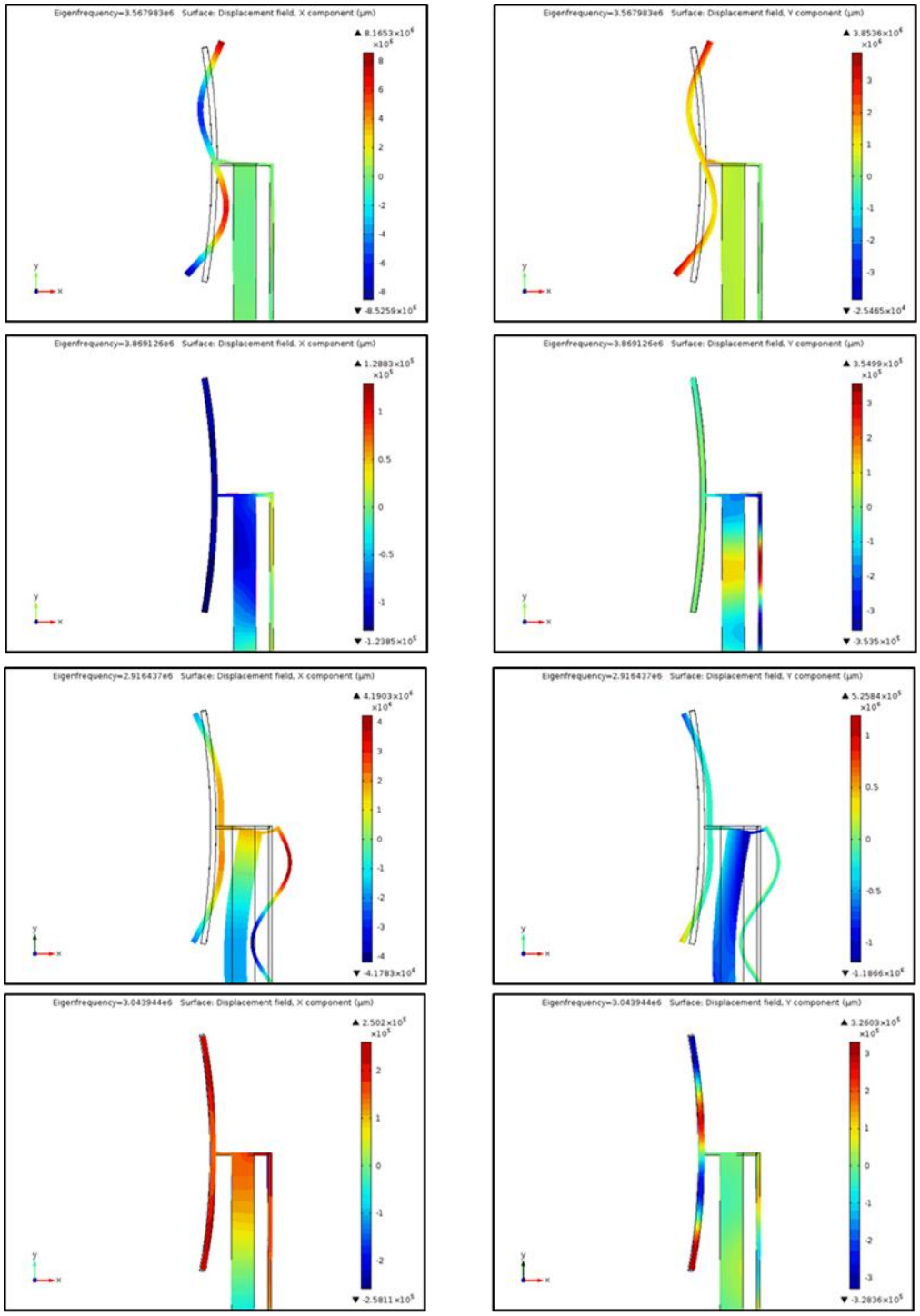

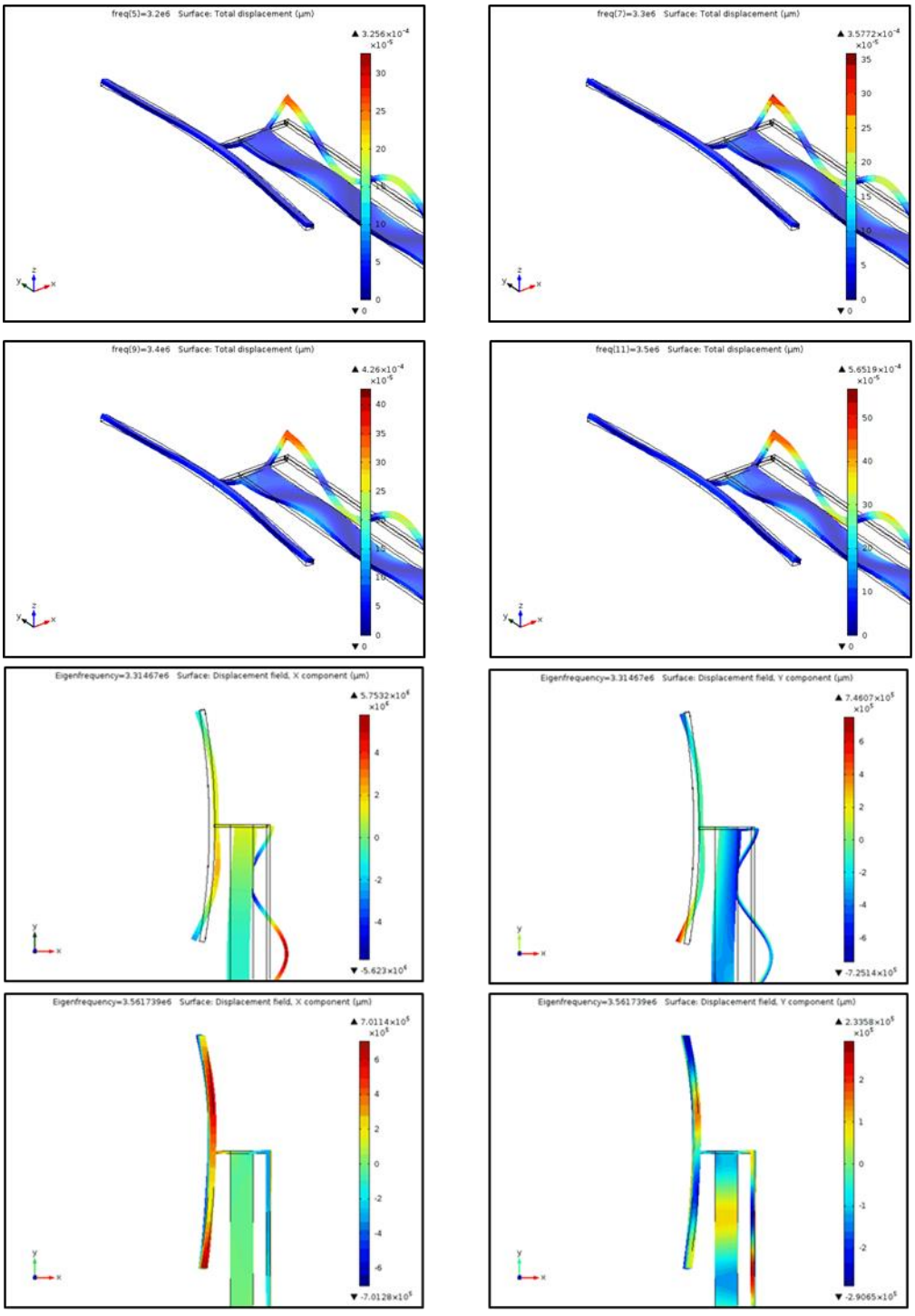

Figure C. 1 COMSOL simulations of thermal actuator driven gripper showing various resonant modes.

D. Rotor control through Gripper – Mathematica derivation

- u= Exp[-y/d]*((Cos[y/d-w*t+n*x]-(Exp[-2*g/d])*(Cos[(y-2*g)/(d)-w*t+n*x])-(Exp[-2*(g-y)/d])*(Cos[(2*g-y)/(d)-w*t+n*x])+(Exp[-2*(2*g-y)/d])*(Cos[y/d+w*t-n*x]))/(1-2*(Exp[-2*g/d])*Cos[2*g/d]+Exp[-4*g/d]))
- dudx = D[u,x]
- v=Integrate[dudx,y]
- uu=u*u
- uv=v*u
- uubar=Integrate[uu/(2*3.14), {t, 0, 6.28}]
- uvbar=Integrate[uv/(2*3.14), {t, 0, 6.28}]
- duubardx=D[uubar, x]
- duvbardy=D[uvbar, y]
- Facousticbyrho=duubardx-duvbardy
- Facousticbyrhozeg=Facousticbyrho/.y->g
- Facstreamrotorg=Facousticbyrhozeg/.{d ->1.24*10^(-6), w ->20.41*10^6, n ->1}
- m =1.205 * 10^(-9)
- Facstrmrotorgint=Integrate[Facstreamrotorg,x]
- Facstrmrotorgintxsubs=Facstrmrotorgint/.{x->170*10^(-6)}
- Facstrmrotorgintxsubsact=Facstrmrotorgintxsubs*m
- Facstrmrotorgintxsubsactreal=Re[Facstrmrotorgintxsubsact]

REFERENCES

[1] V. Kaajakari and A. Lal, "Thermo-Kinetic Actuation for Hinged Structure Batch Microassembly," in *The 15th IEEE International Conference on Micro Electro Mechanical Systems*, Las Vegas, Nevada, 2002.

[2] J. W. Judy, "Microelectromechanical systems (MEMS): fabrication, design and applications," *Smart materials and Structures,* vol. 10, no. 6, pp. 1115-1134, 2001.

[3] L.-S. Fan, Y.-C. Tai and R. S. Muller, "IC-processed electrostatic micromotors," *Sensors and actuators,* vol. 20, no. 1, pp. 41-47, 1989.

[4] K. R. Udayakumar, S. F. Bart, A. M. Flynn, J. Chen, L. S. Tavrow, L. E. Cross, R. A. Brooks and E. D. J., "Ferroelectric thin film ultrasonic micromotors," in *Micro Electro Mechanical Systems, 1991, MEMS '91, Proceedings. An Investigation of Micro Structures, Sensors, Actuators, Machines and Robots. IEEE*, Nara, 1991.

[5] V. Kaajakari, S. Rodgers and A. Lal, "Ultrasonically driven surface micromachined motor," in *Micro Electro Mechanical Systems, 2000. MEMS 2000. The Thirteenth Annual International Conference on*, Miyazaki, 2000.

[6] J. Sniegowski and E. Garcia, "Surface-micromachined gear trains driven by an on-chip electrostatic microengine," *Electron Device Letters, IEEE,* vol. 17, no. 7, pp. 366-368, 1996.

[7] B. Watson, J. Friend, and L. Yeo, “Piezoelectric ultrasonic micro/milli-scale actuators,” Sensors and Actuators A: Physical vol.152, no.2, pp. 219-233, 2009.

[8] A. M. Flynn, Piezoelectric ultrasonic micromotors, 1995.

[9] http://en.wikipedia.org/wiki/Electric_motor

[10] R. Muller and K. Y. Lau, "Surface-micromachined microoptical elements and systems,," *Proceedings of the IEEE,* vol. 86, no. 8, pp. 1705-1720, 1998.

[11] L. Lin, S. Lee, K. Pister and M. Wu, "Micro-machined three-dimensional micro-optics for integrated free-space optical system," *Photonics Technology Letters, IEEE,* vol. 6, no. 12, pp. 1445-1447, 1994.

[12] I. Okumura, "A designing method of a bar-type ultrasonic motor for autofocus lenses," *In Proc. IFToMM-jc Intl., Symp. on Theory of Machines and Mechanisms,* vol. 836, 1992.

[13] T. S. Glenn and N. W. Hagood, "Development of a two-sided piezoelectric rotary ultrasonic motor for high torque," *SPIE,* vol. 3041, pp. 326-338, 1997.

[14] K. Uchino, "Piezoelectric actuators 2006," *Journal of Electroceramics,* vol. 20, no. 3-4, pp. 301-311, 2008.

[15] C. Zhao, Ultrasonic Motors: Technologies and Applications, New York: Springer, 2011.

[16] NHK TV morning news, July 21st, 2004.

[17] X. Changliang and W. Mengli, "Stability analysis of the rotor of ultrasonic motor driving fluid directly," *Ultrasonics,* vol. 43, no. 7, pp. 596-601, 2003.

[18] Y. Yamayoshi, S. Hirose, S. Sone and H. Nakamura, "An Analysis on the Driving Force and Optimum Frequency of a Non-contact-Type Ultrasonic Motor," *Japanese journal of applied physics,* vol. 33, no. 1, pp. 3081-3084, 1994.

[19] J. Hu, K. Nakamura and S. Ueha, "Characteristics of a noncontact ultrasonic motor using acoustic levitation," in *Ultrasonics Symposium, 1996. Proceedings., 1996 IEEE,* San Antonio, TX, 373-376.

[20] T. Yamazaki, J. Hu, K. Nakamura and S. Ueha, "Trial construction of a noncontact ultrasonic motor with an ultrasonically levitated rotor," *Japanese Journal of Applied Physics,* vol. 35, pp. 3286-3288, 1996.

[21] J. Hu, K. Nakamura and S. Ueha, "An analysis of a noncontact ultrasonic motor with an ultrasonically levitated rotor," *Ultrasonics,* vol. 35, pp. 459-467, 1997.

[22] J. Hu, K. Nakamura and S. Ueha, "A noncontact ultrasonic motor with the rotor levitated by axial acoustic viscous force," *Electronics and Communications in Japan (Part III: Fundamental Electronic Science)*, vol. 82, pp. 56-63, 1999.

[23] J. Saito, J. Friend, K. Nakamura and S. Ueha, "Resonant mode design for noncontact ultrasonic motor with levitated rotor," *Japanese journal of applied physics*, vol. 44, p. 4666, 2005.

[24] J. Liu, B. Wu, Z. Yang, G. Cheng and Y. Lu, "A new type of circular cylindrical non-contact ultrasonic motor," *ACTA ACUSTICA-PEKING*, vol. 26, pp. 113-116, 2001.

[25] H. &. K. A. Isobe, "Frequency characteristics of non-contact ultrasonic motor with motion error correction," *Precision engineering*, vol. 31, no. 4, pp. 351-357, 2007.

[26] B. Yang, J. Liu, D. Chen and B. Cai, "Theretical and experimental research on a disk-type non-contact ultrasonic motor.," *Ultrasonics*, vol. 44, no. 3, pp. 238-243, 2006.

[27] J. L. G. C. H. L. W. &. C. C. L. Hu, "A standing wave-type noncontact linear ultrasonic motor.," *Ultrasonics, Ferroelectrics and Frequency Control, IEEE Transactions on*, vol. 48, no. 3, pp. 699-708, 2001.

[28] D. Koyama, H. Takei, K. Nakamura and S. Ueha, "A self-running standing wave-type bidirectional slider for the ultrasonically levitated thin linear stage," *Ultrasonics, Ferroelectrics and Frequency Control, IEEE Transactions on*, vol. 55, no. 8, pp. 1823-1838, 2008.

[29] K. Uchino, Piezoelectric actuators and ultrasonic motors, vol. 1. Springer, 1997.

[30] A. Kumada, "Ultrasonic motor using bending, longitudinal and torsional vibrations," U.S Patent No. 4,642,509, February 10,1987.

[31] N. Tsukada, "Ultrasonic motor", U.S. Patent No. 5,025,186, June 18, 1991.

[32] K. Uchino, S. Cagatay, B. Koc, S. Dong, P. Bouchilloux and M. Strauss, "Micro piezoelectric ultrasonic motors," *Journal of electroceramics,* vol. 13, no. 1-3, pp. 393-401, 2004.

[33] V.Kaajakari, "Ultrasonic surface micromachine actuation, Applications to release, microstructure assembly, and micromotors", 2002.

[34] S. Tin, Radio frequency pulsed signal transmitter utilizing radioisotope-powered self-triggered electrostatic discharge system, 2011.

[35] S. M. Ardanuç and A. Lal, "Ultrasound Enhanced Electrostatic Batch Assembly for MEMS," Sensors and Actuators A: Physical., 2013.

[36] S. Tin, M. Pandey and A. Lal, "Experimental verification and characterization of sub-harmonic traveling wave on an ultrasonic micromotor," in Ultrasonics Symposium (IUS), 2010 IEEE, San Diego, USA, 2010.

[37] V. Kaajakari and A. Lal, "Parametric excitation of circular micromachined polycrystalline silicon disks," *Applied Physics Letters,* vol. 85, no. 17, pp. 3923-3925, 2004.

[38] V. Kaajakari and A. Lal, "Micromachined ultrasonic motor based on parametric polycrystalline silicon plate excitation," *Sensors and Actuators A: Physical,* vol. 137, no. 1, pp. 120-128, 2007.

[39] S. Tin, S. Ardanuc and A. Lal, "Design optimization of polysilicon ultrasonic micromotor," in *Ultrasonics Symposium (IUS), 2009 IEEE International*, Rome, 2009.

[40] A. Cowen, B. Hardy, R. Mahadevan and S. Wilcenski, "PolyMUMPS design handbook," [Online]. Available: http://www.memscap.com/__data/assets/pdf_file/0019/1729/PolyMUMPs-DR-13-0.pdf.

[41] K. Pister, "Hinged polysilicon structures with integrated CMOS TFTs," in Solid-State Sensor and Actuator Workshop, 1992. 5th Technical Digest., IEEE,, Hilton Head, SC, USA, 1992.

[42] A. Lal and R. M. White, “Silicon microfabricated horns for power ultrasonics”, Sensors and Actuators A: Physical, vol. 54, no. 1, pp.542-546, 1996.

[43] M. Koch, A.G.R. Evans and A. Brunnschweiler, “The dynamic micropump driven with a screen printed PZT actuator”, Journal of Micromechanics and Microengineering, vol. 8, no.2, pp.119, 1998.

[44] A. W. Leissa, Vibration of plates, Acoustical society of America, 1993.

[45] C. Touzé, O. Thomas and M. Amabili, “Transition to chaotic vibrations for harmonically forced perfect and imperfect circular plates.” *International Journal of non-linear Mechanics*, vol. 46, no.1, pp. 234 – 246, 2011.

[46] S. Sridhar, D.T. Mook and A.H. Nayfeh, “Non-linear resonances in the forced responses of plates, Part II: Asymmetric responses of circular plates.” Journal of Sound and Vibration, vol. 59, no. 2, pp. 159 – 170, 1978.

[47] C. Williams and S. Tobias, "Forced undamped non-linear vibrations of imperfect circular discs," *Journal of Mechanical Engineering Science*, vol. 5, no. 4, pp. 325-335, 1963.

[48] T. A. Nayfeh and A. F. & Vakakis, "Subharmonic travelling waves in a geometrically non-linear circular plate," International journal of non-linear mechanics, vol. 29, no. 2, pp. 233-245, 1994.

[49] L. Debnath, *Sir James Lighthill and modern fluid mechanics*, Imperial College Press, 2008.

[50] C. Lee and T. Wang, "Near-boundary streaming around a small sphere due to two orthogonal standing waves," *The Journal of the Acoustical Society of America*, vol. 85, p. 1081, 1989.

[51] M. T. K. L. K. M. Hou, H. Z. Yeh, B. W. Cheng, P. Y. Hong and R. Chen, "Fabrication of micromachined focusing mirrors with seamless reflective surface," *Micromachining and Microfabrication, International Society for Optics and Photonics 2003*, pp. 359-366, 2003.

[52] M. L. Dunn, Y. Zhang and V. Bright, "Deformation and structural stability of layered plate microstructures subjected to thermal loading," *Microelectromechanical Systems, Journal of,* vol. 11, no. 4, pp. 372-384, 2002.

[53] M. T.-K. Hou, K.-M. Liao, H.-Z. Yeh, P.-Y. Hong and R. Chen, "Design and fabrication of surface-micromachined spherical mirrors," in *Optical MEMs, 2002. Conference Digest. 2002 IEEE/LEOS International Conference on*, Lugano, Switzerland, 2002.

[54] E. Jomehzadeh, A. R. Saidi and S. R. & Atashipour, "An analytical approach on the buckling analysis of circular, solid and annular functionally graded thin plates," *Journal of Mechanical Engineering,* vol. ME.41, no. 1, 2010.

[55] W.F. Faris, "Nonlinear dynamics of annular and circular plates under thermal and electrical loadings", 2003.

[56] D.O. Brush and B.O. Almroth, *Buckling of bars, plates and shells*, vol. 6, no.6, New York: McGraw-Hill, 1975

[57] W. Cowan, V. Bright, A. Elvin and D. Koester, "Modeling of stress-induced curvature in surface-micromachined devices", International Society for Optics and Photonics, pp.56-67, Septermber 1997.

[58] D. Holmes, M. Ursiny and A. Crosby, "Crumpled surface structures," *Soft Matter,* vol. 4, no. 1, pp. 82-85, 2007.

[59] D. Shilkrut and E. Riks, Stability of nonlinear shells: on the example of spherical shells, Kidlington, Oxford, UK: Elsevier Science, 2002.

[60] M. Kraft, M. Farooqui and A. Evans, "Modeling and design of an electrostatically levitated disk for inertial sensing applications," *Journal of Micromechanics and Microengineering,* vol. 11, no. 4, pp. 423-427, 2001.

[61] C. Shearwood, K. Y. Ho, C. B. Williams and H. Gong, "Development of a levitated micromotor for application as a gyroscope," *sensors and actuators A: physical,* vol. 83, no. 1, pp. 85-92, 2000.

[62] B. Dillard, V. Trent, M. Greene and E. W. Taylor, "Radiation effects on multiple DOF MEMS inertial sensors," in *Proc. SPIE 8164, Nanophotonics and Macrophotonics for Space Environments V*, San Diego, CA, 2011.

[63] T. Murakoshi, Y. Endo, K. Fukatsu, S. Nakamura and M. Esashi, "Electrostatically levitated ring-shaped rotational-gyro/accelerometer," *Japanese Journal of Applied Physics*, vol. 42, no. n4B, pp. 2468-2472, 2003.

[64] Q. A. Huang and N. K. S. Lee, "Analysis and design of polysilicon thermal flexure actuator," *Journal of Micromechanics and Microengineering*, vol. 9, no. 1, pp. 64-72, 1999.

[65] R. Hickey, D. Sameoto, T. Hubbard and M. Kujath, "Time and frequency response of two-arm micromachined thermal actuators," *Journal of Micromechanics and Microengineering*, vol. 13, no. 1, pp. 40-46, 2003.

[66] M. Mayyas, P. S. Shiakolas, W. H. Lee and H. Stephanou, "Thermal cycle modeling of electrothermal microactuators," *Sensors and Actuators A: Physical*, vol. 152, no. 2, pp. 192-202, 2009.

[67] M. J. Crocker, ed. Handbook of acoustics. Wiley.com, 1998.

[68] P. Aggarwal, Z. Syed, X. Niu and N. El-Sheimy, "A standard testing and calibration procedure for low cost MEMS inertial sensors and units," *Journal of Navigation*, vol. 61, no. 2, pp. 323-336, 2008.

[69] I.P. Prikhodko, S. A. Zotov, A. A. Trusov, A. M. Shkel, “What is MEMS Gyrocompassing? Comparative Analysis of Maytagging and Carouseling”, 1-1, 2013

[70] S.M. Kohler, *MEMS Inertial Sensors with Integral Rotation Means*, United States, Department of Energy, 2003.

[71] G.Zhou, K.K. Cheo, Y. Du and F.S. Chau, “An optically interrogated microgyroscope using an out-of-plane lamellar grating”, Sensors and Actuators A: Physical, vol. 154, no. 2, pp. 269-274, 2009.

[72] Vishnevsky, V. V. Lavrinenko, M. M. Nekrasov and A. A. Prez, "Piezoelectric motor structures". USA Patent 4,019,073, 19 April 1977.

[73] K. Ragulskis, R. Bansevicius, R. Barauskas and G. Kulvietis, Vibromotors for precision microrobots, New York: Hemisphere Publishing Corporation, 1988.

[74] R. Inaba, A. Tokushima, O. Kawasaki, Y. Ise and H. Yoneno, "Piezoelectric Ultrasonic Motor," in *IEEE 1987 Ultrasonics Symposium* , Denver, 1987.

[75] T. Sashida, "Trial Construction and Operation of an Ultrasonic Vibration Drive Motor:Theoretical and Experimental Investigation of its Performances," *Oyo Butsuri,* vol. 51, no. 6, pp. 713-720, 1982.

[76] T. Sashida, "Ultrasonic Motors," *Japanese Journal of Applied Physics,* vol. 54, no. 6, pp. 589(65) - 590(66), 1985.

[77] Shinsei Corporation, *Operation Manual for the Ultrasonic Motor,* Japan: Shinsei Corporation, 1-8, Kasuya 2-chome, Setagaya-ku, Tokyo, 157 Japan, 1989.

[78] I. Okumura and H. Mukohjima, "A Structure of Ultrasonic Motor for Auto Focus Lenses," in *Proceedings of Motor Control*, 1987.

[79] K. Hosoe, "An Ultrasonic Motor for Use in Autofocus Lens Assemblies," *Techno,* pp. 36-41, 1989.

[80] M. Kasuga, T. Satoh, J. Hirotomi and M. Kawata, "Development of Ultrasonic Motor and Application to Silent Alarm Analog Quartz Watch," in *4th Congres Europeen de Chronometrie*, Lausanne, Switzerland, 1992.

[81] T. Sashida and T. Kenjo, Introduction to Ultrasonic Motors, Oxford, UK: Oxford University Press, 1993.

[82] S. Ueha and Y. Tomikawa, Ultrasonic Motors: Theory and Applications, Oxford, UK: Oxford University Press, 1993.

[83] R. Moroney, R. White and R. Howe, "Ultrasonic Micromotors," in *Ultrasonics Symposium, 1989. Proceedings.*, Montreal, Quebec, 1989.

[84] A. M. Flynn, L. S. Tavrow, S. F. Bart, R. A. Brooks, D. J. Ehrlich, K. R. Udayakumar and L. Eric Cross, "Piezoelectric micromotors for microrobots,"

IEEE Journal of Microelectromechanical Systems, vol. 1, no. 1, pp. 44-51, 1992.

[85] W. Nyborg, "Acoustic Streaming near a Boundary," *The Journal of the Acoustical Society of America*, vol. 30, no. 4, pp. 329-339, 1958.

[86] S. Piratla and A. Lal, "Resonant stator gear coupled ultrasonic motors," in *Transducers*, Beijing, China, 2010.

[87] [Online]. Available: http://www.gcdataconcepts.com/calibration.html.

[88] S. Hirose, Y. Yamayoshi and H. Ono, "A small noncontact ultrasonic motor," in *Ultrasonics Symposium, 1993. Proceedings., IEEE 1993*, Baltimore, MD, 1993.

[89] J. Hu, G. Li, H. L. W. Chan and C. L. Choy, "A standing wave-type noncontact linear ultrasonic motor," *Ultrasonics, Ferroelectrics and Frequency Control, IEEE Transactions on*, vol. 48, no. 3, pp. 699-708, 2001.